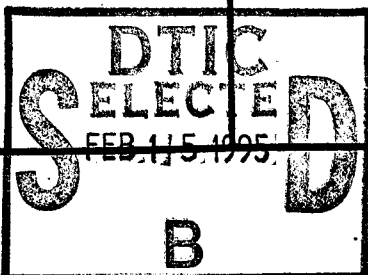


# REPORT DOCUMENTATION PAGE

Form Approved  
OMB No. 0704-0188

Public reporting burden for this collection of information is estimated to average 1 hour per response, including the time for reviewing instructions, searching existing data sources, gathering and maintaining the data needed, and completing and reviewing the collection of information. Send comments regarding this burden estimate or any other aspect of this collection of information, including suggestions for reducing this burden, to Washington Headquarters Services, Directorate for Information Operations and Reports, 1215 Jefferson Davis Highway, Suite 1204, Arlington, VA 22202-4302, and to the Office of Management and Budget, Paperwork Reduction Project (0704-0188), Washington, DC 20503.

1. AGENCY USE ONLY (Leave blank)		2. REPORT DATE June 6, 1994	3. REPORT TYPE AND DATES COVERED Final (5/1/91 thru 7/31/94)	
4. TITLE AND SUBTITLE Ceramics Derived From Metal-Organic Precursors			5. FUNDING NUMBERS F49620-91-C-0033 6110 AF 2303-BS	
6. AUTHOR(S) Professor Donald R. Uhlmann				
7. PERFORMING ORGANIZATION NAME(S) AND ADDRESS(ES) Material Sciences and Engineering College of Engineering and Mines The University of Arizona Tucson, Arizona 85721			8. PERFORMING ORGANIZATION REPORT NUMBER AFOSR-TR- 95 0070	
9. SPONSORING/MONITORING AGENCY NAME(S) AND ADDRESS(ES) Air Force Office of Scientific Research/NL 110 Duncan Avenue Suite B115 Bolling AFB, DC 20332-0001 MAJ. Erstfeld.			10. SPONSORING/MONITORING AGENCY REPORT NUMBER	
11. SUPPLEMENTARY NOTES				
12a. DISTRIBUTION/AVAILABILITY STATEMENT Approved for public release; distribution is unlimited			12b. DISTRIBUTION CODE	
13. ABSTRACT (Maximum 200 words)  Research carried out under the present grant has during the past year been directed to four principal areas: (A) Ferroelectric Films; (B) Organic-Inorganic Hybrid Materials (POLYCERAMS); (C) Nonlinear Optic Dyes in POLYCERAM Hosts; and (D) Gradient Refractive Index Lenses. In all cases, the research was based upon developing novel combinations of chemistry and processing to produce novel materials and structures with exceptional properties and characteristics. Also carried out have been systematic investigations of important phenomena and modeling of observed behavior.				
14. SUBJECT TERMS			15. NUMBER OF PAGES 167	
			16. PRICE CODE	
17. SECURITY CLASSIFICATION OF REPORT Unclassified	18. SECURITY CLASSIFICATION OF THIS PAGE Unclassified	19. SECURITY CLASSIFICATION OF ABSTRACT Unclassified	20. LIMITATION OF ABSTRACT UL	

19950207 060

187 JUN 1995

AIR FORCE  
OFFICE OF SCIENTIFIC RESEARCH

**FINAL REPORT**

**AFOSR-TR- 95 0070**

**on**

**CERAMICS DERIVED FROM ORGANO-METALLIC PRECURSORS**

**(GRANT NO. F49620-91-C-0033)**

**Approved for public release;  
distribution unlimited.**

**submitted to**

**AIR FORCE OFFICE OF SCIENTIFIC RESEARCH**

**by**

**UNIVERSITY OF ARIZONA**

**Professor D.R. Uhlmann  
Principal Investigator**

**DTIC QUALITY INSPECTED 4**

## I. INTRODUCTION

Research carried out under the present grant has during the past year been directed to four principal areas: (A) Ferroelectric Films; (B) Organic-Inorganic Hybrid Materials (POLYCERAMS); (C) Nonlinear Optic Dyes in POLYCERAM Hosts; and (D) Gradient Refractive Index Lenses. In all cases, the research was based upon developing novel combinations of chemistry and processing to produce novel materials and structures with exceptional properties and characteristics. Also carried out have been systematic investigations of important phenomena and modelling of observed behavior.

In each area, important results have been obtained during the past year. These include fabrication of the first POLYCERAM r-GRIN lenses; demonstration that POLYCERAM films can be patterned with, e.g., grating structures; synthesis and fabrication of POLYCERAM planar waveguides with exceptionally low attenuations (in one system, less than 0.15 dB/cm); synthesis, using functionalized dyes, of dye-containing POLYCERAMS with remarkable thermal stability; synthesis and fabrication of lead titanate-based films with greatly improved resistance to fatigue and aging; synthesis and fabrication of amorphous films with exceptionally high refractive index ( $n > 2$ ) and low attenuation (1 dB/cm), and of polycrystalline ferroelectric films with lower

<input checked="" type="checkbox"/>	
<input type="checkbox"/>	
<input type="checkbox"/>	
By _____	
Distribution/ _____	
Availability Codes	
Dist	Avail and/or Special
A-1	

attenuations than previous single crystal or epitaxial films; and development of a new model of ferroelectric films whose predictions are in remarkable accord with experimental data, and which can serve as a highly effective guide for future investigations.

The results of these investigations have demonstrated that by appropriate control of synthesis, using selected precursors and chelating agents, combined with innovations in processing, it is possible to produce ceramic films and POLYCERAMS with exceptional chemical homogeneity, microstructures and combinations of properties. In several cases - e.g., gradient index POLYCERAM lenses, fatigue resistant ferroelectric films, POLYCERAM and high index ceramic waveguides and patternable POLYCERAM films - the results have considerable technological as well as scientific interest; and contacts have been established with Hughes, Donnelly, Corning and YTC America to pursue potential commercialization of the technology.

In addition, the results obtained during the past two years have pointed the way to exciting extensions into new areas, including POLYCERAM lasers based on inorganic lasing ions; spontaneous emission lasers based on combining grating structures with Er POLYCERAM lasers; dye lasers based on functionalized energy-transfer dye pairs; NANOFERRODEVICES based

on utilizing the ferroelectric response in films parallel to the film surface; and novel ferroelectric films and electrodes. The proposed work in these areas is outlined in the appended Progress Report.

**(A) Published Papers Supported by Grant.**  
**September, 1992 - August, 1993**

1. G. Teowee, J.M. Boulton, S. Motakef, B.J.J. Zelinski, D.R. Uhlmann and R. Zaroni, "Optical Properties of Sol-Gel Derived Lead Titanate-Based Films," Sol-Gel Optics II, SPIE 1758, 236-248 (1992).
2. J.M. Boulton, G. Teowee, W.M. Bommersbach and D.R. Uhlmann, "Second Harmonic Generation from Sol-Gel Derived Ferroelectric Thin Films," Sol-Gel Optics II, SPIE 1758, 292-303 (1992).
3. S. Motakef, J.M. Boulton, G. Teowee, B.J.J. Zelinski, D.R. Uhlmann and R. Zaroni, "Optical Properties of POLYCERAM Films," Sol-Gel Optics II, SPIE 1758, 432-445 (1992).
4. J.M. Boulton, G. Teowee, W.M. Bommersbach and D.R. Uhlmann, "Sol-Gel Derived Barium Sodium Niobate and Bismuth Titanate Films," Ferroelectric Thin Films II, MRS Symp. Proc. 243, 303-308 (1992).
5. G. Teowee, J.M. Boulton and D.R. Uhlmann, "Electrical Characterization of Sol-Gel Derived PZT Films," Ferroelectric Thin Films II, MRS Symp. Proc., 243, 255-261 (1992).
6. D.R. Uhlmann and E.V. Uhlmann, "Crystal Growth and Melting in Glass-Forming Systems, A View From 1992," Ceramic Transactions, 30, 109-140 (1993).
7. M. Denesuk, G.L. Smith, B.J.J. Zelinski, N.J. Kreidl and D.R. Uhlmann, "Capillary Penetration of Liquid Droplets into Porous Materials," Journal of Colloid and Interface Science 158 (1993) 114-120.

8. M. Denesuk, B.J.J. Zelinski and D.R. Uhlmann, "Dispersion Energy of a Spherical Cap on a Semi-Infinite Solid", *Journal of Colloid and Interface Science* **155** (1993) 520-521.
9. B.J.J. Zelinski, J.P. Cronin, M. Denesuk and D.R. Uhlmann, "High-Temperature Wetting Behavior of Inorganic Liquids," pp. 465-524 in J.C. Berg, ed., *WETTABILITY* (Dekker, New York, 1993).
10. D.R. Uhlmann, J.M. Boulton and G. Teowee, "Ceramic Films for Optical Applications," pp. 113-126 in *PROCEEDINGS OF THE EUROPEAN SOL-GEL SUMMER SCHOOL* (CNRS, Paris, 1993).

**(B) Papers In Press Supported by Grant**

1. D.R. Uhlmann, S. Motakef, T. Suratwala, R. Wade, G. Teowee and J.M. Boulton, "Ceramic Films for Optical Applications," to appear in *Journal of Sol-Gel Science and Technology*.
2. G. Teowee, J.M. Boulton, C.D. Baertlein, R.K. Wade and D.R. Uhlmann, "Effect of Post-Metallization Annealing on the Ferroelectric Properties of Sol-Gel Derived PZT Thin Films," to appear in *Journal of Sol-Gel Science and Technology*.
3. A. Aruchamy, D. Fry, J.M. Boulton, B.J.J. Zelinski, D.R. Uhlmann and E.A. Tomic, "Effect of Synthesis Route on Properties of Cordierite Based Glasses-Melt and Wet-Chemical Derived Glass Powders," to appear in *Journal of the American Ceramic Society*.
4. S.C. Lee, G. Teowee, R.D. Schrimpf, D.P. Birnie, D.R. Uhlmann and K.F. Galloway, "Low Total-Dose Radiation Effects on Sol-Gel Derived PZT Thin Films," to appear in *Proceedings of the IEEE Nuclear and Space Radiation Effects Conference*, New Orleans, July 1992.

5. G. Teowee, J.M. Boulton and D.R. Uhlmann, "Retention in Sol-Gel Derived PZT Thin Films," to appear in Proceedings of 1992 IEEE International Symposium on the Applications of Ferroelectrics.
6. G. Teowee, R.K. Wade, J.M. Boulton, D.P. Birnie, E.A. Kneer, M.N. Orr and D.R. Uhlmann, "Effect of Zr/Ti Ratio on the Fatigue and Retention Behaviors of Sol-Gel Derived PZT Thin Films," to appear in Ferroelectric Films III, MRS Symp. Proc.
7. S. Seraphin, D. Zhou, G. Teowee, J.M. Boulton and D.R. Uhlmann, "Transmission Electron Microscopy of PZT Thin Films Prepared by a Sol-Gel Technique," to appear in Ferroelectric Films III, MRS Symp. Proc.
8. G. Teowee and D.R. Uhlmann, "A Model of the Metal-Ferroelectric-Metal Capacitor," to appear in Ferroelectric Films III, MRS Symp. Proc.
9. G. Teowee, J.M. Boulton, R.K. Wade, T. Suratwala and D.R. Uhlmann, "Electrical Properties of Sol-Gel Derived La-Doped PbTiO<sub>3</sub>-Containing Films," to appear in Proceedings of the 5th International Symposium on Integrated Ferroelectrics, April, 1992.
10. S.C. Lee, G. Teowee, R.D. Schrimpf, D.P. Birnie, D.R. Uhlmann and K.F. Galloway, "Effect of Fatigue on the I-V Characteristics of Sol-Gel Derived PZT Thin Films," to appear in Integrated Ferroelectrics.
11. S.C. Lee, G. Teowee, R.D. Schrimpf, D.P. Birnie, D.R. Uhlmann and K.F. Galloway, "Fatigue Effect on the I-V Characteristics of Sol-Gel Derived PZT Thin Films," to appear in Proceedings of the 1992 IEEE International Symposium on the Application of Ferroelectrics.
12. S.C. Lee, G. Teowee, R.D. Schrimpf, D.P. Birnie, D.R. Uhlmann and K.F. Galloway, "Fatigue Effect on the I-V Characteristics of Sol-Gel Derived PZT Thin Films," to appear in Proceedings of the 1992 IEEE Transducers, Ultrasonics, Ferroelectrics and Frequency Control.
13. D.R. Uhlmann, J.M. Boulton and G. Teowee, "Sol-Gel Synthesis of

Materials for Optical Applications," to appear in Proceedings of the Izumi Forum, Osaka, Japan, November, 1992.

14. S. Motakef, J.M. Boulton, R.L. Roncone, G. Neilson, G. Teowee and D.R. Uhlmann, "An Optical Loss Study of MPEOU-Based POLYCERAM Planar Waveguides," to appear in Journal of Applied Physics.
15. S. Motakef, T. Suratwala, R. Roncone, J.M. Boulton, G. Teowee and D.R. Uhlmann, "Processing and Optical Properties of Inorganic-Organic Hybrids (POLYCERAMS); Part 1: MPEOU-Based Waveguides," to appear in Journal of Non-Crystalline Solids.
16. S. Motakef, T. Suratwala, R.L. Roncone, J.M. Boulton, D.R. Uhlmann, "Processing and Optical Properties of Inorganic-Organic Hybrids (POLYCERAMS); Part 2: PDMS-Based Waveguides," to appear in Journal of Non-Crystalline Solids.
17. M. Denesuk, J.P. Cronin, B.J.J. Zelinski, N.J. Kreidl and D.R. Uhlmann, "Predictive Modelling of Liquids Spreading on Solid Surfaces," to appear in Physics and Chemistry of Glasses.

**(C) Graduate Students Supported by Grant**

1. Mr. Matthew Denesuk: B.S., MIT, Ph.D. candidate. Supported half-time academic year and full-time summer by the grant.
2. Ms. S. Motakef: B.S., MIT, Ph.D. candidate. Supported half-time academic year and full-time summer by the grant.
3. Mr. T. Suratwala: B.S., University of Illinois, Ph.D. candidate. Supported half-time academic year and full-time summer by the grant. Beginning 8/93 will be supported by Fellowship provided by Corning Inc.
4. Mr. G. Teowec: B.S., University of Rochester. Received Ph.D. in



December, 1992. Was supported half-time academic year and full-time summer by the grant. Presently employed by Donnelly Corp. in Tucson.

5. Mr. Robert Wade: B.S., University of Missouri at Rolla, Ph.D. candidate. Supported half-time academic year and full-time summer by AASERT extension of the grant.

(D) Postdoctoral Researchers Supported by Grant

1. Dr. J. Boulton: Supported full-time by the grant.

## **II. PROGRESS IN SPECIFIC AREAS**

### **A. Ferroelectric Films**

#### **1. Accomplishments of the Previous Year (1991-1992)**

During the previous year of the current investigation, notable progress was achieved in obtaining PZT 53/47 films with exceptional ferroelectric (FE) and dielectric properties, notably a dielectric constant,  $\epsilon_r$ , as large as 3000, exceptionally low leakage currents ( $3 \times 10^{-8}$  A/cm<sup>2</sup> at 100 kV/cm applied field), high fatigue resistance (up to  $10^8$  cycles) and very low aging rates (<0.5%/decade time). These properties, shown in Table 1 on the following page, are notably superior to those of any other PZT films reported in the literature, whether prepared wet chemically or by physical vapor deposition methods, making them particularly attractive for applications in FE memory and high-density DRAM's. These high quality PZT films were obtained via detailed and precise control of not only the synthetic chemistry, including the complexation of the acetate and alkoxide precursors with diethanolamine, but also the subsequent post-deposition processing.

**Table 1: Electrical and Optical Properties of AML Films and other PZT Films (1991-1992)**

	Dielectric Constant	Leakage Current A/cm <sup>2</sup> @ 100 kV/cm	Absorption Edge (Å)	Attenuation Loss (dB/cm)	Aging Rate (%/decade)	Fatigue Resistance (cycles)
AML films	3000	$3 \times 10^{-8}$	2900	1.1-1.4	0.3	$10^6$
Typical sol-gel films	1200	$4 \times 10^{-5}$	3400	5-20		$10^8$ - $10^{10}$
Sputtered films	800	$1 \times 10^{-7}$	3500	5-15		$10^8$ - $10^{10}$
Bulk ceramics	1200	---	3400	---	1.0-5.0	---

With respect to chemistry, the incorporation of excess PbO in the precursor solution affects both the microstructure and phase assembly and results in a 50% increase of  $\epsilon_r$  compared to stoichiometric PZT 53/47 films. In the latter films, firing temperatures of about 750C are required to prepare pyrochlore-free films, while the incorporation of excess PbO allows the achievement of single-phase perovskite films at temperatures as low as 550C, even without the addition of nucleating agents. PbO loss in PZT films occurs from both reaction with the substrates and volatilization loss, and increases with increasing processing temperatures. Such PbO loss needs to be compensated by adding excess PbO in the precursor solutions. Additionally,

superior dielectric and FE properties due to the large grain sizes and hence enhanced domain wall mobility.

Process optimization led to the formation of (100) oriented PZT 53/47 films on (200) oriented Pt substrates. This promoted high values of  $\epsilon_r$  since the direction of spontaneous polarization lies along the substrate plane and the  $\epsilon_r$  is maximal perpendicular to this polarization direction. The finding here provided the basis for a patent disclosure which has been prepared.

Further optimization and tailoring of the chemistry involved in obtaining PZT thin films also enabled the preparation of PZT fibers, which are rarely reported in the literature. It was determined that these fibers can also be densified to a high degree and exhibit potential for composite applications. Additions of  $H_2O$  and polyvinylpyrrolidone facilitate fiber formation. Similar to the case for thin films, the incorporation of excess PbO resulted in fibers exhibiting denser microstructures. Seeding the precursor sol with dispersed PZT powders gave rise to thicker fibers and enhanced their crystallization to the perovskite phase.

Attention was also directed to the wet chemical synthesis of a wide variety of other FE films (beyond the PZT system) which include the perovskite FE's (e.g.,  $BaTiO_3$ ,  $(Ba,Pb)TiO_3$ ,  $(Ba,Sr)TiO_3$  and  $KNbO_3$ ), relaxor

FE's (e.g., PMN), tungsten bronze FE's ((Ba,Sr)Niobate,  $\text{Pb}_2\text{Ta}_2\text{O}_7$ ), layered FE's (e.g.,  $\text{Bi}_4\text{Ti}_3\text{O}_{11}$ ), ilmenite FE's (e.g.,  $\text{LiNbO}_3$  and  $\text{LiTaO}_3$ ) and uniaxial FE's (e.g.,  $\text{Pb}_5\text{Ge}_3\text{O}_{11}$ ). All these FE films were explored for their second harmonic generation (SHG) activities. It was found that such films offer potential in integrated optics in spite of their polycrystalline nature which affects scattering.

## 2. Accomplishments of the Current Year

During the current year, attention has focussed on the further optimization of the electrical and optical properties of sol-gel derived PZT 53/47 films. Significant improvements were obtained in leakage current, aging rate and fatigue resistance. For example, further tailoring of chemistry and processing has enabled the preparation of PZT films with leakage currents at 100kV/cm applied field of  $1 \times 10^{-9}$  A/cm<sup>2</sup>, compared with values achieved last year of  $3 \times 10^{-8}$  A/cm<sup>2</sup>; and fatigue resistance has been extended from  $10^8$  cycles to  $10^{10}$  cycles.

In contrast to the focus of the previous year's effort on PZT 53/47, the attention this year has been broadened to exploring the dielectric, FE and optical properties of both PZT and PLZT (lead lanthanum zirconium titanate)

films as a function of the Zr/Ti ratio and the degree of La incorporation. The microstructures of PZT thin films were also investigated using transmission electron microscopy (TEM) and electron diffraction as a function of excess PbO content and Zr/Ti stoichiometry.

A highly successful model of Pt-PZT-Pt capacitors has also been developed. This model is based on the concept of totally depleted back-to-back Schottky barriers. Excellent agreement has been found between predictions of the model and actual device characteristics. This model has important implications for understanding both normal and relaxor ferroelectric films, and can aid significantly in designing the next generation of integrated FE devices.

### Microstructural Characterization

The phase assemblage (whether amorphous, pyrochlore or perovskite phases) determines to a large extent the film properties, especially the ferroelectric properties. Many of the FE properties improve with increasing concentration of the FE perovskite phase compared to the non-perovskite phases, notably pyrochlore. A larger concentration of perovskite results not only in enhanced values of dielectric constant, remanent polarization and

dielectric loss, but also in lower values of coercive field.

It has been found, however, that increased content of the perovskite phase does not lead to optimization of all desired FE properties. A striking example of this is provided by resistance to fatigue (change in dielectric properties on cycling the field), a property which is critical for FE memory applications. While the focus of other researchers has been directed to optimizing the fatigue resistance of single-phase perovskite PZT films, it was first discovered (surprisingly) in the previous year of the present program that the presence of a pyrochlore phase in conjunction with perovskite can substantially improve the fatigue and aging behaviors and also enhance the radiation hardness. During the present year, this discovery has been extended to optimize the phase assemblage and microstructure for resistance to fatigue and aging; and a patent disclosure has been prepared on the finding.

The firing temperature, soak time and heating rate have all been shown to affect the phase assemblage in PZT films. There exists a window of processing conditions in which single-phase perovskite PZT films are obtained. Higher firing temperature and longer soak times favor the formation of perovskite by allowing more complete amorphous-perovskite transformation to take place. Films fired at low temperatures tend to be amorphous when

deposited on glass substrates and contain pyrochlore when deposited on Pt. Very slow heating rates ( $\sim 1^\circ\text{C min}^{-1}$ ) or fast heating rates (e.g., rapid thermal annealing) result in films with high perovskite contents. In slowly-heated films, there is more time for conversion to perovskite; while in rapidly-heated films, the window in temperature for nucleation of pyrochlore can be bypassed.

In nominally stoichiometric PZT films (i.e., films containing no excess PbO), the microstructures typically consist of large perovskite rosettes ( $\mu\text{m}$ 's in size) and a fine intergrain phase ( $< 100\text{nm}$ ). The intergrain phase is relatively PbO-poor compared to the perovskite rosette grains. Such a biphasic microstructure may result from phase separation in the gel network upon firing into PbO-rich and PbO-poor microregions: TEM work during the present year has indicated a texture of the amorphous, stoichiometric PZT which may reflect such phase separation (see Fig. A-2 below), where the respective regions subsequently crystallize into perovskite and pyrochlore grains on heat treatment. PZT films containing such microstructures exhibit satisfactory (but not outstanding) FE properties - e.g., a film heated to  $750^\circ\text{C}$  exhibits a dielectric constant ( $\epsilon_r$ ) of 1200. It was expected ( and later verified) that a uniform microstructure containing only perovskite grains would provide superior FE properties.



The improvement in film microstructures and dielectric properties achieved during the present year was obtained principally through controlled incorporation of excess PbO. The incorporation of excess PbO eliminates the formation of such biphasic rosette-and-intergrain microstructures by reducing the tendency to form PbO-rich and PbO-poor microregions, and thus results in dense single-phase perovskite PZT films.

The excess PbO not only aids in obtaining PZT films with large grain sizes (which enhances the FE properties), but also promotes crystallization of the perovskite phase. The larger grains result in higher domain wall mobilities which increase  $\epsilon_r$ , remanent polarization ( $P_r$ ) and aging rate, but lower the coercive field ( $E_c$ ) and switching time.

In recent work, it has been found that when bulk gels are formulated with excess PbO, an extraneous PbO phase is formed upon firing; but no such PbO phase is found in thin films formulated with excess PbO. In the case of films, the excess PbO in the formulation does not produce superstoichiometric PZT structures (where the excess Pb atoms are incorporated directly in the perovskite lattices). Rather, the excess PbO is removed upon firing at high temperatures, both by volatilization (which is important due to the high surface area/bulk volume of the films) and diffusion into the underlying substrates.

ceramics as thin films.

The phase assemblages of PLT and PLZT films depend strongly on the specific composition and firing temperature chosen. The crystallization behaviors of PLT films deposited on Pt and Corning 7059 glass are quite similar. PT films on Pt did not convert into single-phase perovskite until fired at or above 600C. Incorporation of La significantly aided in obtaining perovskite. In PLT films with La contents of  $\geq 7$  mole %, single-phase perovskite films were obtained at temperature as low as 500C. In contrast, PT films fired to 500C still contained pyrochlore.

PT is highly anisotropic; and the addition of La into its crystal lattice tends to render the structure more cubic (less tetragonal). The perovskite nuclei are cubic, and the paraelectric pyrochlore phase (which usually forms

As an additional intriguing observation, the crystallization of PZT films on heating takes place at temperatures which are notably higher (typically by  $>200$ C) than those at which crystallization of bulk gels of the same composition is observed. Since the films are in contact with a potentially-nucleating substrate, and since the difference in crystallization temperature can by no means be explained by the difference in volume of the two forms, these

and PLZT (lead lanthanum zirconate titanate) - offers a corresponding wide range of properties, and also of applications. Research activity was therefore directed to exploring the applicability of compositions known from bulk PLZT

implication of these observations is the impact of dopant incorporation on phase formation: lower perovskite crystallization temperatures can be achieved as long as the dopants (not necessarily restricted to La) render the perovskite phase more cubic.

In PLZT films, the phase assemblages are dependent not only on the La content, but also on the Zr/Ti ratios. The presence of Zr was found to inhibit crystallization, particularly the formation of the perovskite phase, due to the diffusion of PbO into the substrate especially at high Zr content. In DTA studies of PZT and PLZT gels, the crystallization temperatures increased with increasing Zr/Ti content. In PLZT films with similar La content, single-phase perovskite was obtained at lower temperature for films with high Ti content (or low Zr/Ti ratio). For example, a PLZT 12/20/80 film was already single-phase perovskite when fired to 500C; while a PLZT 12/65/35 film still contained pyrochlore even when fired to 750C for 30 min. For PLZT films with fixed Zr/Ti ratio, the addition of La inhibited perovskite formation, in contrast with PLT films where La incorporation promoted the formation of perovskite. This is illustrated by observations on PLZT x/65/35 films where for La content (x) greater than 7 mole %, the films remained single-phase pyrochlore even when fired to 750C.

The microstructures of PZT films have during the present year been investigated using transmission electron microscopy (TEM) and electron diffraction. The microstructures of three sets of thin films with different chemical compositions were investigated - viz., PZT 53/47 films with no excess PbO; PZT 53/47 with excess PbO; and PZT 65/35 with no excess PbO. All samples were deposited on Pt substrates and were fired for 30 min. at temperatures from 400C to 700C.

The microstructures of PZT 53/47 films containing no excess PbO, fired at 450, and 700C are shown in Fig. A-2. The image of the film fired at 450C is featureless save for faint dark regions about 100 nm in size. As indicated above, the occurrence of the dark and light regions may reflect phase separation into relatively PbO-rich and PbO-poor regions. The electron diffraction pattern (not shown) indicates the film to be amorphous.

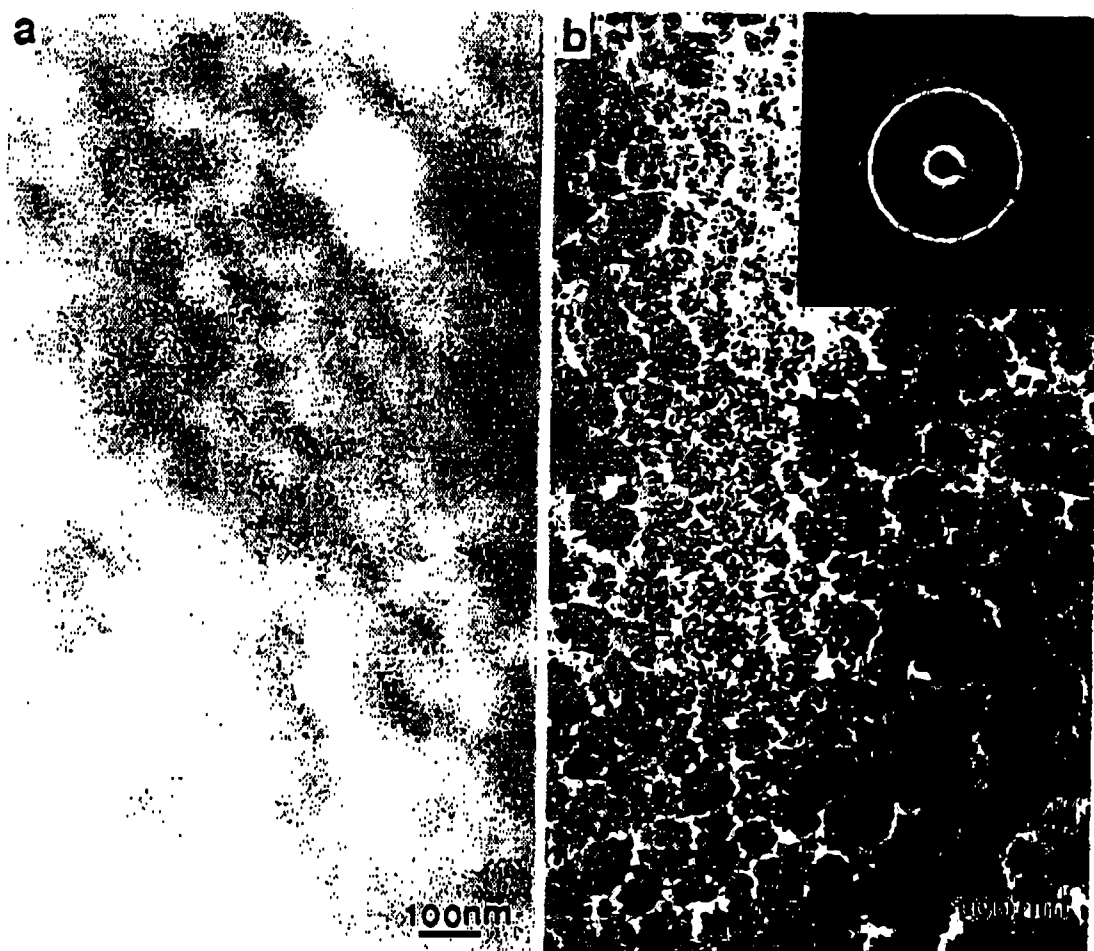


**Fig. A-2 Plan View TEM Images of PZT 53/47 Films fired at (a) 450C, and (b) 700C**

In contrast, the film fired at 700C consists of two distinct crystalline phases. The phase of higher density, which appears darker in the micrograph,

has a roughly - spherical morphology and comprises about 80 vol. % of the film. The selected area electron diffraction pattern, shown in the inset of Fig. A-2b, is a ring pattern corresponding to polycrystalline perovskite PZT mixed with a pyrochlore phase ( $\text{PbTi}_3\text{O}_7$ , cubic). The innermost ring has the highest intensity, indicating a preferred  $\langle 100 \rangle$  orientation and likely reflecting an epitaxial relation with the underlying Pt layer which has  $\langle 200 \rangle$  orientation. These TEM results are in good agreement with the X-ray diffraction data, which show the presence of perovskite and minor traces of pyrochlore.

Fig. A-3a shows a cross-sectional view of the PZT 53/47 film of Fig. 2b. The film is seen to consist of polycrystalline grains about 50 nm in diameter and >200 nm long. The grains grow along the direction perpendicular to the interface. The corresponding electron diffraction pattern shown in Fig. A-3b indicates a perovskite single crystalline pattern viewed along the  $\langle 110 \rangle$  direction. The splitting and/or elongation of most diffraction spots reflects misalignment of the grains along the viewing direction.



Fig. A-3 Cross-sectional TEM Image (a) and Electron Diffraction Pattern (b) of PZT 53/47 Film fired at 700C for 30 min.

PZT 53/47 films with excess PbO, having a stoichiometry of  $\text{Pb}_{1.15}\text{Zr}_{0.53}\text{Ti}_{0.47}\text{O}_{4.5}$ , have significantly different microstructures. Fig. A-4 shows a series of TEM images and corresponding electron diffraction patterns of such films fired at 400, 450, and 700C, respectively. At 400C, the films are crystalline and have a small grain size ranging from 30 to 100 nm. Grain boundaries are decorated by precipitates, 5-10 nm in diameter, possibly reflecting segregation of the remnant pyrochlore phase or excess PbO. The corresponding electron diffraction shown in Fig. A-4b indicates the presence of mainly polycrystalline pyrochlore mixed with some perovskite.



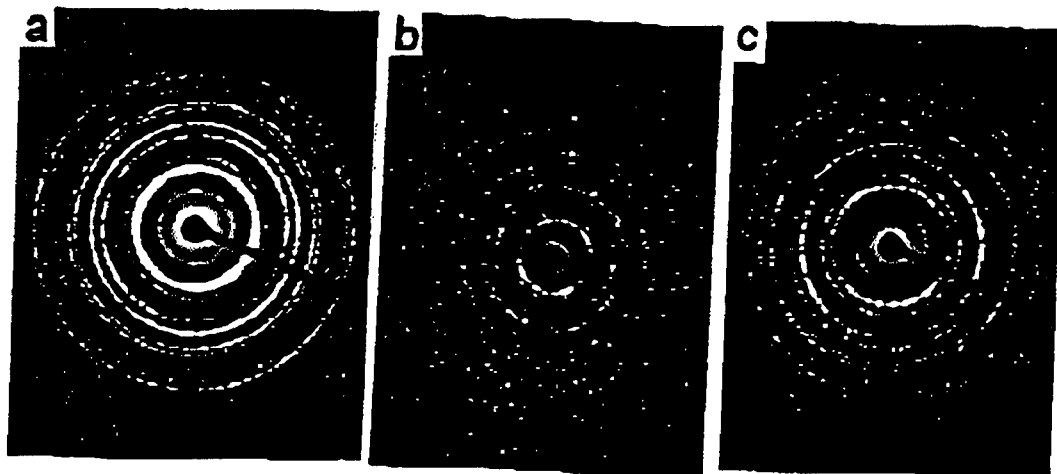


Fig. A-4 Selected Area Electron Diffraction Patterns of PZT 53/47 films with excess PbO, fired at (a) 400C, (b) 450C, and (c) 700C

When fired at 450C, the films have a polycrystalline structure with a slightly larger grain size. This sample contains a higher density of decorated precipitates at the grain boundaries than films fired at 400C. The diffraction pattern, shown in Fig. A-4b, indicates that the sample consists mainly of perovskite, with some pyrochlore present. At a firing temperature of 700C, the grains were larger, with a notable decrease in the number of precipitates at the grain boundaries. The electron diffraction pattern shows only perovskite. Twinning was observed occasionally in these films; but well-ordered domains

were not observed in any of the samples.

The effect of excess PbO on the microstructure is illustrated by comparing the microstructures of Figs. A-2b and A-3b. The excess PbO enhances grain growth and hence results in higher domain wall mobility. It also promotes the formation of single-phase perovskite, which produces a marked improvement in the dielectric constant - from  $\epsilon_r \approx 1000$  in the films without excess PbO to  $\epsilon_r \approx 2500$  for films with excess PbO, for films fired at 700C.

The PZT 65/35 films with no excess PbO, fired at 700C, have a drastically different structure compared to the other films. They contain numerous perovskite PZT rosettes embedded in a pyrochlore matrix. Fig. A-5 shows the general morphology of a rosette about 15  $\mu\text{m}$  in diameter, much larger than diameters of 3-4  $\mu\text{m}$  observed in other work [1,2], and very much larger than the film thickness of about 540 nm.



**Fig. A-5** TEM Image and Electron Diffraction Pattern of Perovskite "rosette" in PZT 65/35 Film fired at 700C.

The electron diffraction pattern of the rosette, shown in the inset, indicates a single crystal of perovskite viewed along the  $\langle 100 \rangle$  direction. The splitting of the diffraction spots indicates a slight misalignment of the rosette. Fig. A-6a shows that the matrix of the film is a mixture of two interpenetrating phases, approximately 50 nm in size. The electron diffraction pattern, Fig. A-6b, indicates that the matrix contains small grains of a pyrochlore phase. Due to the preponderance of the pyrochlore phase, the film exhibits a low dielectric constant of only 600.

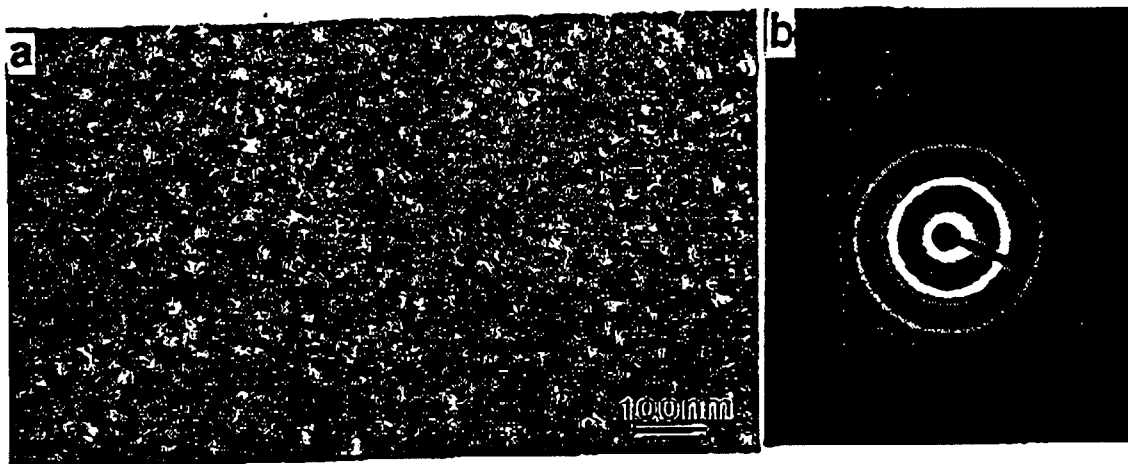


Fig. A-6 TEM Image (a) and Electron Diffraction Pattern (b) of the Pyrochlore-containing Matrix of PZT 65/36 Film fired at 700C.

The PZT 53/47 films synthesized with excess PbO exhibit  $\epsilon_r \approx 2500$  when fired to 700C and  $\epsilon_r \approx 3000$  when fired to 750C. The leakage currents of these films are exceptionally low, typically about  $1 \times 10^{-9}$  A/cm<sup>2</sup> at an applied field of 100 kV/cm. The combination of exceptionally high  $\epsilon_r$  and exceptionally low leakage current makes these PZT films highly attractive for a range of applications; and efforts to explore some of these applications have been initiated with two companies (see discussion in Section I above).

## Electrical Characterization

The dielectric constants,  $\epsilon_r$ 's, of PZT films with varying Zr/Ti ratios deposited on Pt substrates fired to 700C are shown in Fig. A-7 as a function of the Zr/Ti ratio. The  $\epsilon_r$  shows a maximum at the morphotropic phase boundary (MPB), PZT 53/47, and decreases with increasing Zr or Ti content away from this composition. This trend follows the behavior of bulk samples (also shown in Fig. A-7). Note that the  $\epsilon_r$ 's of the present films are consistently higher than those of their corresponding bulk ceramic counterparts regardless of the Zr/Ti ratio, attesting to the high degrees of purity and stoichiometry in these films.

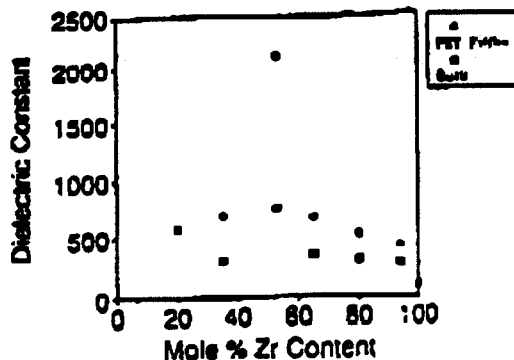


Fig. A-7 Dielectric Constants of Sol-Gel derived PZT Films fired to 700C as a Function of Zr Content. Also shown for Comparison are the Values for Bulk Ceramics of the same Compositions.

The remanent polarization and coercive fields of the PZT films fired to 700C are shown in Fig. A-8. Both the remanent polarization and coercive field are highest near the MPB. Being antiferroelectric,  $\text{PbZrO}_3$  films exhibit low values of  $P_r$  and  $E_c$ .

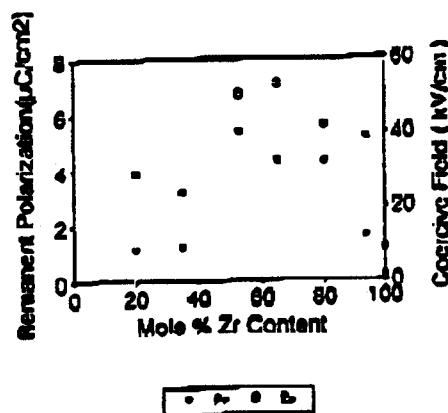


Fig. A-8 Remanent Polarizations and Coercive Fields of Sol-Gel derived PZT Films fired to 700C as a Function of Zr Content.

Note that the PZT ferroelectric capacitors, being non-linear dielectrics, do not exhibit ohmic or linear resistance - i.e., the resistance depends not only on the applied field but also on the electrical history, namely the polarization state. The films show a rapid rise of current at low voltages and an exponential dependence at higher voltages, reflecting the presence of a Schottky barrier at the PZT-Pt interfaces.

Fig. A-9 shows the bulk resistivities of PZT films fired to 700C as a function of Zr content. The resistivities are mostly in the range  $10^{10}$ - $10^{11} \Omega$ .

cm. Such values are notably higher than those reported in the recent literature, e.g.  $10^8 \Omega\text{-cm}$ , and reflect a high level of homogeneity/stoichiometry as well as the large grain size of the present films. The resistivities increase with increasing Zr content, reaching  $2.5 \times 10^{11} \Omega\text{-cm}$  for a  $\text{PbZrO}_3$  film, while  $\text{PbTiO}_3$ -rich films tend to be relatively conductive.

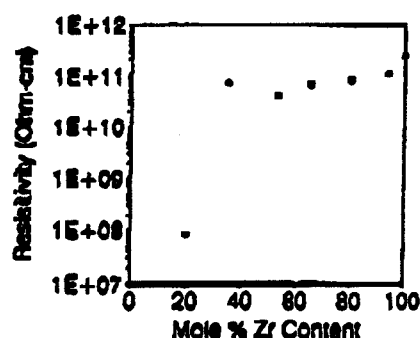


Fig. A-9 Bulk Resistivities of Sol-Gel derived PZT Films fired to 700°C as a Function of Zr Content.

The resistivity is a strong function of domain structure and microstructure. While the  $\text{PbZrO}_3$ -rich films tend to be biphasic, consisting of rosettes and an intergranular phase, their composite resistivities are quite high ( $10^{11} \Omega\text{-cm}$ ). The  $\text{PbTiO}_3$  films are not fully densified even when fired to 700°C; and  $\text{PbTiO}_3$ -rich films develop severe stresses from the highly anisotropic  $c/a$  lattice ratio upon cooling below their Curie temperatures ( $T_c$ ). Microcracks can occur, leading to conductive paths between electrodes. The

microstructures of the  $\text{PbZrO}_3$ -rich ( $\text{Zr} > 53$  mole %) films contained rosettes whose size increased with increasing Zr content. The increase of resistivity with grain size reflects the fact that with larger grains there are fewer grain boundaries to serve as conduction pathways.

The fatigue and retention behaviors of the PZT films were also analyzed based on  $P^*$ , the difference between the maximum polarization in one polarity and the remanent polarization,  $P_r$ , in the reverse polarity as a function of cycling or time. Note that  $P^*$  is a strong function of the applied voltage (or field), since the voltage determines the maximum polarization achieved. The voltage applied to the films was preset to 8 V. The values of  $P^*$  measured for the films as a function of Zr content and processing temperature, namely 700 and 750C, are shown in Fig. A-10.

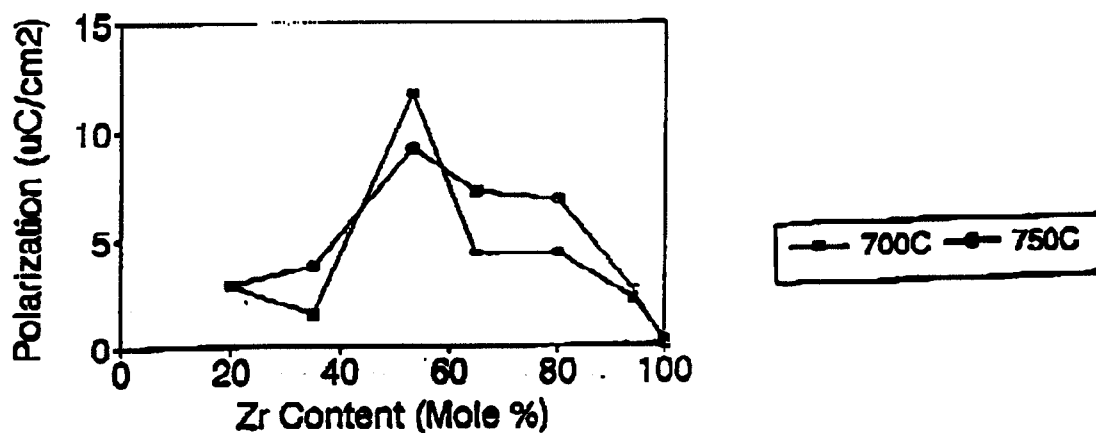


Fig. A-10 Values of Polarization ( $P^*$ ) of PZT Films as a Function of Zr Content and Firing Temperature.



The polarization  $P^*$  reaches a maximum value at the composition of the morphotropic phase boundary. As expected, the polarization values are higher for films fired at higher temperature than for those fired at lower temperature. This reflects the enhanced crystallinity and large grain sizes obtained on firing at the higher temperature.

Figs. A-11a and A-11b show the effects of cycling, using 8 V amplitude, 100 kHz square waves, on the values of  $P^*$  for a series of PZT films with different stoichiometries. The polarizations after fatiguing have been normalized with respect to the polarization values of the virgin capacitors. It is seen that films fired to higher temperatures are less susceptible to the deleterious effects of fatigue, i.e., the monotonically decrease in polarization with continuous cycling. In both sets of films fired to 700C and 750C, films with compositions removed from the MPB display superior fatigue resistance: PZT 53/47 films exhibit the fastest decrease in polarization with cycling. The fatigue behavior was superior for films fired at higher temperatures compared with those fired at lower temperatures.

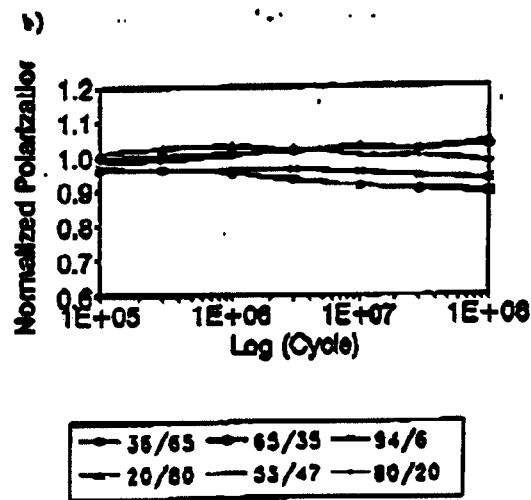
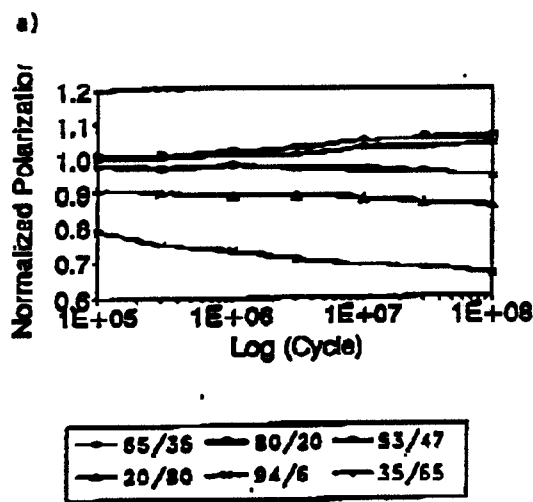


Fig. A-11 The Effect of Fatigue on Values of Normalized  $P^*$  in various PZT Films fired to (a) 700C and (b) 750C for 30 min.

For films fired at 700C, rhombohedral PZT films (with high Zr/Ti content) have superior fatigue resistance compared with tetragonal films. In contrast, for films fired at 750C, the observations are reversed, i.e., tetragonal films exhibit better fatigue resistance than rhombohedral films. It has been documented that in PZT films, the partial pressure or activity of PbO increases with Zr content, and hence leads to more significant PbO loss (arising from PbO volatility and/or diffusion into substrates) when fired to higher temperatures. Thus at higher firing temperatures, the PbO diffusion into Pt substrates tends to be exacerbated in rhombohedral PZT films and render these films more conductive due to formation of Pb vacancies.

The retention behaviors of PZT films fired to 700C and 750C are shown in Figs. A-12a and A-12b, respectively. The polarizations are again normalized with respect to their initial values. Films near the MPB composition tend to exhibit domain structures with the highest domain wall mobility (which enhances the values of  $\epsilon_r$ , piezoelectric coefficients and dielectric loss); hence the films are expected to show the highest rate of domain relaxation upon voltage pulsing which then results in poor retention behavior. On the other hand, PZT films with the highest tetragonal and rhombohedral characteristics tend to exhibit domain structures which are essentially clamped due to the high crystal anisotropy which in turn retard domain relaxation or realignment after voltage pulsing.

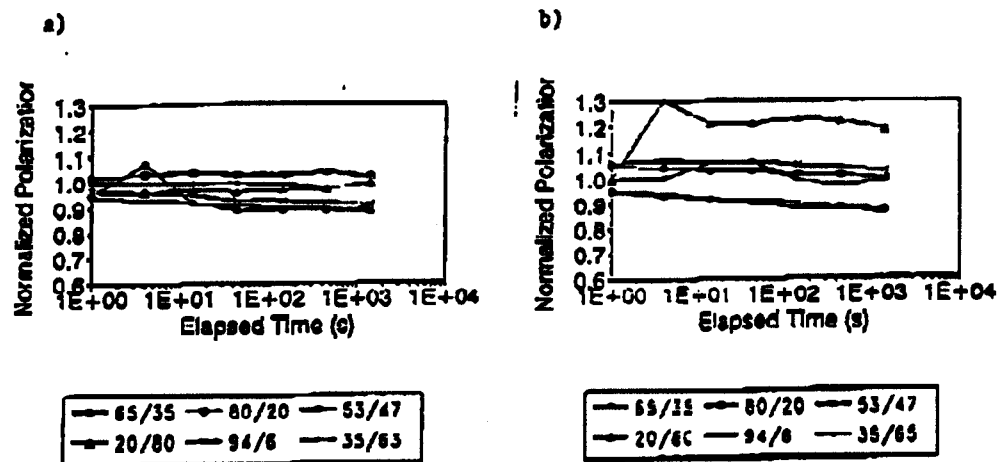


Fig. A-12 Retention Behavior of Various PZT Films fired to (a) 700C and (b) 750C.

In addition to investigating the electrical properties of PZT films of various Zr/Ti stoichiometry ratios, PLT and PLZT films obtained via the incorporation of La were also explored for their wide and fascinating range of electrical properties.

The small-signal values of dielectric constant and dissipation factor (measured at 5 mV oscillation level) of various PLT films fired to 700C are shown in Fig. 12. The dielectric constant increased with La content. This is associated with the shift of  $T_c$  toward room temperature with increasing La content. The dielectric constants of the PLT films fired to higher temperatures, namely 750C, exhibited about the same values, except for PLT 28 which reported a decline to 550 (fired at 750C) from 838 (fired to 700C) due to PbO loss into the Pt substrates. Note that PLT 28 is on the ferroelectric (FE) - paraelectric (PE) boundary. Such films are expected to be non-FE, which explains their lower dissipation factors. At higher oscillation levels (or large signal values), the dissipation factors of the ferroelectric PLT films with <28 mole % La (~0.12) are about four times the value (~0.03) of a PLT 28 film. The larger values of dissipation factor at large ac fields reflect loss arising from partial switching of the domains resulting in domain wall motion.

**Fig. A-13 Dielectric Constant and Dissipation Factor of PLT Films with Various La Contents fired to 700C.**

The remanent polarizations,  $P_r$ , and coercive fields,  $E_c$ , of PLT films are shown in Fig. A-14. The values of  $P_r$  and  $E_c$  exhibit a steady decrease with increasing La content, reaching almost zero values at 28 mole % La. The decrease in both  $P_r$  and  $E_c$  can be explained by the lower tetragonality,  $c/a$  (approaching unity) with increasing La incorporation in the perovskite lattice.

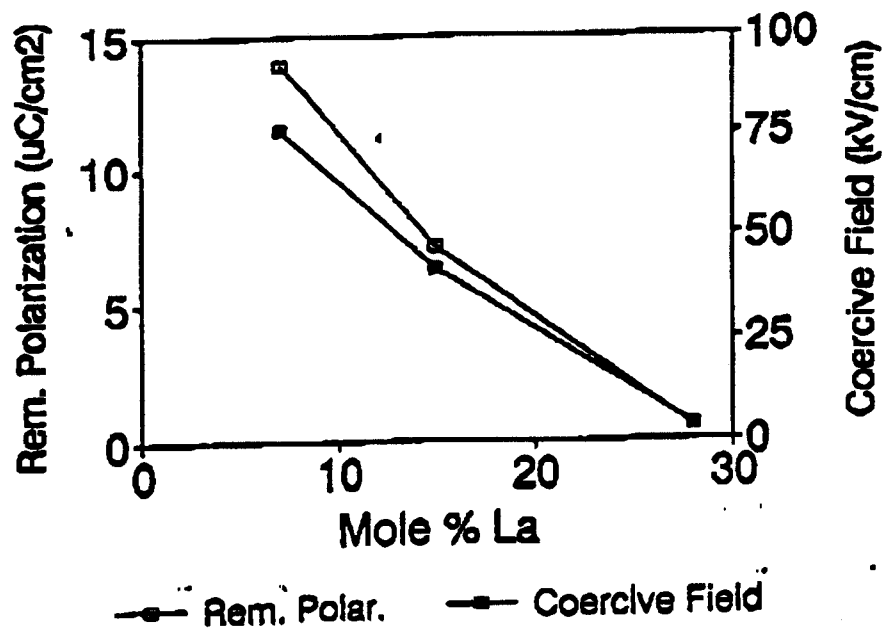


Fig. A-14 Remanent Polarization,  $P_r$ , and Coercive Field,  $E_c$ , of PLT Films with Various La Contents fired to 700°C.

The PE or non-FE nature of the PLT 28 film affected the frequency response of its dielectric properties. Due to the absence of domains, the dielectric constant was independent of measuring frequency over the range 500 Hz to 100 kHz, as shown in Fig. A-15. In contrast, as also shown in Fig. A-15, the dielectric constants of a FE PLZT 1/53/47 film exhibited dispersion, i.e., a monotonic decrease in dielectric constant with increasing frequency. PLT films are attractive for microelectronic applications, where frequency-independent capacitive devices are required.

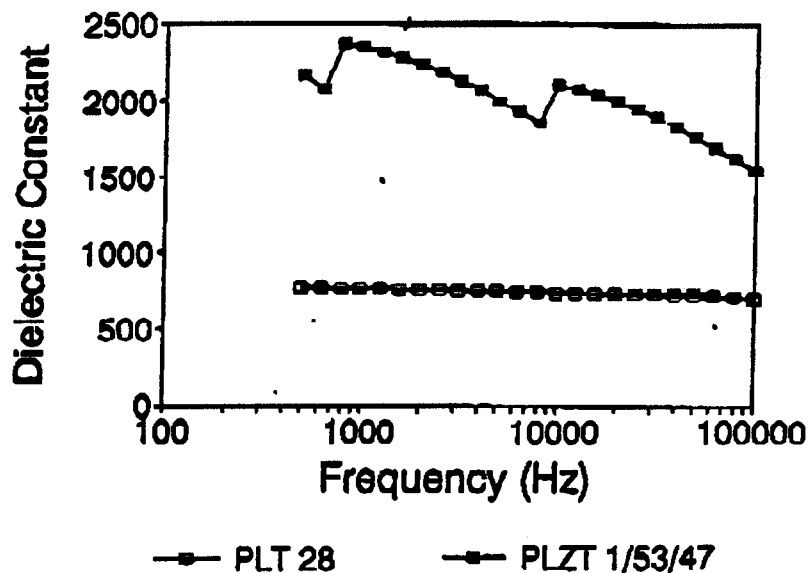


Fig. A-15 Effect of Frequency on the Dielectric Constants of PLT 28 and PLZT 1/53/47 Films fired to 700C.

The effects of applied dc bias on the dielectric properties are shown in Fig. A-16. For both PE and FE films, the dielectric constants decreased at large applied biases, with the FE films (typified by PLZT 1/53/47), exhibiting higher sensitivity to the dc bias. For example, the PLT 28 film exhibited only ~40% decrease in  $\epsilon_r$ , while the FE PLZT 1/53/47 film showed a 60% decline. Both films are non-centrosymmetric and polar; hence they are expected to show dielectric saturation, namely the decline of dielectric constant at high fields. However, the level of dielectric saturation is lower in PLT 28 than in the ferroelectric PLT films due to the absence of domains in the PLT 28 films

(with the presence of domains, domain realignment can take place under an applied field and results in a lowering of  $\epsilon_r$ ).

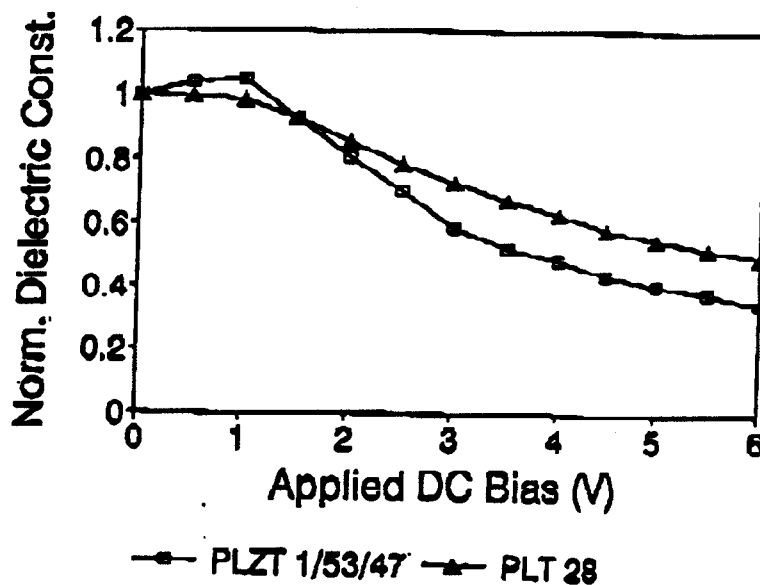


Fig. A-16 Effect of DC Bias on the Dielectric Constants (Normalized to Values at OV Applied Bias) of PLT 28 and PLZT 1/53/47 Films fired to 700C.

A dependence of the dielectric properties of PLT films on electrode geometry was also observed. The effect of Pt electrode area on  $\epsilon_r$  and dissipation factor of a PLT 28 film fired to 700C is shown in Fig. A-17.  $\epsilon_r$  is seen to increase and the dissipation factor to decrease with decreasing electrode area. This can be attributed to a higher probability of film defects



existing in larger area capacitors. However, data obtained on ferroelectric PZT 53/47 films indicated that the dielectric properties were nearly independent of electrode area. Work is currently being carried out to reconcile these observations.

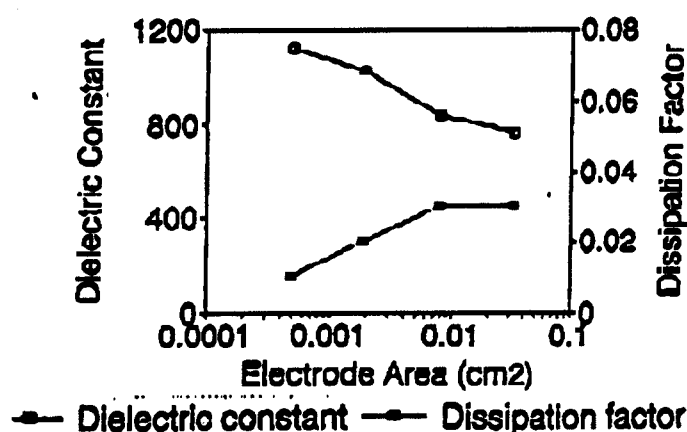


Fig. A-17 Values of Dielectric Constant and Dissipation Factor of PLT 28 Films fired to 700C Measured on Capacitors having Different Electrode Areas.

The leakage current increases with increasing concentration of La in the FE films (see Fig. A-18). Since  $\text{La}^{3+}$  is an off-valent donor substituting for  $\text{Pb}^{2+}$  in the perovskite phase, its incorporation results in more n-type behavior. The lowest leakage current was exhibited by PLT 28 films, likely because they are paraelectric and thus free of domains. The leakage current of the PLT 28 film was about an order of magnitude lower than that of the best FE films

(e.g., PLZT 1/53/47). This suggests the utility of paraelectric films as capacitor materials in DRAM applications where the leakage current must be minimized.

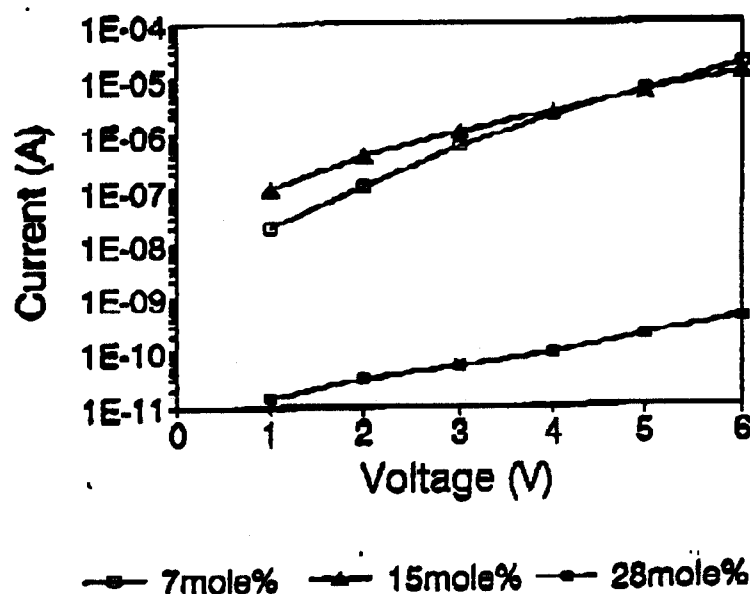


Fig. A-18 Leakage Characteristics of Various PLT Films fired to 700C for 30 min as a Function of Applied Voltage and La Content.

Also explored during the present year were the effects of post-metallization annealing (PMA) on the electrical properties of Pt-PZT(53/47)-Pt capacitors. Conventionally most PZT films are PMAed, usually at the same temperatures where the films are fired. To now, however, there has been no systematic study of the effects of such annealing on the dielectric and FE

properties of the capacitors. For monolithic Pt-PZT-Pt capacitors, the bottom Pt-PZT interface has a different thermal history compared to the top Pt-PZT interface, since the bottom interface undergoes heat treatment during crystallization of the PZT film. If no PMA involving comparable heat treatment is performed, these two interfaces should be quite different in their characteristics, e.g., barrier heights, degree and extent of interfacial diffusion, and interface state density. Additionally, when the polarity of the applied field is reversed on these capacitors, the resulting leakage characteristics may not be symmetrical due to different Schottky barrier heights at the two interfaces.

X-ray diffraction results indicated that films fired to 700C were single-phase perovskite, and PMA of these films up to 700C did not produce any other phase. Optical microscopy showed that films fired at high PMA temperatures exhibited larger grain sizes ( $7.5 \mu\text{m}$  at 700C) than films PMAed at low temperatures ( $5 \mu\text{m}$  at 100C).

The values of spontaneous polarization,  $P_s$ , remanent polarization,  $P_r$ , and  $\epsilon_r$  as functions of PMA temperature are shown in Fig. A-19. These dielectric properties are seen to decrease with increasing PMA temperature. The decay of the polarizations and  $\epsilon_r$  with increasing PMA temperature cannot be explained by the larger grain sizes, since FE properties should be enhanced

in larger grain size films. Rather, the observed effect can be attributed to Pb diffusion at the Pt-PZT interfaces, the degree of which increases with increasing PMA temperature.

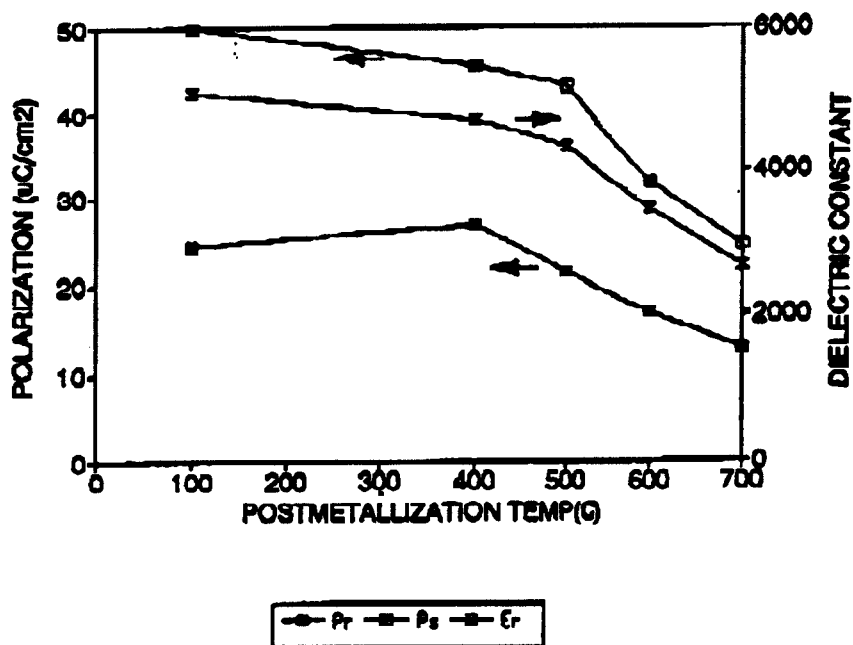


Fig. A-19 Effect of PMA on Remanent Polarization,  $P_r$ , Spontaneous Polarization,  $P_s$ , and Dielectric Constant,  $\epsilon_r$ , of PZT 53/47 Films fired to 700C.

As shown in Fig. A-20, the bulk resistivities ( $\rho$ ) at 8V applied voltage increased monotonically with annealing temperature. At higher PMAa temperatures (i.e., >400C), the increase in  $\rho$  can be as high as a factor of 10 per 100C. The  $\rho$ 's shown in Fig. A-20 are large-signal values and assume the

To date, most studies of POLYCERAMS have focussed on their structural characteristics and thermal/mechanical properties. Relatively little attention has been directed to the optical properties of this novel class of materials. In this phase of the present program, we have investigated the optical properties and waveguiding characteristics of POLYCERAMS prepared in the form of planar waveguides. The planar waveguide is the fundamental component which connects the various elements of an integrated optical device. In many applications, ranging from optical data storage to communications, the planar waveguide forms an important element in the fabrication of complicated optical circuits. We have found (to our pleasant surprise) that despite the disparate chemistry of their constituents, POLYCERAMS exhibit remarkable waveguiding characteristics with very low optical losses. In addition, the optical properties of these waveguides - including their refractive indices and dispersion characteristics - can be varied over a wide range through variations in chemistry and processing.

During the present year of the grant, a large number of POLYCERAM systems have been explored. These have been based on the oxides of Si together with those of Ti, Ge, Ba, Pb, Zn and Zr as the inorganic species, and MPEOU or PDMS (polydimethyl siloxane) as the organic constituents. In

The properties of these materials can be varied over a wide range by varying the volume fractions of the constituents as well as their chemistries, molecular weights, synthesis conditions, etc. POLYCERAMS are usually synthesized from solutions of the constituents and provide exceptional drying behavior, which permits the easy fabrication of crack-free monoliths and films of arbitrary thickness. As an example, Fig. B-2 shows a POLYCERAM monolith synthesized from tetrathoxysilane (TEOS) and N-triethoxysilylpropyl-modified poly(ethylene oxide) urethane (MPEOU). The materials are processed at low temperatures (typically near ambient), and exhibit - for example - enhanced thermal and photostability, increased hardness, improved scratch resistance and exceptional adhesion to inorganic surfaces as compared with the constituent organic species.

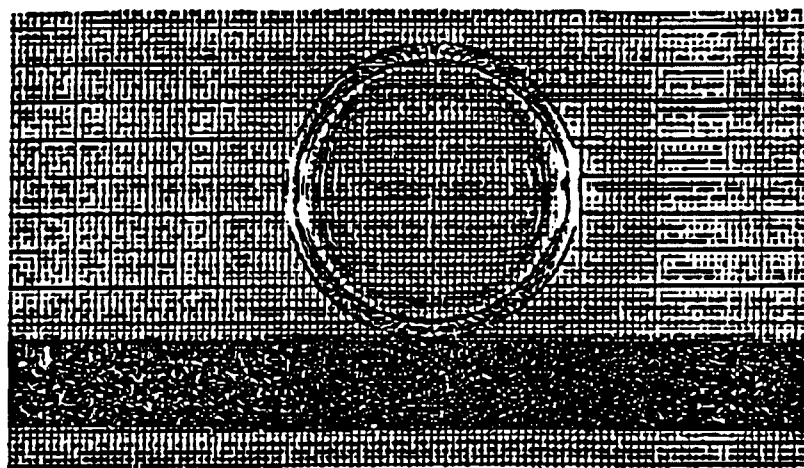


Fig. B-2 Monolithic TEOS/MPEI polyceram.

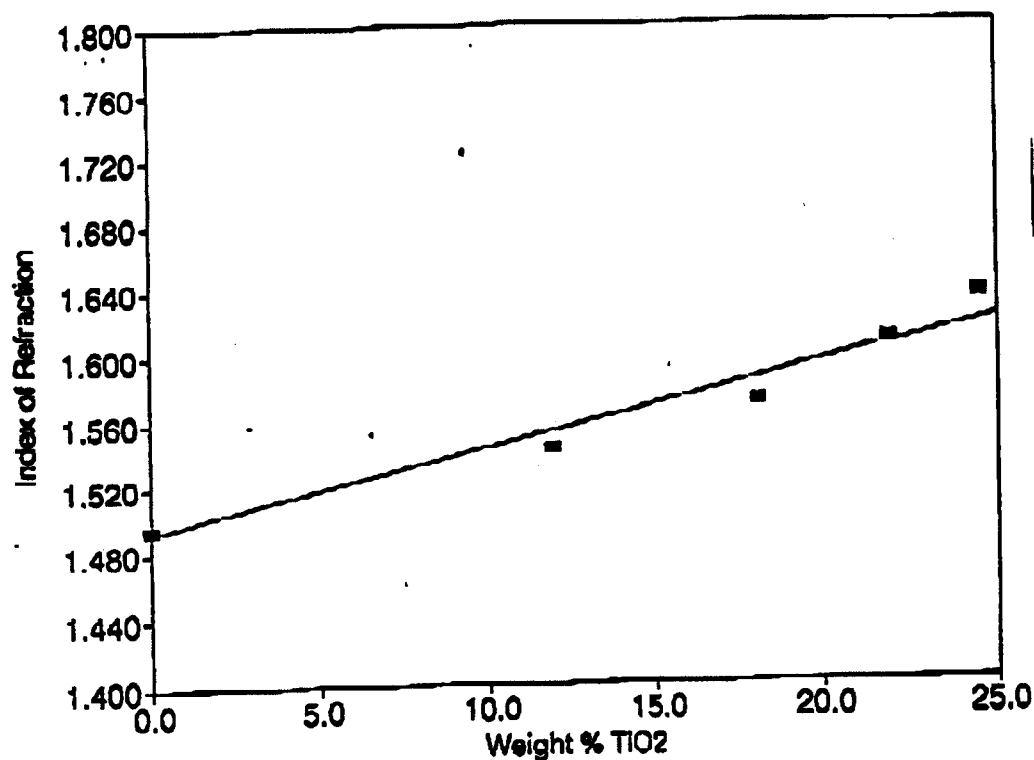


Fig. B-4 Linear increase of the index of refraction with TiO<sub>2</sub> content of SiO<sub>2</sub>-TiO<sub>2</sub>-MPEOU POLYCERAMS incorporating 80 % volume MPEOU.

The variation of the refractive index with SiO<sub>2</sub>-TiO<sub>2</sub> molar ratio of the inorganic component was also investigated for POLYCERAMS containing 60 vol. % polymer. As illustrated in Fig. B-5, the refractive index again increases approximately linearly with increasing TiO<sub>2</sub> content. As expected, the indices of refraction of POLYCERAMS containing 60 vol. % MPEOU are higher than

previous years, we investigated POLYCERAMS synthesized with other polymers, but these did not exhibit the high optical clarity of those synthesized using MPEOU or PDMS. In recent weeks, exploration has been initiated of POLYCERAMS based on a number of acrylic polymers.



capacitors are ohmic at both Pt-PZT interfaces. If the capacitors are non-ohmic, such bulk  $\rho$ 's are physically meaningless, since the current would depend on the rectifying interfaces and hence on the voltage. A more useful parameter is the leakage current at fixed voltage or field.

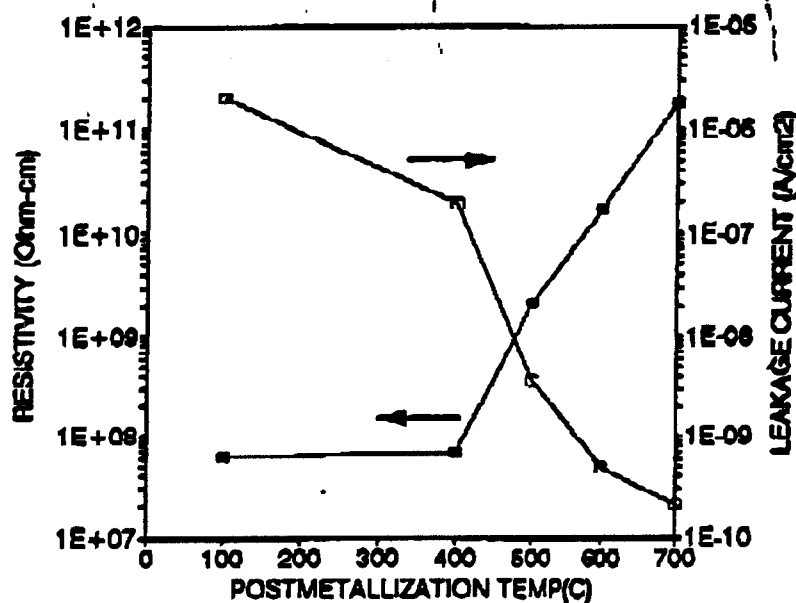


Fig. A-20 Effect of PMA on the Resistivity and Leakage Currents (8V) of PZT 53/47 Films fired to 700C.

The leakage currents of such capacitors PMAed at various temperatures are shown in Fig. A-20. It is clear that the resistivity and leakage current increase and decrease respectively with increasing PMA temperature. It was

found, however, that in films containing high concentrations of Zr, the leakage currents increase with post-metallization annealing temperature. This is shown in Fig. A-21 for a PZT 35/65 film. Upon post-metallization firing to 700C (the same temperature at which the films were originally fired), the leakage current increases by about 4 orders of magnitude, while lower firing temperatures (i.e., 100C-400C) resulted in insignificant changes. In films containing higher concentrations of Zr, the increase in leakage current is exacerbated even at lower PMA temperatures (e.g., 400C). This is due to the diffusion of Pb into the Pt electrodes - an effect which becomes more significant with increasing Zr content. Such diffusion not only affects the PZT-Pt interfaces, but also renders the PZT films more conducting due to Pb vacancies resulting from the Pb loss.

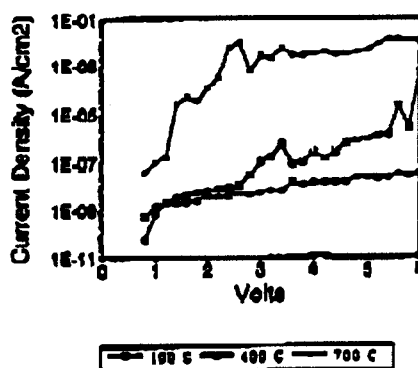


Fig. A-21 Effect of Post-Metallization Annealing Temperature on the Leakage Current of Sol-Gel Derived PZT 35/65 Films fired to 700C.

Fig. A-22 shows the I-V characteristics of the Pt-PZT 53/47-Pt capacitors PMAed to 100C and 700C at both polarities (the positive and negative voltages applied with respect to the Pt substrate). The currents decreased dramatically with higher PMA temperature; and the I-V characteristics tended to be more symmetric (less polarity-dependent) when the capacitors were fired to higher temperatures. In the capacitors fired to 100C, the currents were quite polarity-dependent, with the currents at positive voltages being higher than when negatively poled. PMA temperatures >400C are sufficient to render the capacitors symmetric electrically.

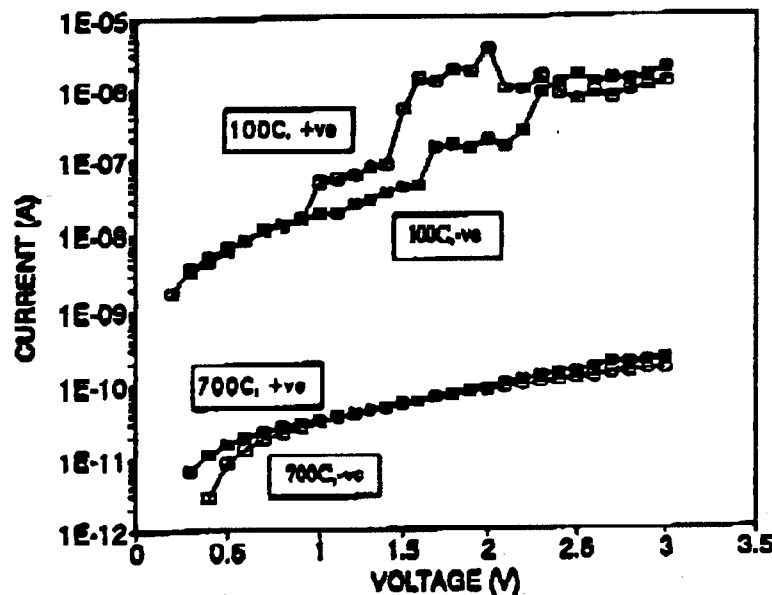


Fig. A-22 I-V Characteristics of Pt-PZT 53/47-Pt Capacitors

The fatigue behaviors of PZT 53/47 and PZT 35/65 films fired to 700C are shown in Figs. A-23 and A-24, respectively, before and after PMA at 400C

for 30 min. For PZT 53/47 films, post-metallization annealing seems to be deleterious to the overall fatigue behavior: for an unannealed film, the polarization decreased to only 0.93 of its initial value after  $10^8$  cycles, whereas for an annealed 53/47 film, the polarization dropped to 0.67 of its initial value after the same number of polarization reversals. The fatigue behavior of PZT films with stoichiometries different from PZT 53/47 appear less affected by such post-metallization annealing.

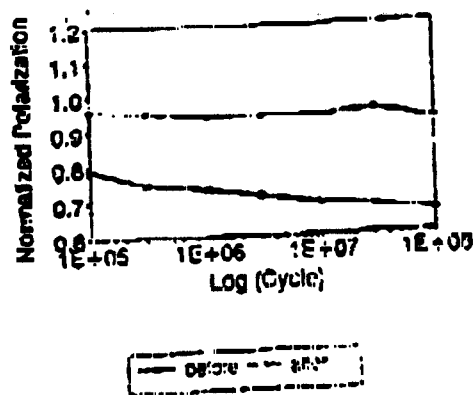


Fig. A-23 Fatigue behaviors of PZT 53/47 films fired to 700C.

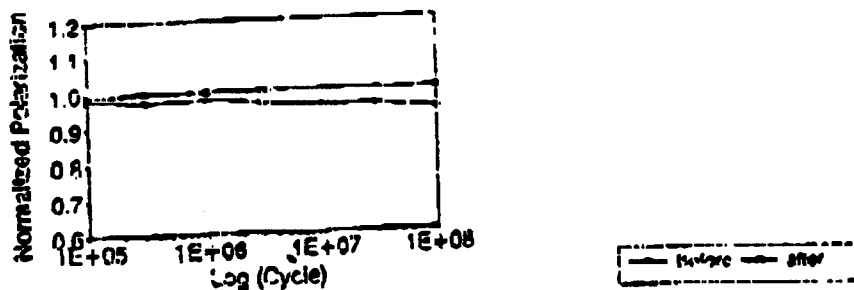


Fig. A-24 Fatigue behaviors of PZT 35/65 films fired to 700C.

## Optical Characterization

The optical characteristics of sol-gel derived PLZT films on Corning 7059 glass were also explored in some detail. The results of these explorations have yielded high quality crystalline and amorphous waveguides. Crystallization of the films is heterogeneously nucleated at the interface with the substrate as indicated by the (100) oriented films obtained on (200) oriented Pt substrates. The crystallization of both pyrochlore and perovskite phases is enhanced on crystalline substrates (e.g., Pt) and hindered on amorphous substrates (e.g., Corning 7059 glass).

The presence of La dramatically increased the overall transparency of the PLT films compared with PT films. The latter PT films become opaque on crystallization since the refractive index anisotropy of the crystallites is fairly large ( $\Delta n = -0.011$ ), and results in significant scattering. Additionally, the concomitant large anisotropy in lattice parameter ( $c/a$  ratio = 1.063) often leads to microcracks within the films on cooling (particularly for thick films), further enhancing the scattering. The addition of La decreases the lattice anisotropy, lowers the  $c/a$  ratio as well as the anisotropy in refractive index, and results in less cracking and scattering. Hence the transmission improved systematically with increasing La content. While the index difference between

stress becomes compressive when Pt is used.

The refractive indices  $n$  of PZT 53/47 and PLT 28 films on Corning

pyrochlore and amorphous or perovskite phases remained large, none of the pyrochlore-containing films were opaque or translucent since the amount of pyrochlore in most of the films was miniscule.

While crack-free films ( $\sim 2500\text{\AA}$ ) of PT and PLT can routinely be obtained on Corning 7059 glass, Zr-containing films tended to crack, especially when fired above  $500^\circ\text{C}$ . In contrast with films on Corning 7059 or fused  $\text{SiO}_2$ , crack-free films of any PZT composition up to  $1\text{ }\mu\text{m}$  thick can be routinely obtained on platinized Si wafers by multiple coating. The reason for the cracking lies in the mismatch in thermal expansion coefficient between the PZT films and the substrates. The thermal expansion coefficient increases with

Similar behavior was observed in other non-Zr-containing films; while films containing Zr such as PZT, PLZ or PLZT displayed maxima in  $n$  (usually at 400-450C) before decreasing at higher firing temperatures ( $>450C$ ), reflecting PbO loss from the films. The incorporation of La into PT and PZT to form PLT and PLZT usually resulted in lower values of refractive index due to their lower densities.

The refractive indices of various PZT films fired to 450C are shown in Fig. A-26 as a function of Zr/Ti ratio. The indices showed a monotonic decrease from 2.33 in a PT film down to 2.10 in a PZ film. Except for the PT film (which consisted of biphasic perovskite and pyrochlore), the rest of the PZT films in Fig. A-26 were amorphous. The refractive indices of these amorphous films were lower than those of their crystalline ceramic counterparts (2.67 and 2.42 for PT and PZ respectively). The trend of decreasing  $n$  with increasing Zr content in PZT films has been reported by others, and reflects a decrease in density with increasing Zr content.

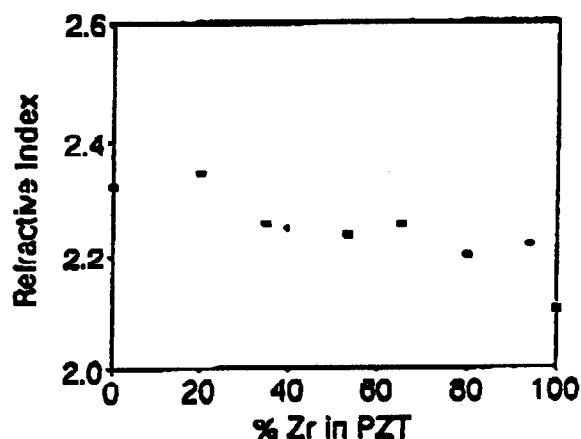
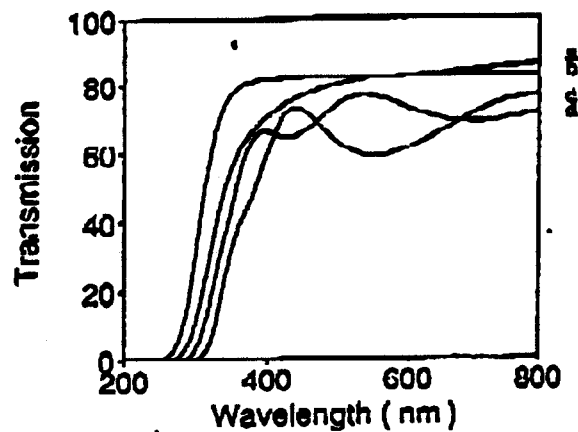


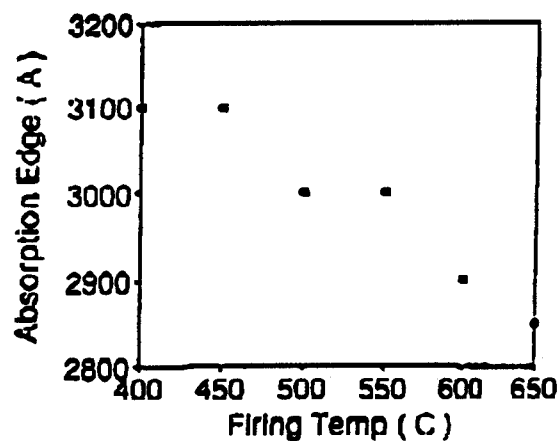
Fig. A-26 Variation of Refractive Index With Zr Content of PZT Films fired to 450C

Fig. A-27 shows the UV-VIS transmission spectra of the Corning 7059 substrate, a PbO-infiltrated Corning 7059 substrate obtained by firing a PbO film to 600C and diffusing the entire film into the substrate, and PLZ 28 and PLT 28 films fired to 500C. Note that PLT 28 exhibited the highest UV cutoff at about 3200Å; while the cutoffs for PLZ 28 and PbO-infiltrated 7059 glass occur at shorter  $\lambda$ 's, - 2800 and 2700Å respectively. The UV cutoff of PZT 53/47 films shifted to shorter wavelengths (<2900Å) at higher firing temperature (Fig. A-28). The absorption edge of bulk pyrochlore  $\text{PbTi}_3\text{O}_7$  and as-sputtered PZT films has been reported to be in the range 3800-4500Å. Bulk PZT ceramics exhibit an absorption edge at 3400Å.





**Fig. A-27** UV-VIS Transmission Spectra of a) Corning 7059 Glass; b) PbO Film Defused into Corning 7059 Glass Substrate; and c) PLT 28 and d) PLZ 28 Films fired to 500C on Corning 7059 Glass.



**Fig. A-28** Variation of UV Absorption Edge with Firing Temperature for PZT 53/47 Films.

The effect of film thickness on the refractive index and absorption edge of PZT 53/47 films is shown in Figs. A-29a and A-29b, respectively. The refractive index increased and the absorption edge decreased in  $\lambda$  with decreasing thickness below 2000 Å, but tended to saturate in thicker films.

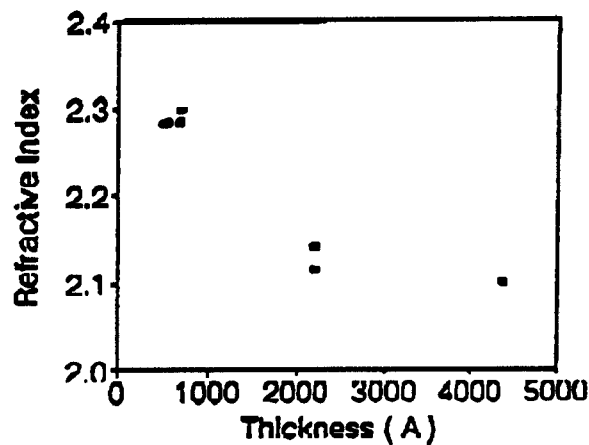


Fig. A-29a Variation of Refractive Index with Film Thickness  $n$  for PZT 53/47 Films fired to 500°C.

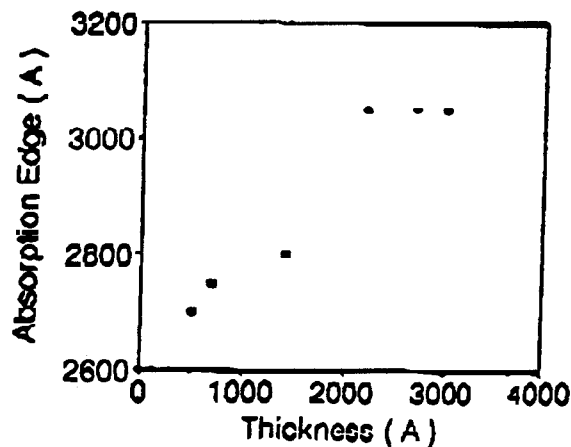


Fig. A-29b Variation of Absorption Edge with Film Thickness for PZT 53/47 Films fired to 500°C.

The dependence of the optical properties of PZT films on film thickness (particularly in thinner films) can be attributed in large measure to interfacial reaction between the films and the substrate. PZT film-substrate interaction has been documented for ITO and even Pt. It is postulated that PbO from the films diffuses into the substrates during firing, especially at higher processing temperatures. The partial pressure of PbO over the PZT films increases in the following order: PZ > PZT > PT. This trend indicates that the PbO diffusion is worse in materials with higher Zr contents. Such an expectation is validated by the results in Fig. A-30, which shows the transmission spectra of Corning 7059 substrates where the top PT, PZT 80/20 and PZT 53/47 films (fired to 500C) have been acid-etched away. The spectra shown in Fig. A-30 have been normalized to that of a Corning 7059 substrate.

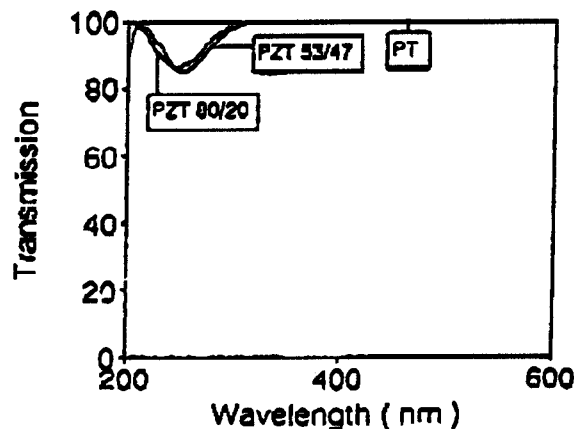


Fig. A-30 Normalized Transmission Spectra of Corning 7059 Substrates (with Respect to that of a Virgin Substrate) after Etching away PT, PZT 53/47 and PZT 80/20 Films fired at 500C.

The transmission of a substrate initially coated with PT is seen to be flat over the range of wavelength investigated, while that of substrates initially coated with PZT 53/47 and 80/20 films (but later etched away) indicated fairly strong absorbance at 2600-2700Å. This absorption can be attributed to PbO within the substrate (see Fig. A-27). Thus PbO diffusion was negligible from the PT film, but became significant from Zr-containing films. In thinner films, the interfacial layers would dominate the overall optical properties of the films. Since Corning 7059 is an aluminoborosilicate glass, there may be diffusion not only of PbO into the glass, but also diffusion of B or Al into the PZT films.

In Zr-containing films, the exacerbation of these interfacial layers led to a downward shift of the absorption edge and lower values of refractive index resulting from significant diffusion of PbO from the films. The resulting PbO-poor films were difficult to crystallize, especially into the desired perovskite phase. In contrast to the PbO film on Corning 7059 glass fired to 600C, which had completely diffused into the substrate, a similarly treated PbO film remained on fused SiO<sub>2</sub>, demonstrating the lower degree of PbO diffusion into SiO<sub>2</sub>. Correspondingly, a PT film on SiO<sub>2</sub> was single-phase perovskite when fired at 550C, a notably lower temperature than that (600C) needed to obtain single phase perovskite PT film on Corning 7059 glass.

It is seen that the presence of Zr in the films is deleterious to overall film properties. Zr not only exacerbates PbO diffusion from the films into the substrates but also retards crystallization and increases the tendency of cracking. For thin film applications, the choice of PLZT composition should in many cases be limited to the PLT series, which offer films with enhanced transparency compared to PT but reduced reaction with the substrate compared to PZT. In cases where crystalline Zr-containing PLZT films are required (e.g., to achieve large electrooptic coefficients), suitable barrier layers toward PbO diffusion or intermediate epitaxial films such as PLT should be employed. Rapid thermal annealing can also be used so that the kinetics of crystallization are much faster than the kinetics of PbO diffusion into the substrates. However, amorphous Zr-containing films can be used as passive waveguides since the notable absence of either grain or domain boundaries can lead to low losses.

Attenuation measurements of the PZT waveguides on Corning 7059 glass are shown in Table A-2. In the case of a PZT 53/47 film fired to 650C, which was amorphous, the loss was only 1.1 dB/cm. In amorphous PZT films, the losses are expected to be fairly low due to the absence of domain and grain boundaries (the discontinuities in index at domain and grain boundaries in

polycrystalline films can lead to significant scattering). The losses should then

... This expectation is confirmed by

be rectifying is in the presence of surface states (arising, e.g., from absorbed oxygen at the PZT surface and/or termination of the PZT crystalline lattice at the metal contacts). These surface states with a density of  $D_0$  and a neutral energy level at  $E_0$  result in band bending near the contacts and barrier heights of  $\phi_b$  at the interfaces. If it is assumed that the barrier heights are similar at both interfaces, the capacitor should exhibit symmetric electrical behavior - i.e., the behavior should be independent of the polarity of the applied voltage. If it is further assumed that the PZT film is depleted throughout its thickness, Poisson's equation can be solved to evaluate the charge distribution ( $\rho$ ), electric field ( $E$ ), potential ( $\phi$ ) and energy band diagram. The results of such calculations are shown in Fig. A-31 for the equilibrium case with no applied voltage.

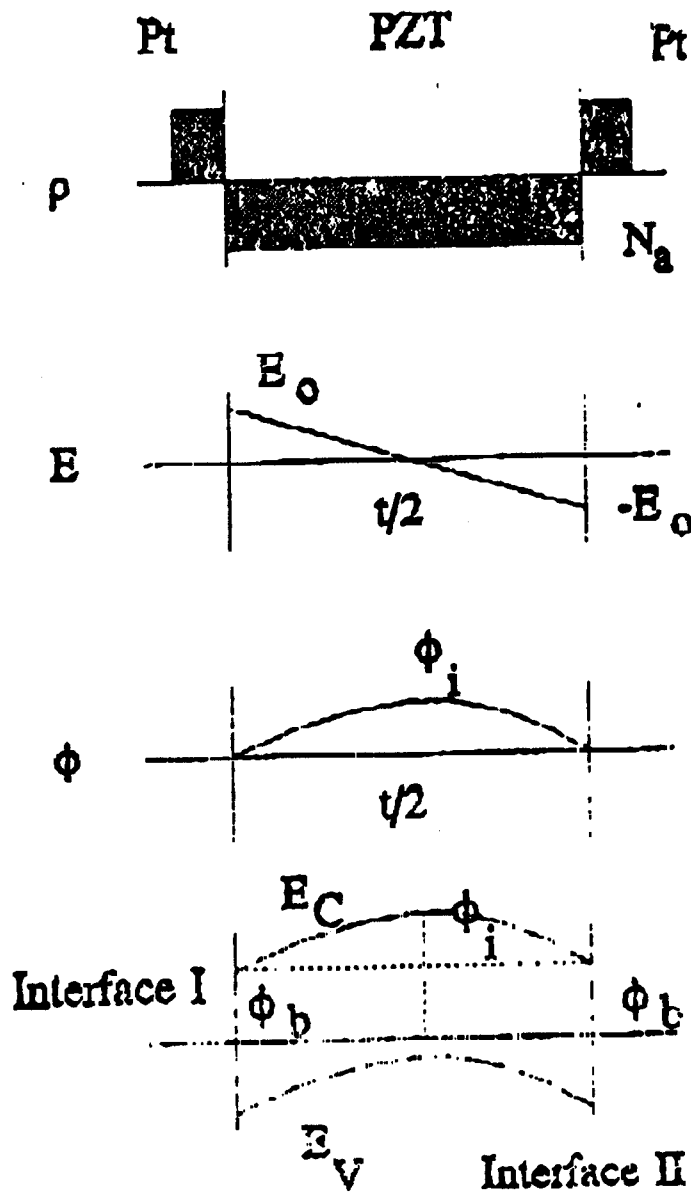


Fig. A-31 Solutions to Poisson's Equation for a wholly depleted PZT Film, showing the Charge Distribution ( $\rho$ ), Electric Field ( $E$ ), Potential ( $\phi$ ) and Energy Band Diagram at Equilibrium.



As seen in this figure, there exists a built-in field within the film, whose magnitude depends on the distance within the film. The field is zero at the center of the film and is of different signs at the contacts. The maximum fields are found at the interfaces. The presence of such a field can affect significantly the ferroelectric properties of the film. For example, assuming  $N_a$  (acceptor concentration) =  $10^{18}/\text{cm}^3$ ,  $t$  (film thickness), =  $0.5 \mu\text{m}$ , and  $\epsilon_{\text{PZT}}$  (dielectric constant) = 1000, it is calculated that  $E_0$  (built-in-field) = 45.2 kV/cm. The magnitude of this field is comparable to the  $E_c$  (coercive field) values (~20-60 kV/cm) measured on PZT films prepared in our laboratories.

The coercive fields for similar bulk ceramics is about 1 kV/cm. Hence the higher values of  $E_c$  found in ferroelectric films compared with their bulk counterparts can likely be attributed to the built-in field which needs to be overcome to switch the domains. Since  $E_0$  is linearly dependent on  $N_a$ , a high purity PZT film with a low value of  $N_a$  is expected to yield a low value of  $E_c$ . Note, too, that if the acceptor concentration is not uniform throughout the film (resulting perhaps from variations in Pb content), the uneven field distribution can lead to asymmetric values of  $E_c$ , as are frequently encountered in ferroelectric films.

Such an uneven built-in field gives rise to different regions within the

film with different Curie temperatures, which in turn leads to a transition in the FE properties over a range of temperature, an expectation which is well documented for the dielectric constants of FE thin films as a function of temperature.

Additionally, the presence of such a built-in field can smear out the FE properties of films of relaxor ferroelectrics (e.g., lead magnesium niobate or PMN:  $\text{PbMg}_{1/3}\text{Nb}_{2/3}\text{O}_3$ ) which are much more sensitive to electric fields than are films of normal ferroelectrics such as PZT. The presence of the built-in field leads to a prediction that the dielectric constants of thin films of relaxor FE's should be much lower than those of their bulk counterparts.

Prior to this modeling, the observation of substantially smaller dielectric constants for relaxor thin films (typically  $\epsilon \sim 1000$ ) compared with bulk samples (typically  $\epsilon \sim 10000$ ) had remained a puzzle; and significant research effort had been (mis)directed to processing films of relaxor FE's with properties closer to those of bulk specimens. For  $1\mu\text{m}$  thick relaxor films, control of  $N_{\text{a}}$  down to  $10^{16}/\text{cm}^3$  is necessary to achieve an  $E_{\text{c}}$  of 1 kV/cm. Since  $N_{\text{a}}$  is closely related to Pb vacancies, this calculation illustrates the critical need to control precisely the PbO content in PbO-containing relaxor films. Control to the indicated level is not presently possible.

For FE films thicker than the depletion width, the overall capacitance (and hence dielectric constant) will be dominated by the depletion capacitance unless the films are thick enough that the majority of the voltage drop takes place in the bulk or neutral portion of the film rather than in the depletion zones. As a first approximation, assume that bulk capacitance will dominate when the film thickness is ~10 times the depletion width (typically 0.5-1  $\mu\text{m}$ ) or 5-10  $\mu\text{m}$ . The transition to bulk behavior for FE films is then not expected unless the films are thicker than 5-10  $\mu\text{m}$ . Thus the use of relaxor films for high density DRAM applications is not feasible due to this thickness requirement.

In terms of the model, for an applied voltage,  $V_a$ , the current,  $J$ , is proportional to  $\exp\left[\frac{-qV_a}{4E_0t kT}\right] \left[\sinh \frac{qV_a}{kT}\right]$  where  $q$  = electronic charge,  $E_0$  = threshold voltage,  $t$  = film thickness,  $k$  = Boltzmann's constant and  $T$  = temperature (Fig. A-32). At fields higher than the threshold field,  $E_0$ , the current is limited strictly by Interface I (Fig. A-33), since the barrier to electron flow at Interface II will then be much much larger compared to  $\phi_b$  at Interface I. For constant  $\phi_b$  (assumed independent of applied voltage), the current is then constant with applied voltage, namely  $J \propto \exp(-q\phi_b/kT)$ , where  $\phi_b =$

barrier height at Interface I.

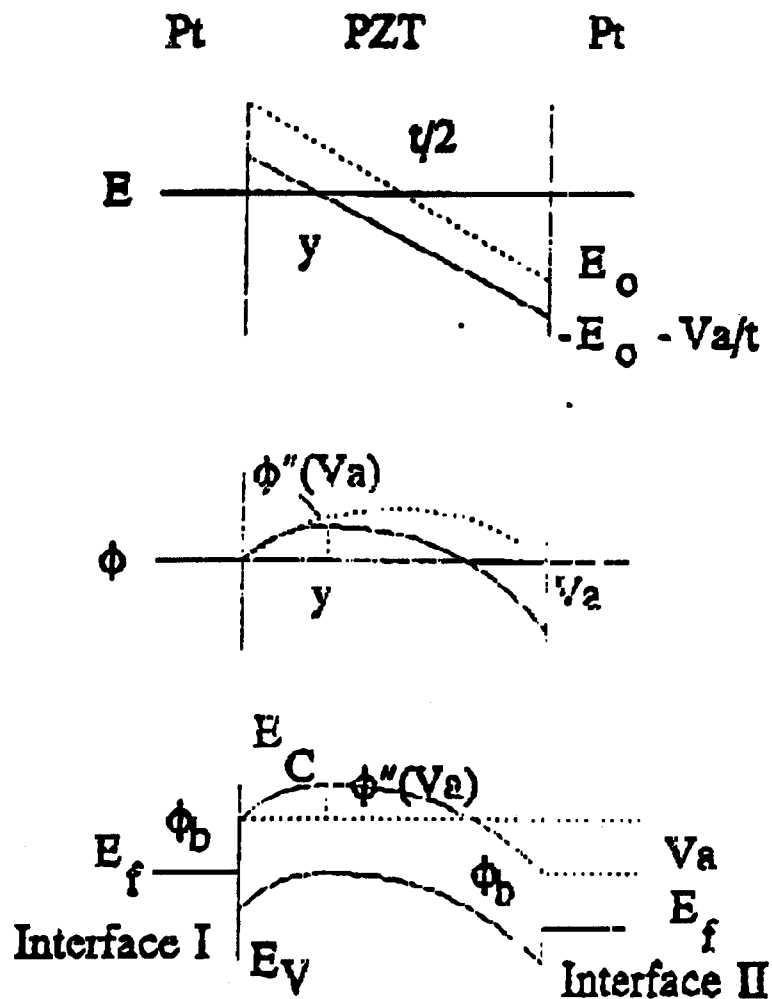


Fig. A-32 Solutions to Poisson's Equation for a wholly depleted PZT Film showing the Electric Field (E), Potential ( $\phi$ ) and Energy Band Diagram at an Applied Bias  $V_a < E_{0t}$ .

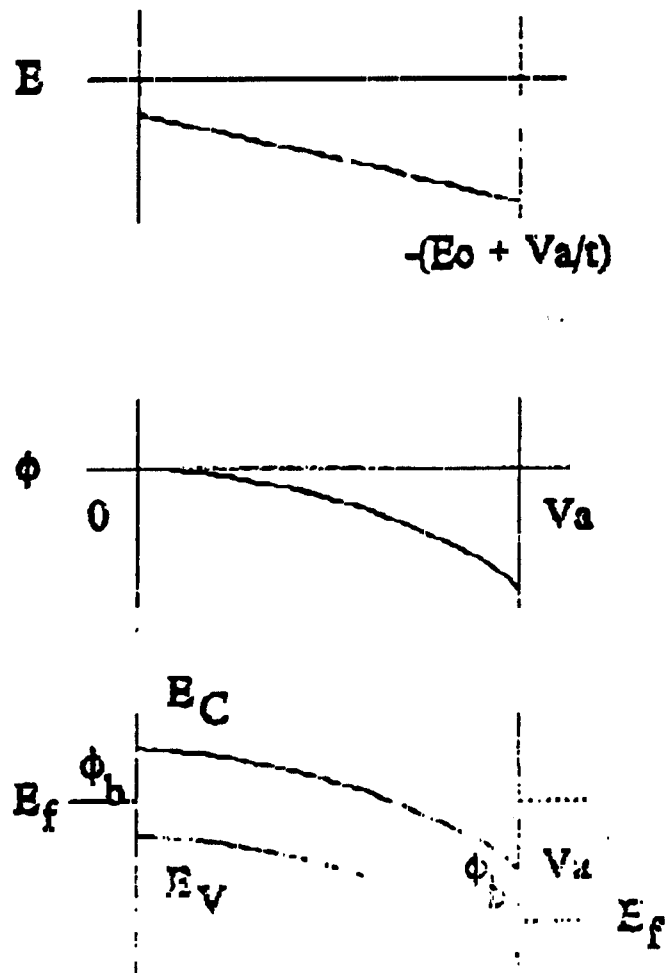


Fig. A-33 The Solutions to the Poisson's Equation for a wholly depleted Film showing the Electric Field ( $E$ ), Potential ( $\phi$ ) and the Energy Band Diagram at an Applied Bias  $V_a > E_0 t$

A general plot of the current-voltage (I-V) behavior according to the proposed model is shown in Fig. A-34a. The predicted behavior is found to agree exceptionally well, both in form and magnitude, with observed I-V characteristics (Fig. A-34b). Also shown in Fig. A-34a are the current-voltage characteristics expected on the basis of conventional models which treat partially depleted Pt-PZT-Pt capacitors. The behavior expected on the basis of previous models based on a partially depleted capacitor is dominated by the reverse bias current of a Schottky barrier and is essentially independent of applied bias, in contrast to the observed behavior in real capacitors.

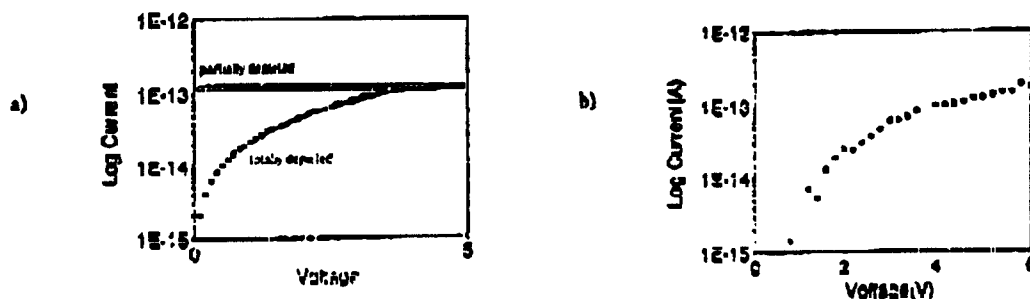


Fig. A-34 I-V Characteristics of a Pt-PZT-Pt Capacitor with Similar Barrier Heights at both Interfaces: a) Predicted for Totally Depleted and Partially Depleted Films; and b) Measured.

By considering the thickness dependence of the current, it is predicted that for thin films, the current and saturation voltage should increase and decrease, respectively, with decreasing thickness. Since the saturation current is determined by the current at Interface I (Fig. A-32), the magnitude of the saturation current is expected to be independent of film thickness, assuming the other parameters are constant, namely  $N_a$  and  $\epsilon_{PZT}$ . On-going work is being performed to validate the independence of the saturation current on film thickness and to determine the effect of temperature on the leakage currents. Complications arise from the dependence of  $\epsilon_{PZT}$  on film thickness and the fact that  $N_a$  may vary in films of different thickness due to varying amounts of PbO diffusion during processing.

Further refinements of the present model based on fully depleted PZT films indicate that the leakage characteristics depend on the barrier heights of the Pt-PZT interfaces; and the symmetry of I-V characteristics in both polarities is determined by the difference of the barrier heights at both interfaces.

Within the context of this model, the observations on post metallization annealing (PMA) made in the present study (see above) can be explained. With higher PMA temperatures, more PbO diffused into the substrate and top

electrodes. These PbO losses lead to the observed inferior dielectric and ferroelectric properties. The observed increase in resistivity and decrease in leakage current with increasing PMA temperature can be correlated with increased PbO diffusion into the substrate and top electrodes, giving rise to higher barrier heights at the interfaces. With higher PMA temperatures, the barrier heights at the two interfaces are higher due to the PbO diffusion; but the difference between the barrier heights at the two interfaces is then smaller due to the smearing effect of the PMA on the PbO profile; and hence the capacitors were more symmetric electrically with much smaller leakage currents.

Finally, the time-dependent effects seen in the dielectric properties of capacitors fired at lower PMA temperatures subjected to a voltage pulse can be attributed to surface states present at the interfaces giving rise to dielectric relaxation after application of the voltage. Such surface states pin further the equilibrium Fermi level, leading to a larger surface potential compared to the bulk (midfilm). This potential pins the domains unless they are pulsed by an external voltage. During voltage pulsing, the surface states undergo relaxation, which in turn modifies the domain relaxation and dielectric behavior. In capacitors fired to higher temperatures, the density of these surface states is



lower due to diffusion at the interfaces. Hence the relaxation effect of the surface states on the domain structure of the films during voltage pulsing is weaker, and the dielectric behaviors of the devices are essentially time-independent. The density of the surface states and their location in the electronic structure of the films, as well as their dependence on microstructure and processing, require further elucidation.

In brief, a new model of the electrical behavior of Pt-PZT-Pt capacitors has been developed, based on the concept that the ferroelectric films are fully depleted throughout their thickness. Calculations based on this model have been remarkably successful in predicting observed electrical behavior, quantitatively as well as qualitatively. In light of this success, and the potential of the model for addressing other phenomena, its extension to new areas seems highly desirable.

## B. Organic-Inorganic Hybrid Materials (POLYCERAMS)

POLYCERAMS, also known as ORMOSILS or CERAMERS, are polymer-modified ceramic materials in which the organic and inorganic components are combined on a molecular or near-molecular level. Fig. B-1 shows a schematic view of a POLYCERAM in which the organic components are chemically bonded into the inorganic network.

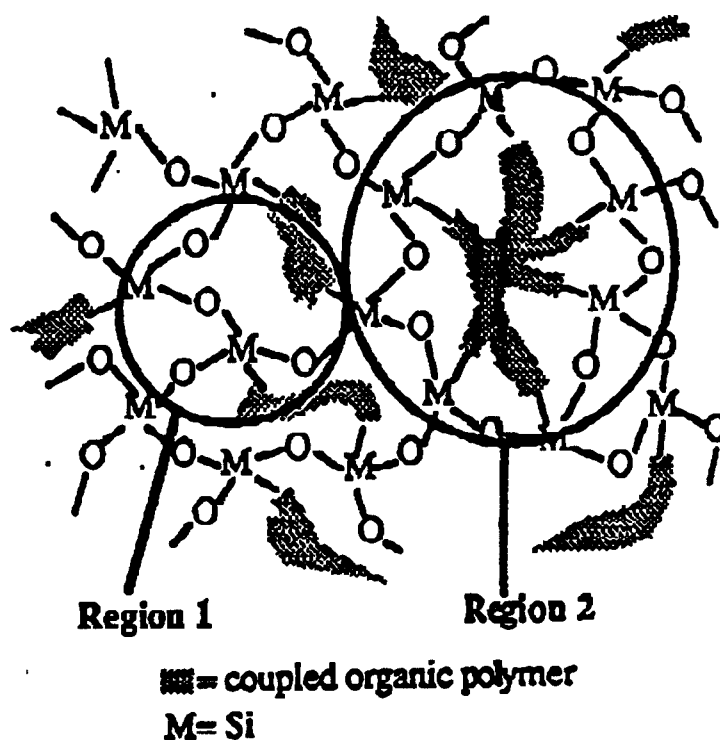


Fig. B-1 A schematic structure of a POLYCERAM.

The properties of these materials can be varied over a wide range by varying the volume fractions of the constituents as well as their chemistries,

those of POLYCERAMS containing 80 vol. % MPEOU due to the presence of more  $\text{TiO}_2$  per volume in the former. Note that refractive indices as high as 1.685 were obtained in the POLYCERAMS containing 60 vol. % polymer.

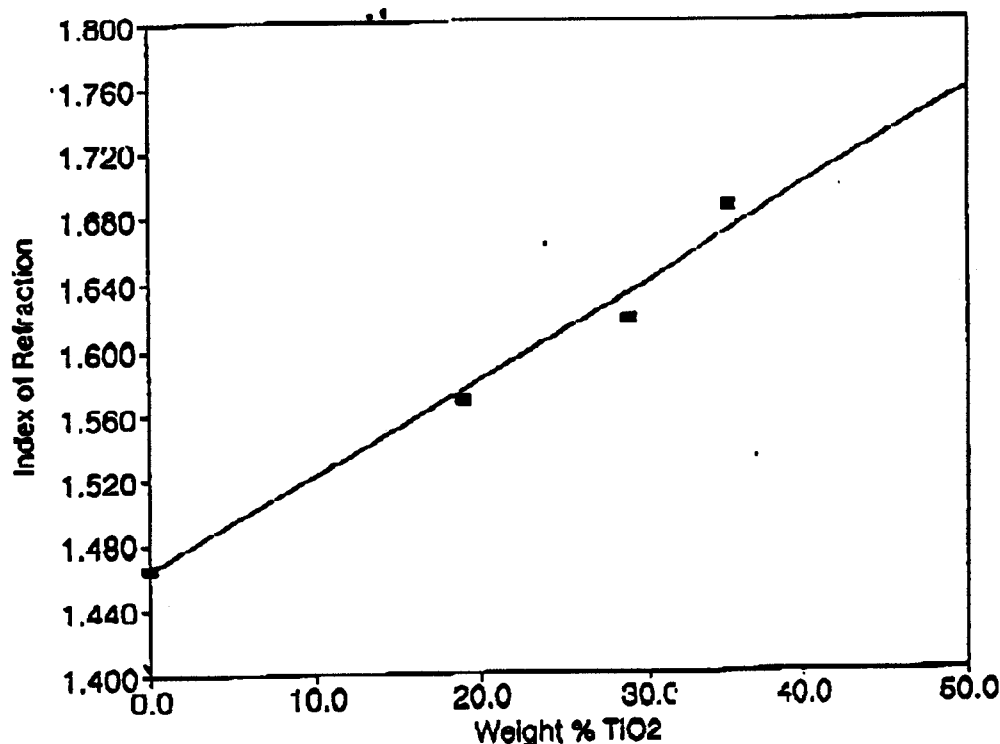


Fig. B-5 Linear increase of the index of refraction with  $\text{TiO}_2$  content of  $\text{SiO}_2$ - $\text{TiO}_2$ -MPEOU POLYCERAMS incorporating 60% volume MPEOU.

POLYCERAMS with a  $\text{SiO}_2/\text{TiO}_2$  molar ratio of 1:2 in 60 vol. % polymer tended to crack. In addition, films containing 40 and 20 vol. %

polymer cracked at all  $\text{SiO}_2/\text{TiO}_2$  mole ratios. These results suggest that a  $\text{SiO}_2/\text{TiO}_2$  molar ratio of 1:2 in POLYCERAMS containing 60 vol. % polymer is the limit of  $\text{TiO}_2$  content for forming crack-free films in this system. Cracking at high  $\text{TiO}_2$  concentrations reflects rapid condensation of the inorganic network, producing rigid structures which are unable to relax sufficiently and to accomodate drying stresses. Hence POLYCERAMS containing 80 vol. % polymer were chosen for further tailoring of chemistry and processing and detailed characterization of the optical attenuation.

Attenuation in the POLYCERAM films was measured using a prism coupling technique. A prism was positioned tightly on the film in order to couple laser light into a waveguide mode and to obtain a streak in the waveguide. A coherent fiber bundle was then used as an imaging system to transfer the scattered streak intensity distribution to a photomultiplier tube (PMT)/precision slit assembly. The PMT/slit combination was driven by a stepper-motor, and was automatically scanned across 1 cm of the imaged streak. The dc signal was converted to a voltage and sent to a digitizing oscilloscope where it was continuously time-averaged to reduce electrical and optical noise. The resulting voltages were converted to a logarithmic scale and least-squares curve-fitted to yield loss in dB/cm. The measurements were made

using a Helium-Neon laser ( $\lambda = 632.8$  nm).

For many applications, the optical loss of a waveguide should be less than 1 dB/cm. Optical attenuation in waveguides can result from scattering of the guided mode due to surface roughness or variations in refractive index through the volume (density fluctuations/inhomogeneities or defects such as grain boundaries, pits, cracks, dust, etc.). Table B-1 reports the losses of MPEOU-SiO<sub>2</sub>-TiO<sub>2</sub> POLYCERAM waveguides comprising 80 vol. % MPEOU. Loss measurements were conducted for the TE<sub>0</sub> mode. Electromagnetic waves propagating in a plane are called TE waves (mode) if the E vector is perpendicular to the plane and TM waves (mode) if the B vector is perpendicular to the plane. The mode number is added to this notation. Fig. B-6 shows the different mode structures in an infinitely long film. TE<sub>0</sub> is the lowest order transverse electric mode in a waveguide and thus is the most confined within the film.

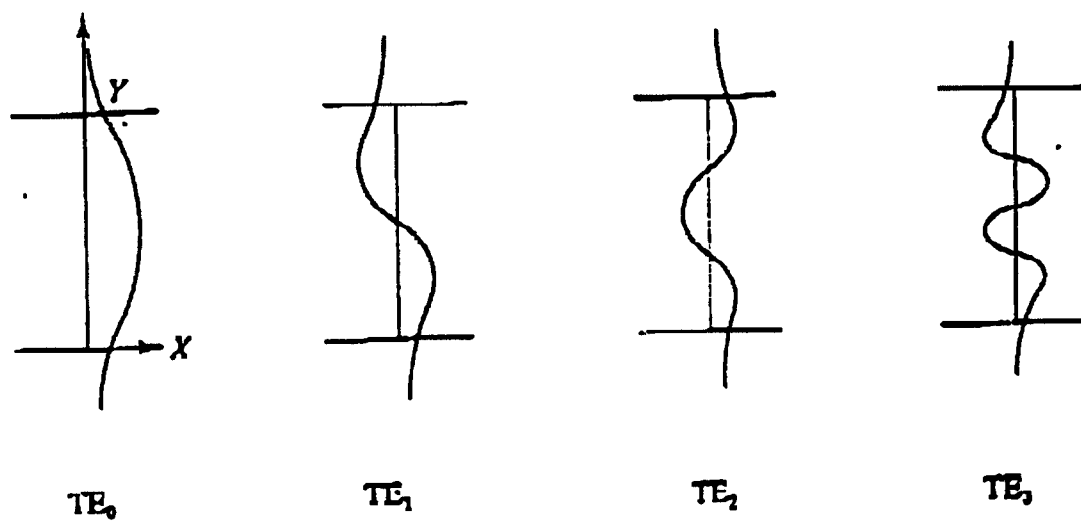


Fig. B-6 Mode structure in the Y direction for an infinitely long film (in the X direction).

**Table B-1: Refractive Index, Thickness and Loss of Partially Hydrolyzed (2 moles H<sub>2</sub>O) MPEOU-SiO<sub>2</sub>-TiO<sub>2</sub> POLYCERAMS (80 vol. % MPEOU) as a Function of Composition.**

<b>Molar Ratio of SiO<sub>2</sub>:TiO<sub>2</sub></b>	<b>Refractive Index</b>	<b>Thickness (microns)</b>	<b>Loss ± st. dev. (dB/cm)</b>
<b>1:0</b>	<b>1.495</b>	<b>3.23</b>	<b>0.69 ± 0.10</b>
<b>1:0.5</b>	<b>1.543</b>	<b>2.62</b>	<b>1.68 ± 0.21</b>
<b>1:1</b>	<b>1.571</b>	<b>2.89</b>	<b>1.39 ± 0.15</b>
<b>1:1.5</b>	<b>1.601</b>	<b>2.86</b>	<b>0.53 ± 0.12</b>
<b>1:2</b>	<b>1.634</b>	<b>2.94</b>	<b>1.49 ± 0.19</b>

It is seen that for all compositions the losses are near or below 1.5 dB/cm, with no apparent trends with composition. These films were multi-mode; and hence a portion of the losses may be due to inter-modal scattering where energy is lost in propagating other modes as well as the lowest order mode. It is expected that the losses will be even lower for single-mode waveguides.

The degree of hydrolysis directly affects the extend of reaction. The effects of the degree of hydrolysis on the properties of POLYCERAM films were explored by preparing solutions with  $H_2O$  contents varying from 2 to 8 moles of  $H_2O$  per mole of TEOS, following the processing sequence shown in Fig. B-7. It was observed that increasing  $H_2O$  content resulted in greater non-uniformity and increased surface roughness. Ellipsometry measurements could not be conducted on films hydrolyzed with  $H_2O$  contents greater than 4 moles due to scattering and absorption of the laser beam.





**Table B-2: Refractive Index, Thickness and Optical Attenuation of Partially Hydrolyzed vs Fully Hydrolyzed POLYCERAM Films. Vol. % MPEOU = 80; SiO<sub>2</sub>/TiO<sub>2</sub> (molar) = 1/1.**

Hydrolysis	Refractive Index	Thickness (microns)	Attenuation at 632.8nm ± st. dev. (dB/cm)
SiO <sub>2</sub> -TiO <sub>2</sub> -MPEOU partial hydrolysis (2 moles H <sub>2</sub> O)	1.571	2.89	1.39 ± 0.15
SiO <sub>2</sub> -TiO <sub>2</sub> -MPEOU full hydrolysis (4 moles H <sub>2</sub> O)	1.569	2.53	2.16 ± 0.20

Consistent with these findings, the modal streak fanned rapidly in the plane of the waveguide, indicating in-plane scatter attributable to volume density fluctuations in the films.

It can therefore be concluded that additional water beyond some modest amount increases the level of inhomogeneity in POLYCERAM films. Additional water apparently causes rapid hydrolysis/condensation of the Ti species resulting in localized inhomogeneity, and may also increase the polarity of the solvent, thus changing the solubility of the reacting species, particularly that of the polymer. A patent disclosure based on this finding is presently being prepared.

The homogeneity of the POLYCERAMS was investigated with Small

Angle X-ray Scattering (SAXS). Fig. B-8 shows the SAXS profiles (in the form of Guinier plots) for  $\text{SiO}_2/\text{MPEOU}$  samples compared with those of partially hydrolyzed (2 moles  $\text{H}_2\text{O}$  per mole of TEOS) and fully hydrolyzed (4 moles  $\text{H}_2\text{O}$ ) MPEOU- $\text{SiO}_2$ - $\text{TiO}_2$  POLYCERAMS. The sample films had a  $\text{SiO}_2:\text{TiO}_2$  molar ratio of 1:1. The scattering from the POLYCERAMS indicates materials having a high degree of chemical and physical homogeneity.

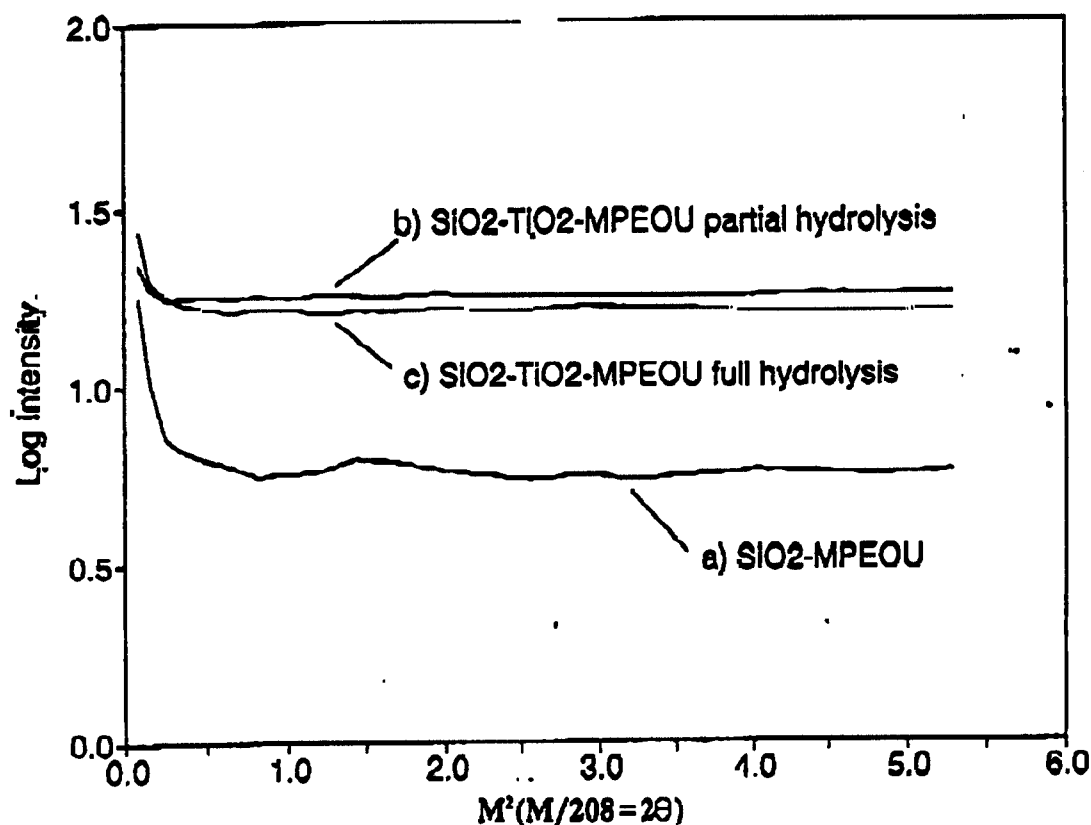


Fig. B-8 SAXS profiles of a) hydrolyzed polymer, b) partially hydrolyzed (2 moles  $\text{H}_2\text{O}$ )  $\text{SiO}_2\text{-TiO}_2\text{-MPEOU}$  POLYCERAM ( $\text{SiO}_2\text{:TiO}_2$  molar ratio of 1:1) and c) fully hydrolyzed (4 moles  $\text{H}_2\text{O}$ )  $\text{SiO}_2\text{-TiO}_2\text{-MPEOU}$  POLYCERAM ( $\text{SiO}_2\text{:TiO}_2$  molar ratio of 1:1). The POLYCERAMS show a higher degree of scattering than the hydrolyzed polymer.

It is observed, however, that the SAXS intensities from  $\text{MPEOU-SiO}_2\text{-TiO}_2$  POLYCERAMS are higher than those from  $\text{MPEOU-SiO}_2$  POLYCERAMS. This indicates that the incorporation of  $\text{TiO}_2$  increases the fluctuations in electron density within the network.

It is also observed that the SAXS intensities from partially hydrolyzed POLYCERAMS (2 moles  $H_2O$ ) are slightly higher than those from fully hydrolyzed POLYCERAMS (4 moles  $H_2O$ ). This observation stands in contrast to the data on optical attenuation, which indicate lower losses for films prepared under conditions of partial hydrolysis than for those prepared using full hydrolysis. The origin of this apparent discrepancy is presently being explored using electron microscopy coupled with more extensive SAXS data.

Atomic Force Microscopy (AFM) was used to study the submicron scale surface morphology of partially hydrolyzed (2 moles  $H_2O$  per mole of TEOS) and fully hydrolyzed (4 moles  $H_2O$ ) MPEOU- $SiO_2$ - $TiO_2$  films. On a scan area of  $1 \times 1 \mu m^2$ , the addition of water from 2 moles to 4 moles has found to increase the average roughness from 1.148 Å to 11 Å, and the root mean square roughness from 1.436 Å to 13.91 Å. The additional water produces a more cross-linked structure, as exhibited by the high viscosity observed in the high- $H_2O$  solutions. Viscous solutions yield films with poor relaxation characteristics after spin-coating, resulting in increased surface roughness of the films.

It thus appears that increased water in the solution, at least over the indicated range, increases both the volume inhomogeneities and surface

roughness of films produced therefrom. Both of these changes should lead to increased optical attenuation in the films.

One of the advantages of wet chemical synthetic methods is the capability which they provide for tailoring the structures of materials - e.g., by modifying the functionality of the reactive groups through the use of chelating agents. During the present year, attention was directed to the effect of TIP chelated with 2,4 pentanedione on fully hydrolyzed (4 moles  $H_2O$ ) POLYCERAMS having a  $SiO_2:TiO_2$  molar ratio of 1:1 and a volume fraction MPEOU of 80%. AFM showed that the addition of 2,4 pentanedione aids in obtaining POLYCERAM films with notably smoother surface contours. Smooth surfaces are desired for reduced surface scattering in planar waveguides. Fig. B-9 shows AFM micrographs of fully hydrolyzed MPEOU- $SiO_2-TiO_2$  POLYCERAMS with and without 2,4 pentanedione. It is seen that the addition of 2,4 pentanedione decreases the average roughness from 11 Å to 3 Å and the root mean square roughness from 13.91 Å to 4.01 Å. The chelating agent decreases the degree of cross-linking of the network, allowing easier relaxation and thus resulting in smoother films. Consistent with this view, the chelated solutions exhibited longer gelation times than similar solutions without the chelating agent.

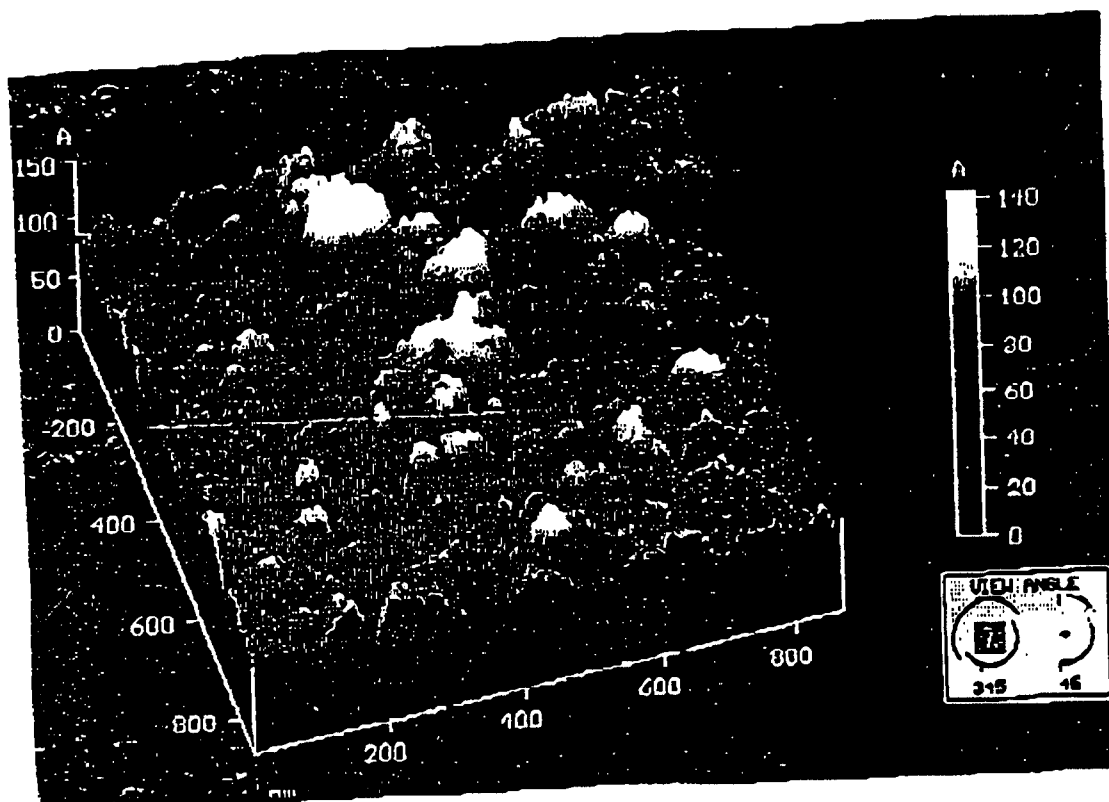


**Fig. B-9** AFM micrographs of fully hydrolyzed (4 moles  $\text{H}_2\text{O}$ )  $\text{SiO}_2\text{-TiO}_2\text{-MPEOU POLYCERAM}$  without a) and with b) chelating agent 2,4 pentanedione at 80 % by volume MPEOU and a  $\text{SiO}_2/\text{TiO}_2$  mole ratio of 1/1. The surface roughness decreases with chelate.

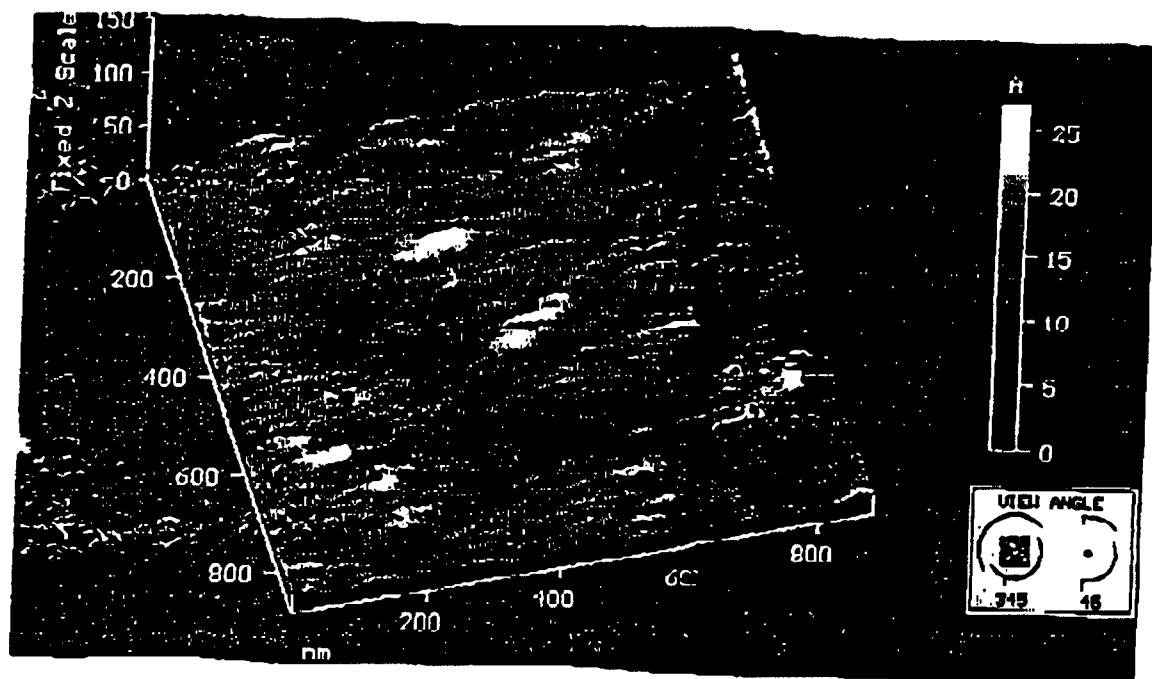


Fig. B-9b



It was found that although 2,4 pentanedione decreased the surface roughness of fully hydrolyzed films, the surface roughness of partially hydrolyzed films was still the lowest (Table B-3). With this in mind, it was decided to explore the effect of chelate on the surface roughness of partially hydrolyzed POLYCERAMS. Since it was observed that the addition of 2,4 pentanedione yields orange-colored materials due to absorption by residual Ti-acac complex, and since it is important for waveguides to have minimal absorption, experiments were conducted with acetic acid, a chelating agent which did not contribute significant absorption.

**Table B-3: Surface Roughness of MPEOU-SiO<sub>2</sub>-TiO<sub>2</sub> POLYCERAMS Films Containing 80 vol. % MPEOU and synthesized with different amounts of H<sub>2</sub>O and with different chelating agents.**

<b>SiO<sub>2</sub>-TiO<sub>2</sub>-MPEOU</b>	<b>Average Roughness (RA)</b>	<b>Root Mean Square (RMS) Roughness</b>
partial hydrolysis (2 moles H <sub>2</sub> O) no chelation	1.148 Å	1.436 Å
full hydrolysis (4 moles H <sub>2</sub> O) no chelation	11.0 Å	13.91 Å
full hydrolysis (4 moles H <sub>2</sub> O) 2,4 pentanedione chelation	3.0 Å	4.006 Å
partial hydrolysis (2 moles H <sub>2</sub> O) acetic acid chelation	0.975 Å	1.222 Å

Acetic acid in a  $\text{TiO}_2\text{:AcAc}$  molar ratio of 1:1 was added to a partially hydrolyzed (2 moles  $\text{H}_2\text{O}$ ) solution of  $\text{MPEOU-SiO}_2\text{-TiO}_2$  with a  $\text{SiO}_2\text{:TiO}_2$  mole ratio of 1:1 and a vol. % polymer of 80 %. AFM studies revealed a small decrease in the surface roughness. Acetic acid decreased the average roughness from 1.148 Å to 0.975 Å and the root mean square roughness from 1.436 Å to 1.222 Å on a scan of  $1 \times 1 \mu\text{m}^2$ . Such levels of surface roughness are sufficiently small that waveguide losses from surface scattering should be unimportant.

Optical loss measurements were performed on the chelated POLYCERAM films described above (see Table B-4). As expected, the attenuation of a partially hydrolyzed (2 moles  $\text{H}_2\text{O}$ )  $\text{MPEOU-SiO}_2\text{-TiO}_2$  film with a  $\text{SiO}_2\text{:TiO}_2$  mole ratio of 1:1 chelated with 2,4 pentanedione was much higher than the loss of the same film chelated with acetic acid. The higher loss is due absorption associated with the Ti-acac complex (orange color). The acetic acid film, on the other hand, exhibited low scatter, low absorption and low optical attenuation.

**Table B-4: Refractive index, thickness, and optical loss at 632.8 nm of partially hydrolyzed (2 moles H<sub>2</sub>O) POLYCERAMS MPEOU-SiO<sub>2</sub>-TiO<sub>2</sub> chelated with 2,4 pentanedione and acetic acid. The compositions have a SiO<sub>2</sub>:TiO<sub>2</sub> mole ratio of 1:1 and a vol. % polymer of 80.**

Chelate	Refractive Index	Thickness (microns)	Loss $\pm$ st. dev. (dB/cm)
2,4 pentanedione	1.569	3.0	11.95 $\pm$ 0.29
Acetic Acid	1.568	3.2	0.48 $\pm$ 0.13

The effects of cross-linking were further explored in a study of solution aging, i.e., the time span between synthesizing the solutions and spin-coating. Although the index of refraction did not show a notable variation, the optical loss increased significantly with aging time, from 1.39  $\pm$  0.15 dB/cm on immediately coating after synthesis to 4.00  $\pm$  0.413 dB/cm after 51 hours of aging (see Fig. B-10). With increased aging time, more cross-linking leads to increased size of the oligomers in the solution and greater width in the size distribution of the oligomers which in turn leads to greater index inhomogeneities in the films, and thus to increased optical loss.

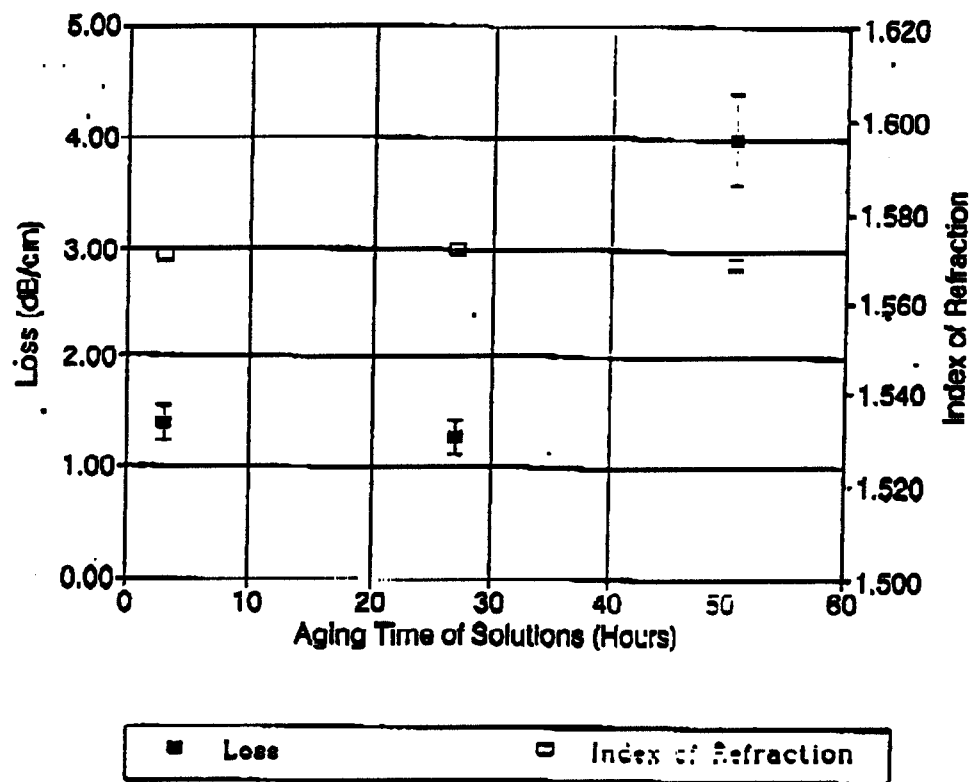


Fig. B-10 A study of the effect of aging of solution on the index of refraction and loss of POLYCERAMS with a  $\text{SiO}_2\text{:TiO}_2$  mole ratio of 1:1. The loss increases with aging time.

UV-Vis transmission spectroscopy was used to obtain the absorption edge of the POLYCERAM films (see Table B-5). The absorption edge is seen to increase with increasing  $\text{TiO}_2$  content. The absorption edge of  $\text{SiO}_2$  (1600 Å) is lower in wavelength than that of  $\text{TiO}_2$  (3500 Å); as the amount of  $\text{TiO}_2$  increases, POLYCERAM films with the same polymer content incorporate more of the  $\text{TiO}_2$  characteristics, thus resulting in an absorption edge located at longer wavelengths. The change in absorption edge with increasing  $\text{TiO}_2$  content is consistent with homogeneous incorporation of the constituents in the POLYCERAM films. This homogeneity is supported by the SAXS data mentioned above.

**Table B-5: Absorption edges of POLYCERAM films vs.  $\text{SiO}_2\text{:TiO}_2$  ratio**

<b>Polyceram Composition <math>\text{SiO}_2\text{:TiO}_2</math></b>	<b>Absorption Edge (<math>\text{\AA}</math>)</b>
<b>1:0.5</b>	<b>2900</b>
<b>1:1</b>	<b>2950</b>
<b>1:1.5</b>	<b>3000</b>
<b>1:2</b>	<b>3050</b>

In sol-gel chemistry, the processing procedure and sequence of steps is often important in tailoring the properties of the resulting materials. Hence, the order of mixing of the components and the refluxing time of the solutions were explored in terms of their effects on the index of refraction and optical loss. Table B-6 reports the optical properties of POLYCERAMS synthesized using four different processing sequences. In all cases, the  $\text{H}_2\text{O}$  was added at the beginning of the reaction. The variation in refractive index remained within experimental error; and all measured losses were below 1 dB/cm. Streaks in films produced following the processing sequences C and D, however, were more uniform and had noticeably fewer hot spots. In processing sequences C and D, MPEOU and TEOS were refluxed together, while in sequences A and

B, MPEOU and TEOS were added at different times. The joint refluxing of MPEOU and TEOS apparently leads to more uniform hydrolysis/condensation reactions. When one component at a time is added during refluxing, reactants may undergo self-condensation, in addition to co-condensation, thus causing decreased homogeneity of the network.



Table B-6: The effect of processing sequence on the index of refraction, thickness and loss of partially hydrolyzed (2 moles  $\text{H}_2\text{O}$ ) POLYCERAMS. All compositions have a  $\text{SiO}_2\text{:TiO}_2$  mole ratio of 1:1 and a vol. % polymer of 80.

Processing Sequence (reflux time)	Refractive Index	Thickness (microns)	Loss $\pm$ st. dev. (dB/cm)
A) MPEOU (15 min) --> TEOS (15 min) --> TIP (1 hr)	1.570	2.90	$0.52 \pm 0.15$
B) TEOS (15 min) --> MPEOU (15 min) --> TIP (1 hr)	1.578	2.85	$0.51 \pm 0.23$
C) MPEOU + TEOS (30 min) --> TIP (1 hr)	1.571	2.89	$< 0.25$
D) MPEOU + TEOS (15 min) --> TIP (1 hr)	1.573	2.95	$0.85 \pm 0.04$

To evaluate whether the optical attenuation is principally associated with the bulk or the surface of the film, loss measurements were conducted on different TE modes. The film chosen was a partially hydrolyzed (2 moles  $\text{H}_2\text{O}$ ) POLYCERAM with a  $\text{SiO}_2\text{:TiO}_2$  mole ratio of 1:1 and a vol. % polymer of 80. This film supported 5 modes ( $\text{TE}_0\text{-TE}_4$ ). Measurements were conducted on the  $\text{TE}_0$ ,  $\text{TE}_2$  and  $\text{TE}_4$  modes. Fig. B-11 shows that the optical loss decreases with increasing mode number: The loss decreased from  $1.39 \pm 0.15$  dB/cm for  $\text{TE}_0$  to  $<0.25$  dB/cm for  $\text{TE}_4$ .

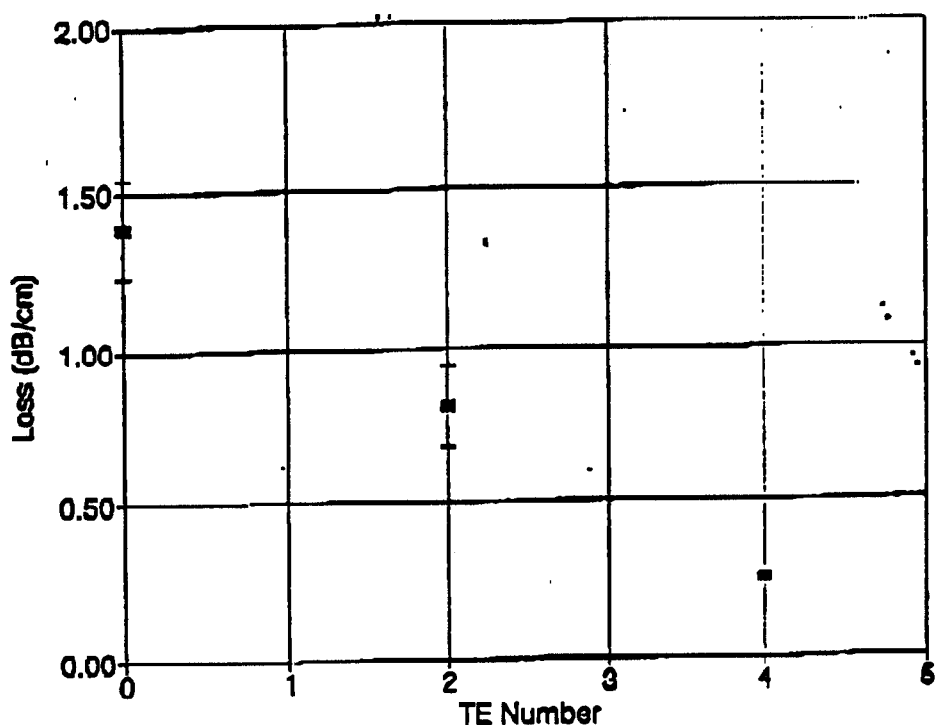


Fig. B-11 Optical loss values of  $TE_0$ ,  $TE_2$  and  $TE_4$  modes of a POLYCERAM with a  $SiO_2$ - $TiO_2$  mole ratio of 1:1. Loss decreases with increasing mode number.

To understand why the loss decreases with mode number, the electric field profiles of the film were calculated. Fig. B-12 shows the transverse electric field profiles of the  $TE_0$ ,  $TE_2$  and  $TE_4$  modes. As the mode number increases, the electric field amplitudes at the two waveguide interfaces increases, and the portion of the mode energy propagating outside the guiding region also increases. Thus, the higher modes tend to probe the surface regions of the guide to a greater extent than the lower order modes, which have low field

amplitudes at the interfaces, and generally have nearly all of their modal energy confined within the guiding film layer. Hence, since the attenuation decreases with increasing mode number, this implies that volume inhomogeneities or absorption within the coating are the dominant loss scattering mechanisms in these films.

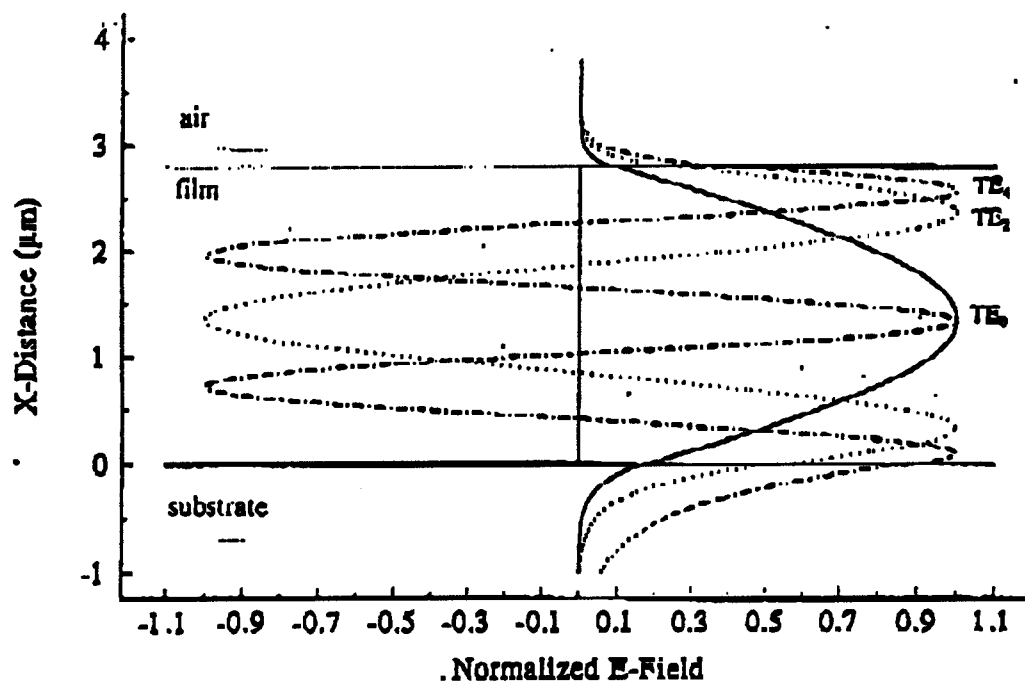


Fig. B-12 Electric field profiles of  $TE_0$ ,  $TE_2$  and  $TE_4$  of a POLYCERAM with a  $SiO_2$ - $TiO_2$  mole ratio of 1:1. As the mode number increases, the profiles are less confined within the film.

Based on the SAXS data, which indicate a high level of homogeneity, it is somewhat surprising that the attenuation data indicate that most of the scattering results from bulk inhomogeneities. It is premature to conclude whether the loss is due principally to density fluctuations in the POLYCERAM network or to particles within the film. An index inhomogeneity of 0.001-0.003 is sufficient to cause the measured attenuation. The films used in the SAXS and loss studies were processed differently: The bulk films used for SAXS characterization were cast in a petri-dish and allowed to dry in air for one to two weeks, while the thinner films used for the loss study were spin-coated through a 0.1  $\mu\text{m}$  syringe filter and dried in vacuum at 125C for three days. Since a longer gelation period usually corresponds to a higher level of homogeneity, it is expected that the bulk (SAXS) films would be more homogeneous than the thin films. More experimentation is needed, however, to determine the principal source of optical attenuation in these films. For example, smaller pore size filters may eliminate more of the dust particles and thus decrease the loss. Such investigations are presently underway.

In addition to the ability to tailor the refractive index of POLYCERAM materials, we have also observed that the hardness and thermal stability can be significantly enhanced compared to those of the neat polymer. Table B-7

reports the Knoop hardness of POLYCERAM films as a function of increasing  $\text{TiO}_2$  content. The analyzed films were  $5\text{ }\mu\text{m}$  thick; and the indicated values represent the average of hardness measurements down to a depth of  $2\text{ }\mu\text{m}$  (hardness measurements deeper than  $2\text{ }\mu\text{m}$  include the effect of the quartz substrate). The hardness is seen to increase by nearly a factor of 1.7 between the polymer film (45.4 Knoop) and the POLYCERAM film with a 1:2  $\text{SiO}_2/\text{TiO}_2$  molar ratio and a vol. % polymer of 80 (76.1 Knoop). The incorporation of  $\text{SiO}_2$  - and even more so the incorporation of  $\text{TiO}_2$  - in the structure serves to decrease the compressibility of the network, thus enhancing the relative hardness.

**Table B-7: Knoop Hardness of POLYCERAM Films**

Composition	Knoop Hardness
100% polymer	45.4
polyceram $\text{SiO}_2\text{:TiO}_2 = 1:0.5$	65.2
polyceram $\text{SiO}_2\text{:TiO}_2 = 1:1$	65.6
polyceram $\text{SiO}_2\text{:TiO}_2 = 1:1.5$	67.8
polyceram $\text{SiO}_2\text{:TiO}_2 = 1:2$	76.1

TGA indicates that the present POLYCERAMS also have a higher thermal stability than their organic constituents. Table B-8 shows that the temperature of onset of decomposition of the MPEOU polymer is about 150C; that of the hydrolyzed polymer is about 185C; and that of an MPEOU- $\text{SiO}_2$ - $\text{TiO}_2$  POLYCERAM (vol. % polymer = 80;  $\text{SiO}_2\text{:TiO}_2$  mole ratio of 1:1) is about 250C. The marked increase in thermal stability indicated by these data expand the range of utility of the POLYCERAMS. Its origin is presently being investigated.

**Table B-8: Decomposition Temperatures of MPEOU, Hydrolyzed MPEOU and MPEOU-SiO<sub>2</sub>-TiO<sub>2</sub> films containing 80 vol. % polymer of SiO<sub>2</sub>/TiO<sub>2</sub> (molar) = 1/1.**

Composition	Temperature of Decomposition (C)
MPEOU	150
Hydrolyzed MPEOU	185
SiO <sub>2</sub> :TiO <sub>2</sub> :MPEOU	250

For most waveguide applications in integrated optics, a low dispersion (index of refraction vs. wavelength) is desired. Measurements of dispersion as a function of composition were therefore carried out using  $\lambda = 632.8, 514.5, 488$  and  $457.9$  nm. The results indicate that the refractive index and dispersion both increase with increasing TiO<sub>2</sub> content. Fig. B-13 shows the refractive index of refraction of partially hydrolyzed (2 moles H<sub>2</sub>O) MPEOU-SiO<sub>2</sub>-TiO<sub>2</sub> POLYCERAMS as a function of composition; and Fig. B-14 shows the change in refractive index ( $\Delta n$ ) vs. TiO<sub>2</sub> content, where  $\Delta n$  is the difference in refractive index between  $\lambda = 632.8$  nm and  $\lambda = 457.9$  nm.

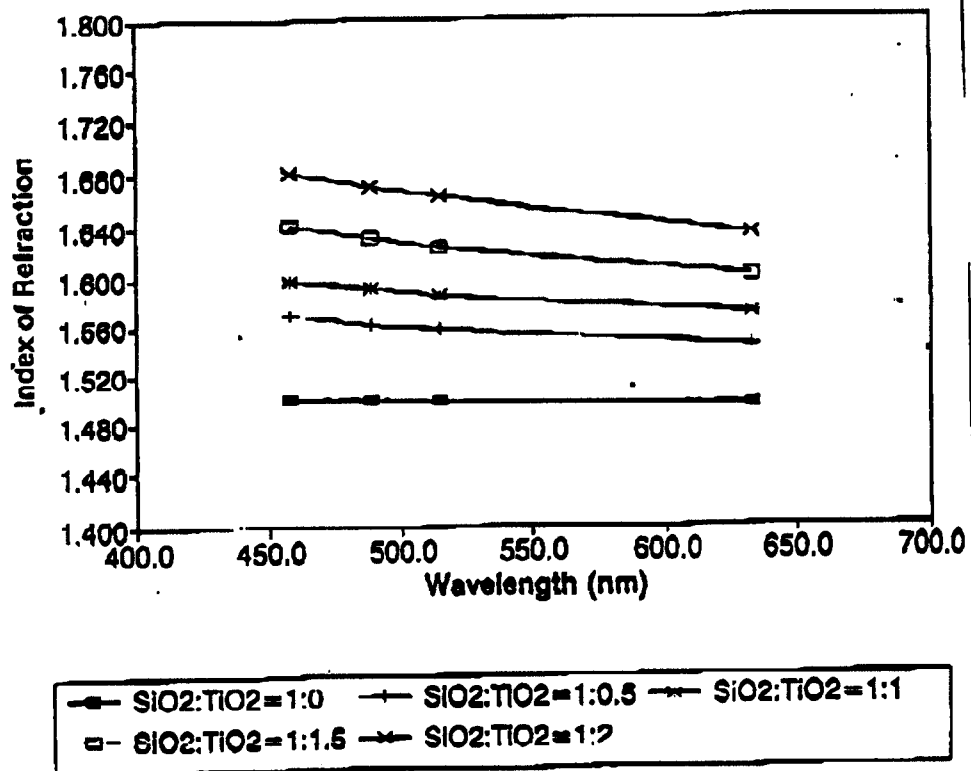


Fig. B-12 Index of refraction of POLYCERAMS with composition at wavelengths 632.8, 514.5, 488 and 457.9 nm.



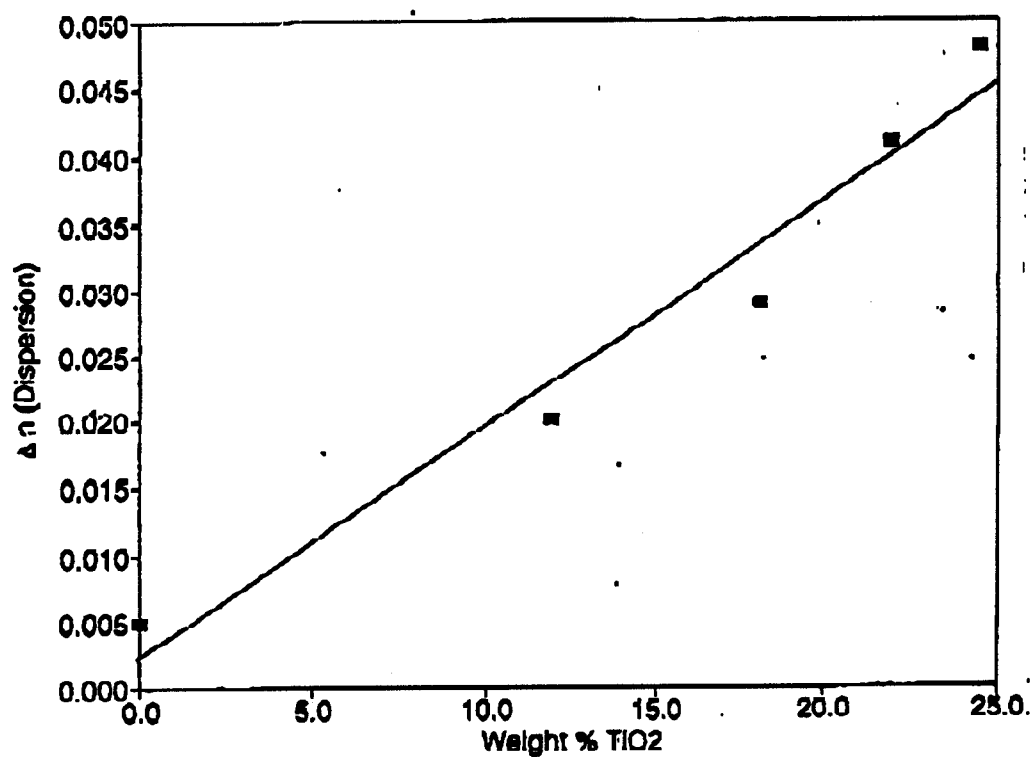


Fig. B-14 Dispersion ( $\Delta n$ ) of POLYCERAMS with weight %  $\text{TiO}_2$ . Dispersion increases with  $\text{TiO}_2$  content.

These dispersion values can be fit using a Sellmeier oscillator relation to find the Abbe number ( $v_d$ ) of each composition. Abbe numbers and the  $n_d$  vs  $v_d$  relationship for glasses are well established while that of organic/inorganic hybrids are substantially unknown save for the work of Schmidt and his co-workers. The Sellmeier dispersion relation can be expressed:

$$\{ [n_F(\lambda)]^2 - 1 \}^{-1} = A/\lambda^2 + B$$

where the constants A and B were determined in a least-squares fit from the indices  $n_F(\lambda)$  measured at the four wavelengths given above. The results of the above fits were employed to find the Abbe number ( $v_d$ ) of each composition where

$$v_d = (n_d - 1)/(n_F - n_C)$$

and  $n_d$ ,  $n_F$  and  $n_C$  are the indices of refraction for the helium d line (587.6 nm), the hydrogen F line (486.1 nm) and the hydrogen C line (656.3 nm), respectively. Table B-9 reports the Abbe numbers of the POLYCERAMS as a function of composition. A high Abbe number corresponds to a low dispersion. It is seen that the POLYCERAM with no  $\text{TiO}_2$  has the highest Abbe number (lowest dispersion), while the POLYCERAM with the highest  $\text{TiO}_2$  content has the lowest Abbe number (highest dispersion). A higher  $\text{TiO}_2$

content increases the index of refraction and dispersion, and decreases the Abbe number. The dispersion values obtained here promise a high degree of flexibility in tailoring the  $n_d$  vs  $v_d$  relationship: The dispersion and refractive index values of POLYCERAMS fall on both sides of the  $n_d$  vs.  $v_d$  relation for optical glasses. To obtain a POLYCERAM with a desired Abbe number, it is sufficient to change the density of the structure by incorporating the correct amount of selected inorganics. Simply stated, the refractive index and the Abbe number of POLYCERAMS can easily be customized, and include a range of novel combinations of  $n$ - $v$  values.

**Table B-9: Abbe numbers of MPEOU-SiO<sub>2</sub>-TiO<sub>2</sub> POLYCERAMS containing 80 vol. % MPEOU and various SiO<sub>2</sub>/TiO<sub>2</sub> molar ratios.**

<b>Molar Ratio of SiO<sub>2</sub>:TiO<sub>2</sub></b>	<b>Weight % TiO<sub>2</sub></b>	<b>v<sub>d</sub> (Abbe number)</b>
<b>1:0</b>	<b>0</b>	<b>112.73</b>
<b>1:0.5</b>	<b>11.9</b>	<b>25.35</b>
<b>1:1</b>	<b>18.1</b>	<b>23.85</b>
<b>1:1.5</b>	<b>21.9</b>	<b>17.52</b>
<b>1:2</b>	<b>24.5</b>	<b>16.16</b>

The successful fabrication of MPEOU-based waveguides with exceptionally low optical losses has led us to synthesize a wide range of POLYCERAM materials, composed of a variety of organic and inorganic components. Of particular interest were POLYCERAMS comprising of  $\text{GeO}_2$ ,  $\text{ZrO}_2$ ,  $\text{Ta}_2\text{O}_5$ ,  $\text{BaO}$  and  $\text{ZnO}$  with  $\text{SiO}_2$  as the inorganic components and PDMS (polydimethylsiloxane) as the organic component. SAXS studies were carried out on all of these POLYCERAMS and indicate a high level of homogeneity. Determinations of refractive index and optical attenuation in planar waveguides prepared from these POLYCERAMS yielded the results shown in Table B-10. Since the synthesis and processing of these materials were by no means optimized, the results are quite encouraging - particularly those on PDMS- $\text{SiO}_2$ - $\text{TiO}_2$  waveguides, where attenuations  $< 0.15$  dB/cm were obtained. Further, as illustrated by the data on  $n$  vs.  $\nu$  shown in Fig. B-15, it is possible to tailor the index-dispersion of POLYCERAMS over a wide range by expanding the chemistry involved.

Table B-10: Refractive index and attenuation at 632.8 nm of POLYCERAMS containing 80 vol. % polymer and oxide/SiO<sub>2</sub> = 1/1.

Composition	Index of Refraction	Loss $\pm$ st. dev. (dB/cm)
MPEOU-SiO <sub>2</sub> -GeO <sub>2</sub>	1.507	2.08 $\pm$ 0.57
MPEOU-SiO <sub>2</sub> -ZrO <sub>2</sub>	1.562	3.27 $\pm$ 0.20
MPEOU-SiO <sub>2</sub> -Ta <sub>2</sub> O <sub>5</sub>	1.631	1.71 $\pm$ 0.25
MPEOU-SiO <sub>2</sub> -BaO	1.525	6.09 $\pm$ 0.480
MPEOU-SiO <sub>2</sub> -ZnO	1.495	5.02 $\pm$ 0.51
PDMS-SiO <sub>2</sub> -TiO <sub>2</sub>	1.514	< 0.15

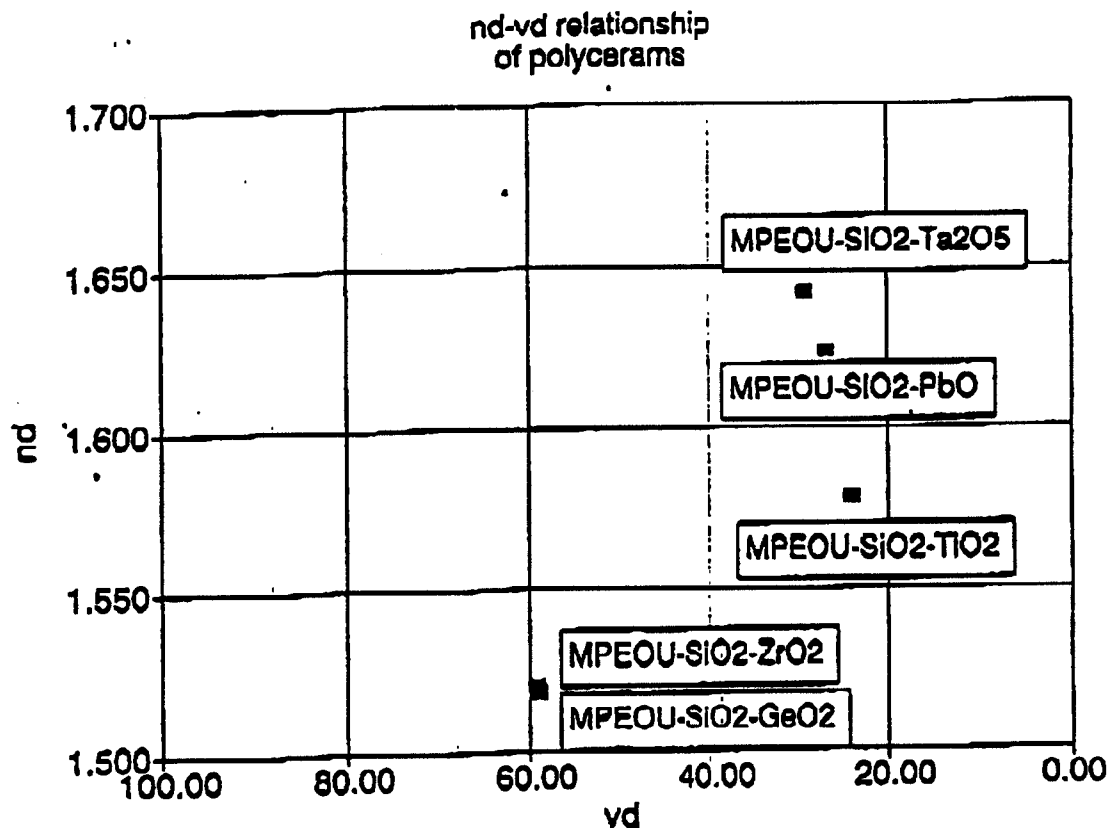


Fig. B-15 A map of  $n_d$ - $v_d$  of POLYCERAMS with different compositions showing a wide tailoring capability.

Work is presently being focussed on optimizing the chemistry and processing of waveguides with this broader range of chemistry to produce materials with losses in the sub - 1 dB/cm range. In addition, the attenuation will be determined as a function of wavelength to provide further insight into

the mechanism of loss in these materials.

It has been demonstrated, therefore, that planar waveguides with attenuations  $<0.15$  dB/cm can be synthesized in at least two POLYCERAM systems (MPEOU-SiO<sub>2</sub>-TiO<sub>2</sub> and PDMS-SiO<sub>2</sub>). These attenuations are similar to the lowest which have been reported for any planar waveguide prepared from any material. It has also been demonstrated that the optical properties of the POLYCERAMS can be tailored over a broad range, and that the processing of POLYCERAM planar waveguides can be carried out using very simple and cost-effective methods. The combination of these characteristics makes POLYCERAMS highly attractive for such applications. Patent disclosures are being prepared with respect to these developments.

The exceptionally low attenuations achieved in these POLYCERAM waveguides are remarkable in light of the highly disparate chemistries and optical properties of their constituents. The data imply a high degree of chemical and physical homogeneity down to almost the molecular level.

In addition to having a low loss, it is important for the optical waveguide to be connected to other optical components. Surface corrugation waveguide gratings have been demonstrated successfully as efficient and rugged interconnects between planar waveguides and external optical components.



such as sources and detectors. In addition, waveguide gratings can provide efficient coupling (near 100%) between guided-wave components, detectors, and diode lasers in planar integrated optic circuits. With this in mind, we undertook an investigation of the ability of POLYCERAMS to hold the shape of waveguide gratings. Because of the extensive relaxation demonstrated by POLYCERAMS, it seemed a priori unlikely that waveguide gratings could successfully be embossed in these materials.

The patterning of POLYCERAMS was conducted using an embossing technique. A surface-relief master grating was transferred to the gel film by creating a line pressure contact as the master is pressed into the film. Surprisingly, it was found that POLYCERAMS in the  $\text{SiO}_2\text{-TiO}_2\text{-MPEOU}$  system can be embossed to produce gratings with a peak-to-trough depth of 200 Å - and this exploration is still in its infancy. It was also found (also surprisingly) that the maximum depths are obtained with no heat-treatment prior to embossing: Pre-heating for 5 - 10 min. at 125C stiffens the structure and reduces the ability of POLYCERAMS to be embossed. Fig. B-16 shows AFM micrographs of surface corrugations on POLYCERAMS with peak-to-trough depths of 40 Å and 200 Å. It is seen that the embossed gratings are periodic and show no apparent flaws. The lateral and longitudinal shrinkage

as well as the periodicity of the gratings are currently being studied optically through measurement of the grating diffraction efficiencies (with the gratings used in transmission). These measurements are being conducted with different heating cycles to determine the shrinkage characteristics of the POLYCERAM and their relation to the grating structures which are obtained. In addition, the pressure and time of embossing are being optimized to produce deeper gratings.

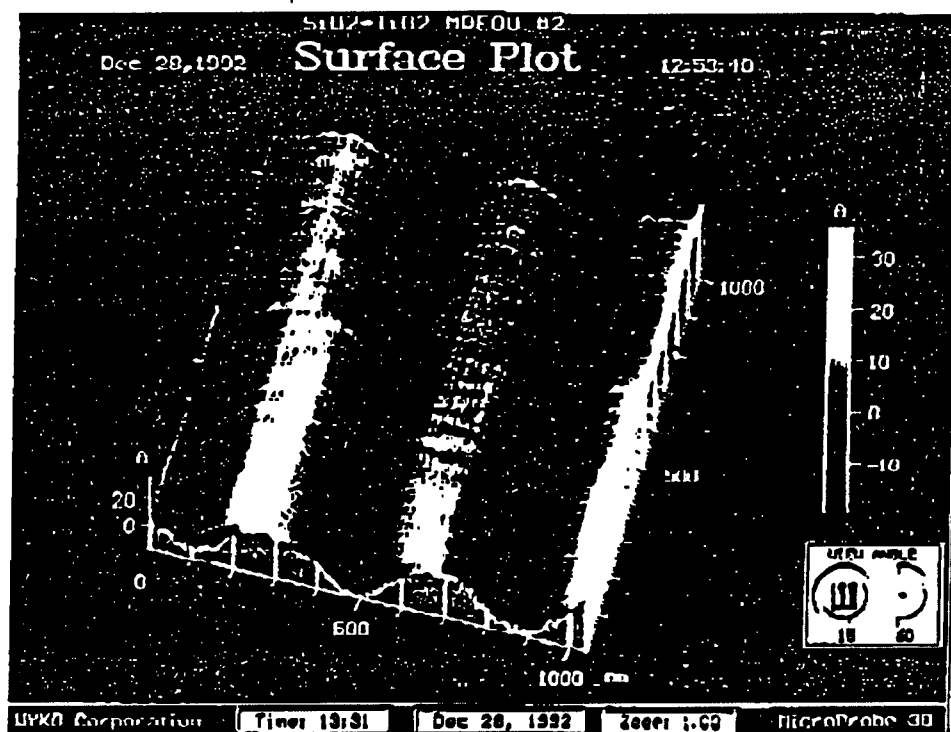


Fig. B-16a Surface profiles of embossed waveguides. Part a) shows a 40 Å peak-to-trough depth and part b) shows a 200 Å peak-to-trough depth.

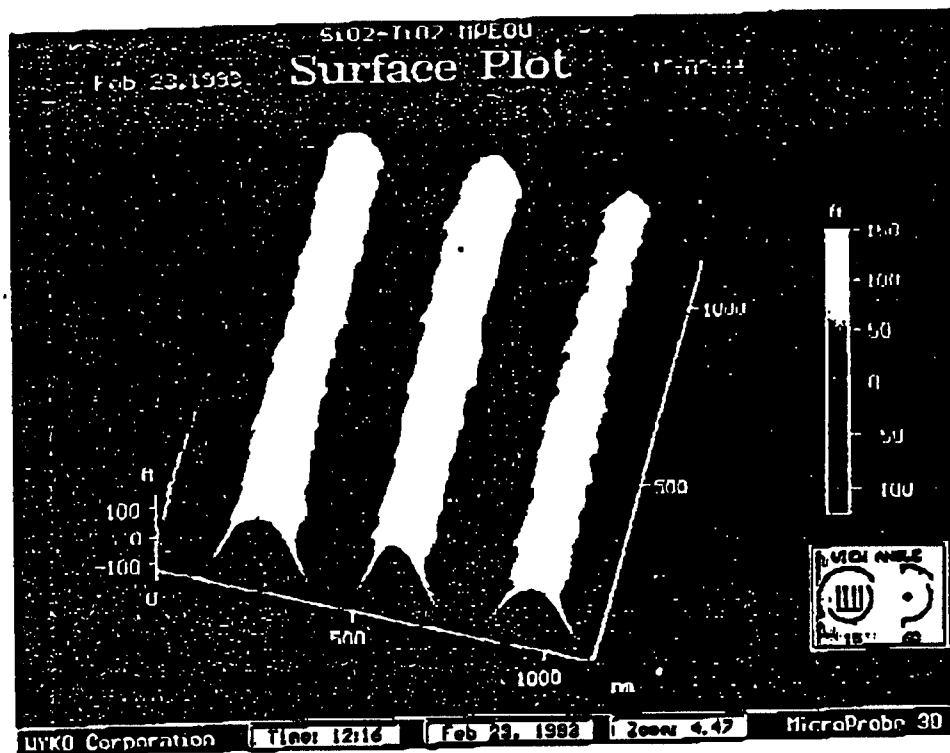


Fig. B-16b

These results, while preliminary, are highly encouraging. They offer great promise for opening an entirely new area of applications for POLYCERAMS in integrated optical devices.

Perhaps the most exciting potential application of POLYCERAMS is in the area of active waveguides, where they can be used as hosts for various

lasing elements or dyes. The low losses ( $<0.15$  dB/cm) obtained in the present POLYCERAMS, coupled with the ability to tailor their chemistry and properties, indicate that they are attractive candidates for such purposes. Inorganic lasing ions being incorporated in these materials include  $\text{Nd}^{+3}$  and  $\text{Er}^{+3}$ . To obtain a suitable lasing medium, it is important to disperse homogeneously the lasing ions ( $\text{Nd}^{+3}$  and  $\text{Er}^{+3}$ ) in the host. Clustering of ions can cause concentration quenching of the fluorescence. Thus, the present approach represents an attractive technique for producing homogeneous lasing media containing arbitrary concentrations of the lasing ions. In work carried out to date a number of MPEOU- $\text{SiO}_2$ - $\text{TiO}_2$  and MPEOU- $\text{SiO}_2$ - $\text{Al}_2\text{O}_3$  POLYCERAMS have been synthesized with different compositions of  $\text{NdCl}_3$  salt. Collaboration with Dr. R. Zanoni at the Center for Laser Research at Oklahoma State University is currently underway to explore the luminescence properties of such POLYCERAMS. Thus far, a  $5 \mu\text{s}$  fluorescence lifetime has been obtained in a MPEOU- $\text{SiO}_2$ - $\text{TiO}_2$  POLYCERAM doped with 3 wt %  $\text{NdCl}_3$ . Current work is directed to optimizing the chemistry and the processing of the films to obtain longer lifetimes. Residual hydroxyl bonds are known to decrease fluorescence lifetime in lasing media. Thus, it is important to dry thoroughly the films to ensure fewer such bonds. In order to eliminate the ion

clustering problem, we have recently synthesized Nd alkoxide for use as a precursor in place of Nd salts. Use of this alkoxide should increase the level of homogeneity through hydrolysis/condensation processes, thus enhancing the lasing properties of the POLYCERAMS. Finally, the incorporation of  $\text{Al}_2\text{O}_3$  in the POLYCERAMS seems promising in light of previous lasing studies of optical glasses, which indicated that Al decreases concentration quenching. Different concentrations of  $\text{Al}_2\text{O}_3$  are being used to determine the required composition for optimal lasing properties.

We have also recently synthesized a number of MPEOU- $\text{SiO}_2$ - $\text{TiO}_2$  POLYCERAMS doped with 0.5-3 wt %  $\text{Er}_2\text{O}_3$  as thin films as well as bulk forms. It has been observed that prism coupling in a thin film of POLYCERAM doped with 1 wt. %  $\text{Er}_2\text{O}_3$  results in a 100  $\mu\text{V}$  fluorescence signal. This composition corresponds to a concentration of  $10^{18} \text{ Er}^{+3}/\text{cm}^3$ . In Er-doped glasses, a concentration of  $10^{19} \text{ Er}^{+3}/\text{cm}^3$  is found to be the maximum limit before clustering of ions becomes detrimental to fluorescence signals; and POLYCERAMS containing these and higher concentrations are presently being synthesized.

Experiments are also being conducted on Er-doped POLYCERAM films covered with a cladding layer of a lower index. The cladding layer will ensure

better confinement of the streak within the Er-containing layer. Since ytterbium (Yb) is known as a good sensitizer for Er - i.e., Yb has absorption bands in the regions where Er does not absorb, and is capable of transferring energy to the lasing Er - we have synthesized Yb alkoxides to be co-doped with erbium in order to increase the fluorescence intensity and lifetime.

In slab waveguides, the streak often begins to fan out after a few cm in the film. A longer streak is preferred because absorption of the input energy by Er ions increases with increasing path length. It is desired to confine the streak laterally, thus preventing its fanning out and loss of energy. Work is currently underway in fabricating Er-doped channel waveguides with lateral dimensions of 1 to 10  $\mu\text{m}$ . Both sides of the channel must be polished in order to minimize energy losses from the edges. Collaboration is underway with the Optical Sciences Center at the University to determine the lasing properties of these Er-doped POLYCERAM waveguides.

contact or corona discharge poling. Corona poling of thin films is preferred because a top electrode is not required, poling can be achieved over larger areas, and microscopic shorts do not occur due to defects in the film.

POLYCERAM hosts for NLO dyes offer several advantages over polymer hosts. These include improved orientational and thermal stability, higher laser damage thresholds, and ability to tailor properties (e.g., refractive index, optical transparency) through variations in composition and processing. During the present year, 2-methyl-4-nitroaniline (MNA) and N-(3-triethoxysilyl-propyl)-2,4 dinitrophenylamine (TDP) NLO dyes have been incorporated in  $\text{SiO}_2\text{:TiO}_2$  POLYCERAMS. The structure of these dyes is illustrated in Fig. C-1. MNA was chosen as an example of a small molecule with high NLO coefficients, and TDP as example of a functionalized dye with attractive NLO coefficients which can be bonded directly into the inorganic matrix. Bonding to the matrix was expected to provide greater orientational stability as well as thermal stability, and should allow greater concentrations of dye to be incorporated in the host without aggregation. High concentrations of appropriate dyes with high degrees of chromophore alignment should provide high values of NLO and electro-optic coefficients.

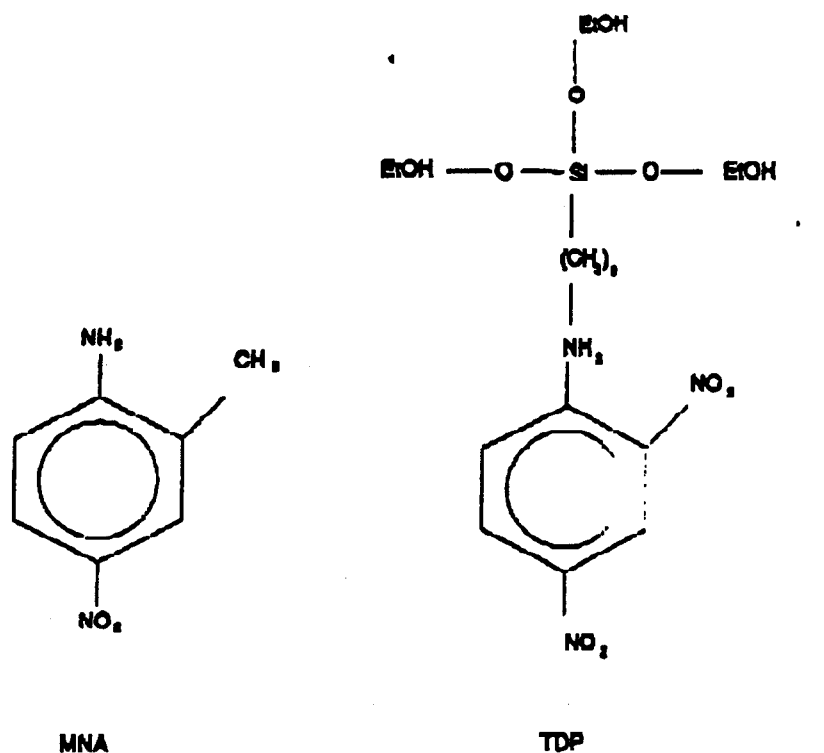


Fig. C-1 Structure of NLO Chromophores

The POLYCERAMS synthesized to date in this phase of the investigation were prepared from tetraethoxy silane (TEOS) and titanium isopropoxide (TIP) in a  $\text{SiO}_2/\text{TiO}_2$  molar ratio of 1/2. Conditions of partial



hydrolysis ( $\text{H}_2\text{O}/\text{TEOS} = 2/1$  molar) were employed to produce POLYCERAMS with low attenuation (see Section B above). Triethoxysilylpropyl-modified poly(ethylene oxide)urethane (MPEOU) was used as the polymer constituent, and was employed at 80 vol. % concentrations. After refluxing and incorporation of the respective dyes in the solutions, films on Corning 7059 glass coated with a transparent conductor (ITO) were prepared by spin casting.

To achieve orientation of the dyes in the POLYCERAMS, the films were subjected to a corona poling treatment. The apparatus shown schematically in Fig. C-2 was employed for this purpose, using a tungsten needle as one electrode and the ITO layer as the other. The discharge current was monitored; and the temperature of the film was raised for some samples to accelerate drying and to freeze the oriented molecules in place.

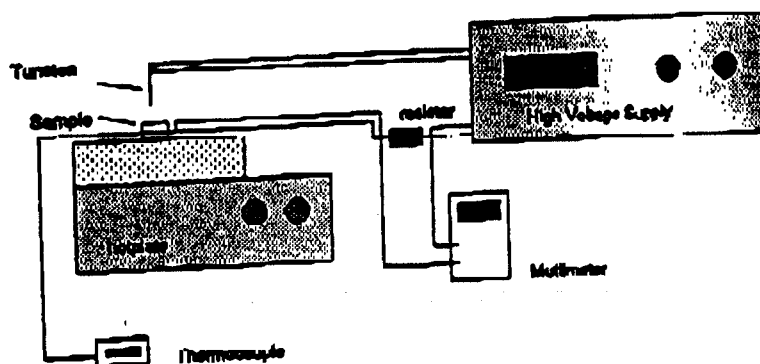


Fig. C-2 Schematic of Corona Poling Setup

The absorption spectra of  $\text{SiO}_2/\text{MPEOU}$  and  $\text{SiO}_2:\text{TiO}_2/\text{MPEOU}$  POLYCERAMS are shown in Fig. C-3. The  $\text{SiO}_2$  POLYCERAM has a UV cutoff at 255 nm. The addition of  $\text{TiO}_2$  resulted in an absorption peak at 290 nm. Absorption only in the UV region of the spectrum explains the high transparency in the visible region of the spectrum (380-780 nm) for these POLYCERAMS. The addition of MNA resulted in an absorption peak at 375 nm. The addition of TDP resulted in two absorption peaks: one at 350 nm and a smaller one at ~410 nm. The absorption peaks of these aromatic dyes can be attributed to excitation of the  $\pi$ -molecular orbital ( $\pi$ - $\pi^*$  transition).

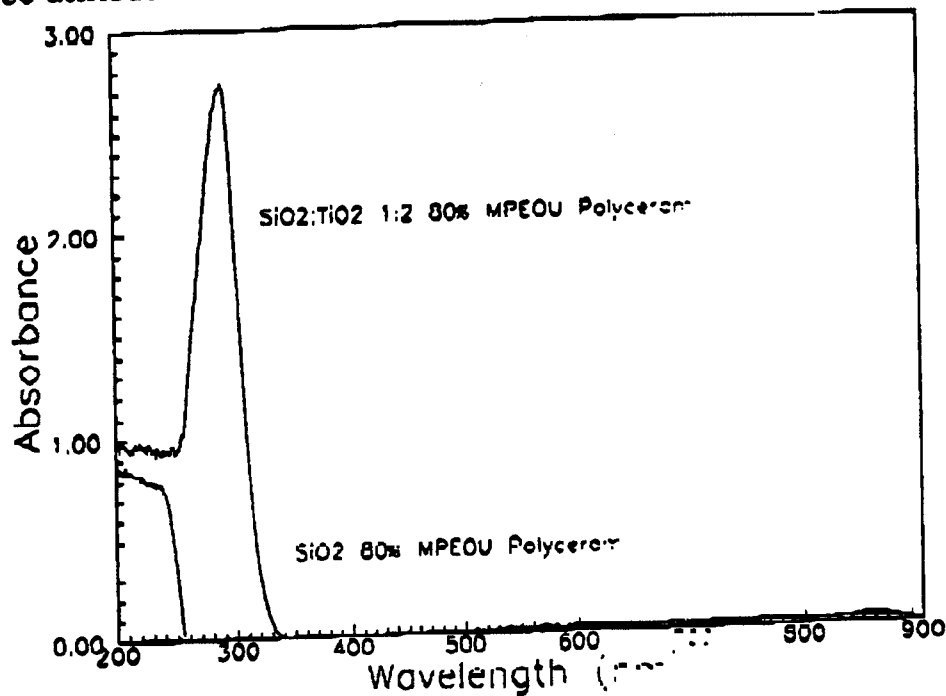


Fig. C-3 Polyceram adsorption spectra

The degree of orientation of the dye molecules was measured by evaluating the change in the absorption spectrum before and after poling. The order parameter, which measures the degree of orientation, is given by:

$$\phi = 1 - \frac{A_1}{A_0}$$

where  $A_0$  is the magnitude of the absorption peak before poling, and  $A_1$  is its magnitude after poling. A derivation of this order parameter is provided in Appendix A following this section.

Corona poling was performed on the samples during drying to provide the largest degree of mobility of the NLO chromophores to orient. Corona poling of previously dried POLYCERAM films resulted in little orientation and a large degree of damage to the film surface. Dried and condensed films offer little free volume for the dye molecules to orient during poling. Poling at elevated temperatures of wet films resulted in a large degree of orientation in TDP POLYCERAMS. Due to sublimation of MNA from the host at elevated temperatures, corona poling of MNA POLYCERAMS was performed at room temperature.

Using the order parameter as a guide, optimum corona poling conditions were determined. Fig. C-4 is a plot of the absorption spectra of TDP POLYCERAMS poled at different discharge currents.

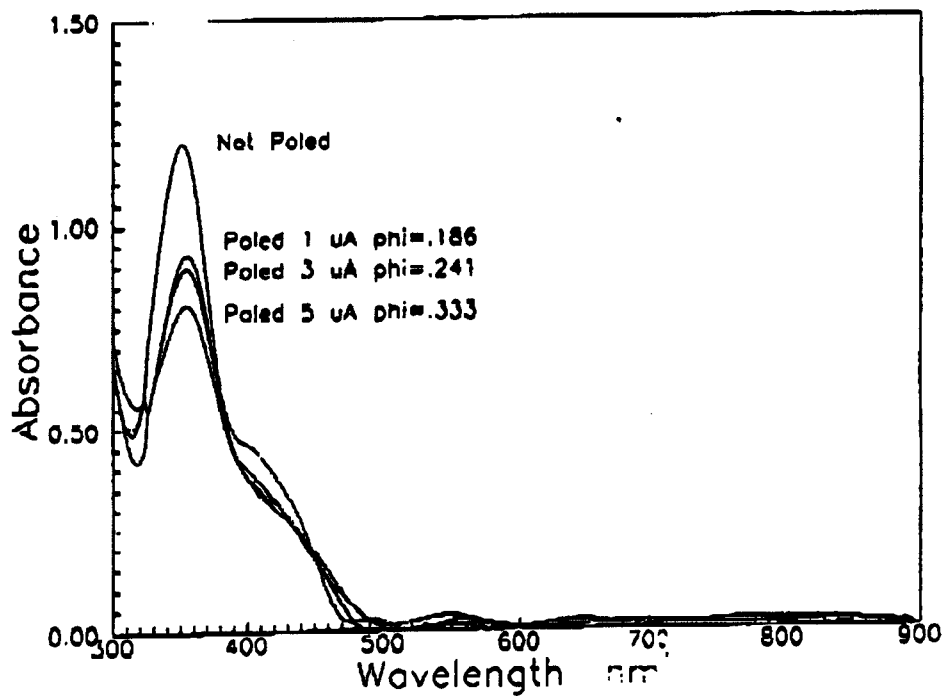


Fig. C-4 Orientation vs. poling discharge current.

It is seen that poling at larger discharge currents results in larger degrees of orientation. The increase in orientation of the dye with increase in discharge current is attributed to larger charge accumulation on the film surface, resulting in a larger field across the film. Some samples were poled at  $8\ \mu\text{A}$  and  $10\ \mu\text{A}$ , which resulted in significant damage to the film surface; and the order parameter was not measurable. Poling at discharge currents of  $5\ \mu\text{A}$  and below resulted in optically clear films.

Fig. C-5 shows the order parameter of TDP POLYCERAM films poled for different times. Increase in the poling time beyond 20 min. did not provide any further orientation. Apparently the drying and condensation of the films at  $120^\circ\text{C}$  within 20 min. result in a sufficient decrease in the free volume to prevent any further orientation.

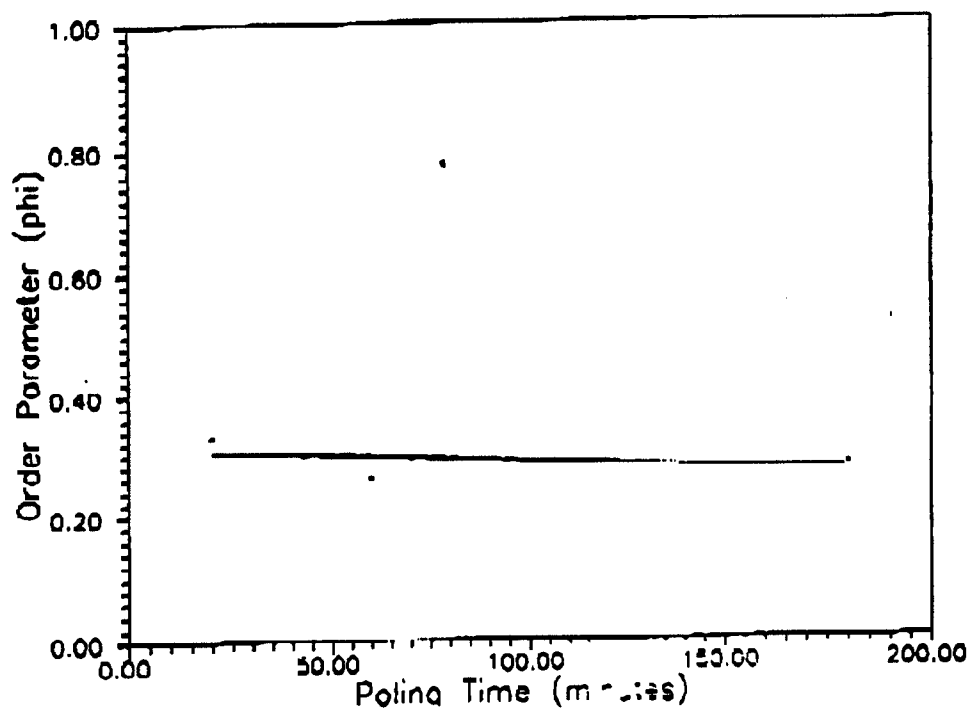


Fig. C-5 Order parameter vs. poling time.

As indicated above, the MNA POLYCERAMS were poled at room temperature. Very high degrees of orientation were obtained ( $\Phi = .626$ ). To the best of the investigator's knowledge, this is the highest order parameter reported to date for any dye/host system. The high degree of orientation is attributed to the high mobility of the chromophore in the wet POLYCERAM film.

To confirm that the change in the absorption spectrum of the TDP POLYCERAM films after poling was due to chromophore orientation and not dye loss or decomposition during heat treatment to the films, a thermal stability test was performed. UV-Vis absorption spectrum was measured on a sample after consecutive heat treatments at 75, 125, 175, 200C for 25 hrs. at each temperature. As seen in Fig. C-6, heat treatment at temperatures of 125C and below produced little or no change in the absorption spectra. Between 125 and 175C, loss or decomposition of the dye resulted in the observed decrease in the absorption spectrum. From these results, it is confirmed that the change in the absorption spectrum from poling at 120C reflects an orientation of the TDP in the film and not loss or decomposition of the dye.

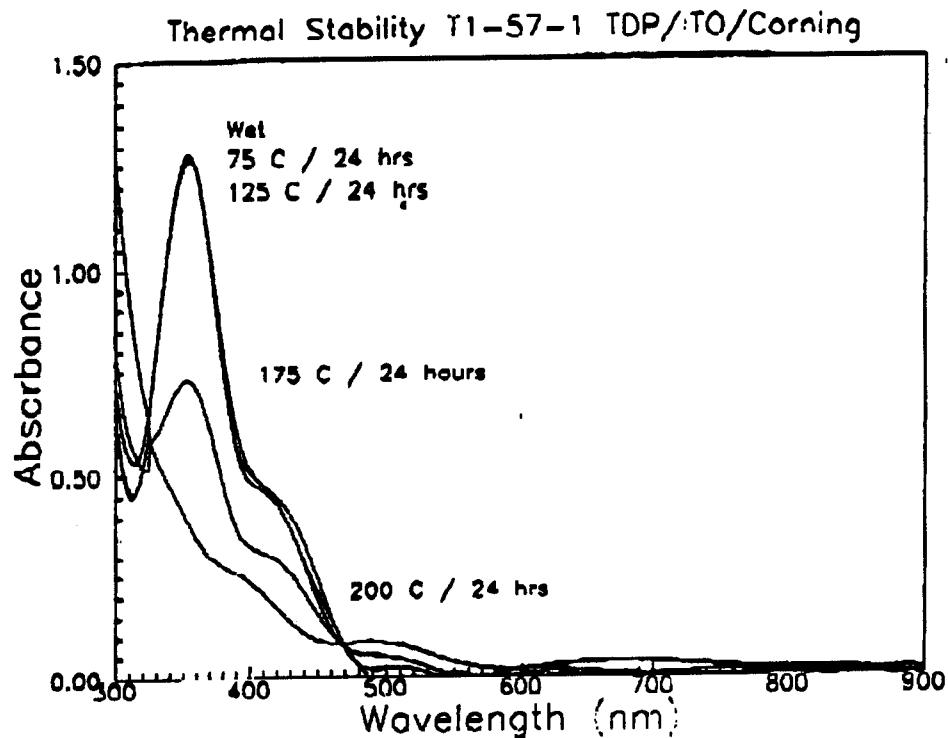


Fig. C-6 Thermal stability.

The orientational stability of the films at room temperature was evaluated by measuring the absorption spectrum at different times after poling: see Fig. C-7 for a poled TDP POLYCERAM film. Two months after poling, no observable relaxation is seen. This is the highest degree of orientational stability seen for this dye in any host, and one of the highest such stabilities seen for any NLO dye in any host. The present results confirm the potential of combining functionalized dyes with POLYCERAM hosts and appropriate



processing to achieve structures with exceptional degrees of orientational stability.

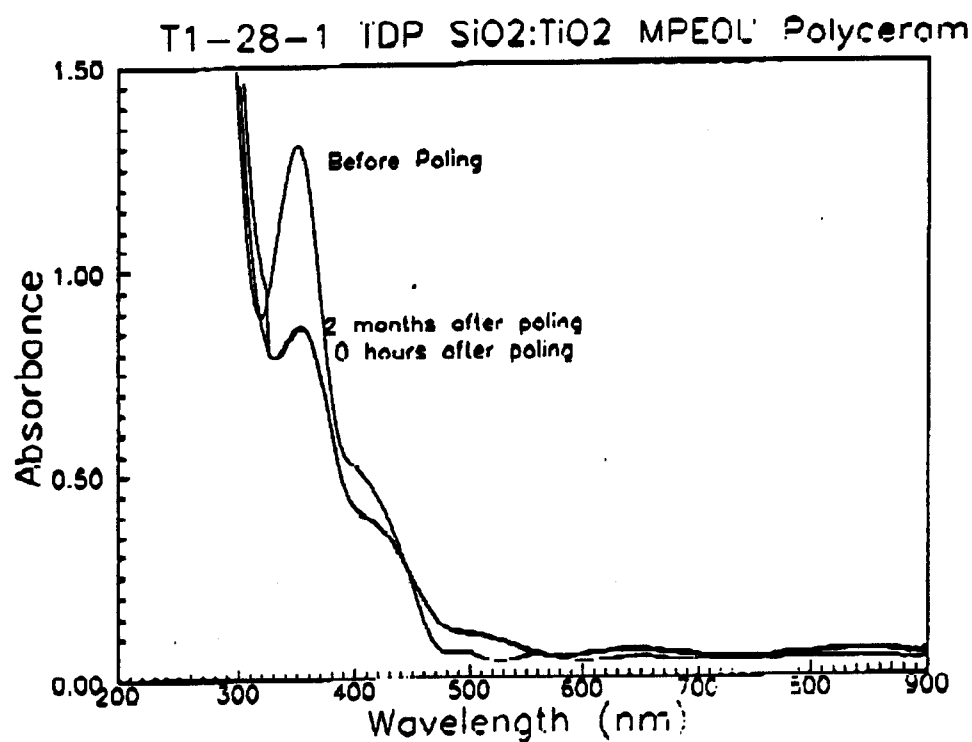


Fig. C-7

Due to MNA loss from the films through sublimation, orientational stability of the poled MNA POLYCERAM films could not be evaluated

accurately. Ten days after polling, the absorption peak showed an increase (Fig. C-8), suggesting that relaxation is taking place. A sample that was not poled showed, however, a significant decrease in the absorption peak in ten days (Fig. C-9). These results suggest that two processes are taking place in the MNA POLYCERAM films upon aging: loss of MNA by sublimation and relaxation of the oriented dye molecules. The results also support the desirability of using functionalized dyes to achieve permanency of the dyes in the structure as well as high orientational stability.

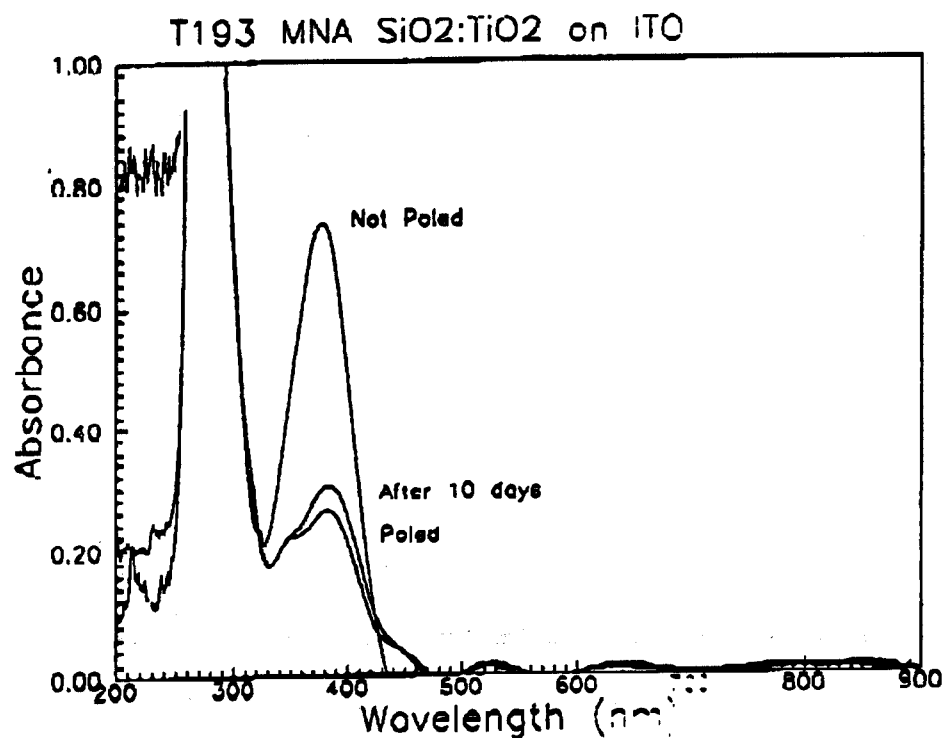


Fig. C-8

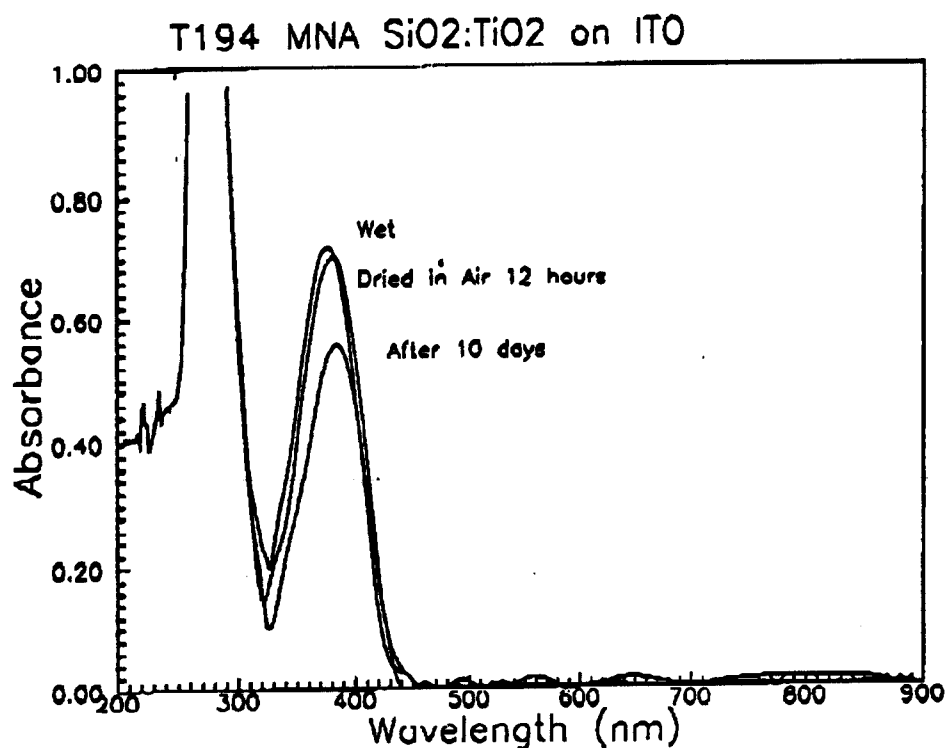


Fig. C-9

The Index of refraction of the dye doped POLYCERAMS was evaluated using ellipsometry at 633 nm. As shown in Table C-1, the refractive index of the undoped POLYCERAM was 1.63. Addition of 27 wt % TDP increases the refractive index to 1.688. A poled film with the same dye content has a refractive index of 1.63. Orientation of the dye perpendicular to the film surface resulted in the reduction of the refractive index of the film. The ellipsometric measurements made on the poled samples had a larger degree

of error than that in measurements on samples which were not poled. This is attributed to the induced birefringence caused in the POLYCERAM by poling (i.e., the film is no longer isotropic) as well as index inhomogeneity around the highly poled area of the film.

Refractive index measurements of the MNA-doped POLYCERAMS showed different results. Addition of 3.6 wt. % MNA to the POLYCERAM resulted in a decrease in the refractive index to 1.56. Poling of the MNA-doped POLYCERAM resulted in an increase in the refractive index to 1.626.

**Table C-1: Properties of NLO Dye doped POLYCERAMS**

Dye/Host	Concentration	Process	Refractive Index	Thickness	$\Phi$
TDP/ Polyceram	27 wt%	Not Poled	1.688	1.348um	Not measur- able
TDP/ Polyceram	27 wt%	Poled	1.630	1.358um	N/A
TDP/ Polyceram	15.8 wt%	Poled	--	--	.33
MNA/ Polyceram	3.6 wt%	Not Poled	1.557	.839um	N/A
MNA/ Polyceram	3.6 wt%	Poled	1.626	.867um	.626

The origin of this difference in behavior is presently being explored, analytically as well as experimentally. Kramers-Kronig analysis of the change in the absorption spectrum before and after poling has been used to describe the change in refractive index due to orientation as a function of wavelength.

Because of the great interest in developing active waveguides for electro-optic and NLO application, effort was undertaken during the present year to fabricate planar waveguides of the dye-doped POLYCERAMS. Because the higher index of the ITO layer was higher (1.73) than that of the POLYCERAM films (1.63-1.68), waveguiding in the POLYCERAM-on-ITO

configuration is not possible. The use of different substrates and buffer layers was therefore investigated to fabricate waveguides. Since direct poling is possible on substrates if the resistivity of the substrate is fairly low, Pyrex and soda lime glasses were explored as substrates. Corona poling was successful on these substrates; but the degree of orientation was not very good ( $\Phi < .20$ ). This is attributed to a lower potential drop through the POLYCERAM film with a Pyrex or soda-lime glass substrate. (Part of the total potential drop takes place through the substrate.) Higher voltages were applied during corona poling; but this resulted in film damage or substrate breakdown.

The use of buffer layers with a lower refractive index proved more successful, such as POLY(methyl methacrylate) (PMMA) ( $n=1.55$ ) and MPEOU-SiO<sub>2</sub> POLYCERAM ( $n=1.495$ ). In the case of the PMMA buffer layers, prism coupling waveguide measurements revealed good waveguide characteristics (e.g., sharp TE and TM m-lines and visual light streaks seen across whole film). Corona poling of such samples was unsuccessful, however, due to problems with cracking of the POLYCERAM films, likely due to differential shrinkage and/or differences in thermal expansion. Preliminary results obtained with the MPEOU-SiO<sub>2</sub> POLYCERAM as a buffer layer also indicated good waveguide characteristics. This approach provides higher

degrees of dye orientation than use of the Pyrex or soda-lime glass substrates or PMMA as a buffer layer. The orientation achieved in these preliminary studies is, however, lower than that obtained when the dye-doped POLYCERAM is directly contacted with the ITO. Further work is presently being directed to improving both the orientation and waveguide characteristics of configurations with a dye-doped, high index POLYCERAM active layer on an undoped, low index POLYCERAM buffer layer.

In summary, both MNA and TDP dyes have been incorporated in POLYCERAM hosts, and have been oriented by corona poling during drying of the films. Significant orientation of the dye molecules has been achieved. Using the functionalized TDP dye, exceptional orientational stability has been demonstrated, with no observable relaxation of the orientation being seen even after two months at room temperature. Waveguiding has been successfully demonstrated in several configurations of poled POLYCERAM films. In current work, the chemistry and processing are being optimized to improve the optical quality of the corona-poled, dye-doped POLYCERAMS for waveguiding. Special attention is being paid to improving surface roughness of both the dye-doped films and the buffer layers through the addition of chelates.

## Appendix A: Derivation of Order Parameter

The following derivation of the order parameter is performed to show that the degree of orientation of the dye molecules can be measured by a change in the absorption spectrum of the dye/host material before and after poling. If the interactions of the guest molecules is negligible (i.e., homogeneous mixture of dye), a rigid orientated gas model (ROGM) can be used to describe the system. First, a mathematical description of the degree of orientation is obtained. Then its relationship to the optical absorption is described.

In the ROGM, the dye molecules are described as cylindrical rods having a static dipole moment within an isotropic host medium (Fig. CA-1). Initially the dipole moments are randomly orientated within the host material. The direction of a particular dipole moment ( $\mathbf{r}$ ) is described in spherical coordinates. The cartesian and spherical coordinate system are described with respect to the film in Fig. CA-1. The degree of alignment can be described by a distribution function:

$$f(\theta, \phi) d\Omega$$



where  $d\Omega$  is the solid angle which is defined as:

$$d\Omega = \sin\theta \, d\theta \, d\phi$$

The distribution function can be thought of as the probability of finding a molecule in a small solid angle. When cylindrical symmetry of the system is assumed, the distribution function becomes independent of  $\phi$ . The distribution function simplifies to the following:

$$f(\theta) \sin\theta \, d\theta$$

For a random distribution of dye molecules the distribution function is described as follows:

$$f(\theta) \sin\theta \, d\theta = \frac{1}{2} \sin\theta \, d\theta$$

Plotting  $f(\theta)$  vs  $\theta$  for the random case, results in a straight line, indicating that there is equal probability of finding the dye molecules in all directions.

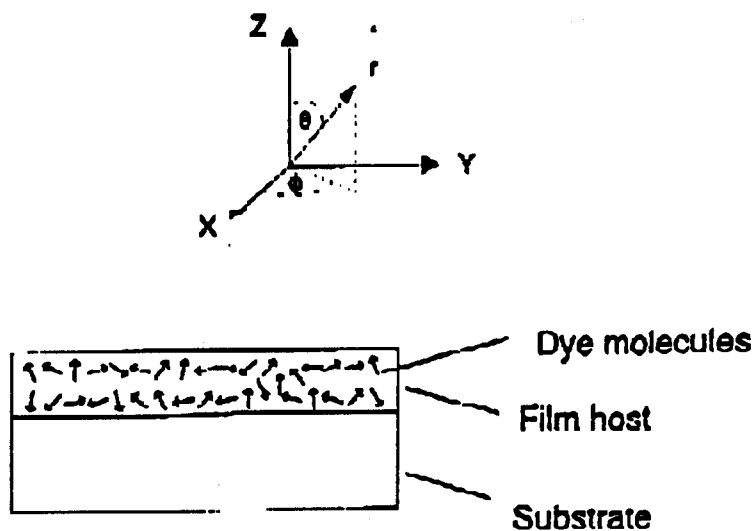


Fig. CA-1: Schematic of random distribution of Dye molecules in host.

Upon application of an electric field ( $E_z$ ) parallel to the z-direction, the energy that forces a particular dipoles to orientate parallel to the field is described as:

$$\mu_z \cdot E_z = |\mu_z| |E_z| \cos \theta$$

where  $\mu_i$  is the dipole moment for the  $i$ th dye molecule and  $E_z$  is the local electric field in the  $z$ -direction which acts on the dye molecule. Since the distribution function is very difficult to determine experimentally, a single parameter can be defined which describes the degree of orientation. Such a quantity is the canonical ensemble average of the cosine of the angle between the dye dipole moment direction and the  $z$ -axis (i.e.  $\cos \theta$ ). This quantity is described as follows:

$$\langle \cos \theta \rangle = \frac{\int_0^\pi \cos \theta f(\theta) \sin \theta d\theta}{\int_0^\pi f(\theta) \sin \theta d\theta}$$

Unfortunately this quantity vanishes due to symmetry reasons. Therefore a higher order term which corresponds to the quadrupole moment is defined as the order parameter ( $\Phi$ ) which does not vanish.

$$\Phi = \frac{1}{2} \langle 3 \cos^2 \theta - 1 \rangle = \frac{1}{2} (3 \langle \cos^2 \theta \rangle - 1)$$

The order parameter can vary from 0 to 1. When  $\theta$  is 0 (i.e. when the direction of the dipole moment of the molecules and the applied field are parallel) then the order parameter is equal to one, indicating perfect order

(Fig. CA-2). When there is random orientation the order parameter is equal to 0. The distribution function for these two cases is illustrated in Fig. CA-3.

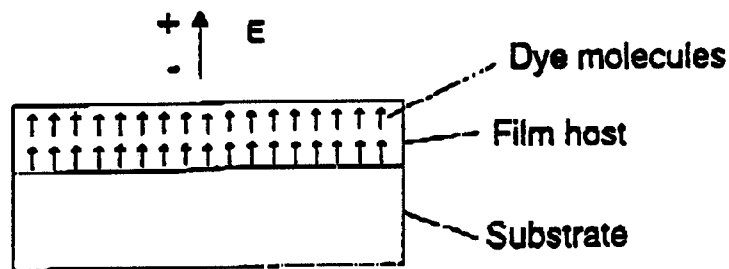


Fig. CA-2: Schematic of perfectly aligned dye/host system.

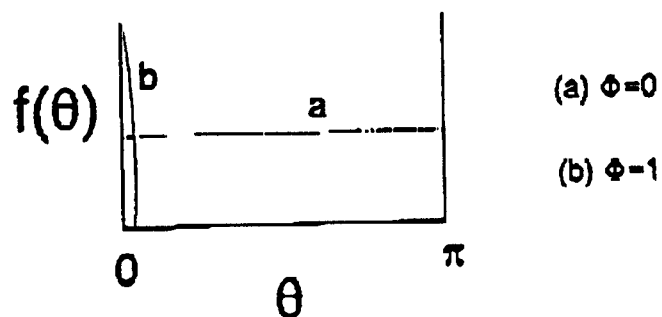


Fig. CA-3: Plot of Distribution Function

Now that a single parameter has been defined which describes the orientation order of the dye molecules in a host has been derived, a way must be determined to measure this quantity experimentally. The order parameter can be related to the inherent dichroism of the dye molecules. The static dipole moment of most organic dye molecules are parallel or have a small angle with the transition dipole moment for optical absorption. Therefore one can assume for this model that the optical absorption transition moment is essentially parallel to the static dipole moment. Also, if the induced dipole moment is negligible upon the application of electric field, then the parallel and perpendicular dichroisms can be defined as follows:

$$\frac{A_{\perp}}{A_0} = \frac{3}{2} \langle \sin^2 \theta \rangle$$

$$\frac{A_{\parallel}}{A_0} = 3 \langle \cos^2 \theta \rangle$$

where  $A_0$  is the absorbance in an isotropic medium (when dye molecules have random orientation),  $A_{\parallel}$  is the absorbance measured with the electric field

polarization of the incoming light parallel to the poling field direction, and  $A_1$  is the absorbance measured with electric field polarization of incoming light perpendicular to the poling field direction. Note that these absorbance values are at the wavelength at which optical transition takes place (i.e. absorption maximum).

By equating the order parameter and absorbance equations above with some trigonometric substitutions, the order parameter is determined as:

$$\phi = 1 - \frac{A_1}{A_0}$$

In order to measure the order parameter, only the absorption maximum before poling ( $A_0$ ) and after poling ( $A_1$ ) is needed. It is expected that the absorption peak will decrease upon poling since the optical transition moment is aligning parallel to the surface of the film and light is passing perpendicular to the film.

Due to the number of assumptions made in deriving the order parameter, the order parameter is used as a semi-quantitative evaluation of the amount of orientation taking place.

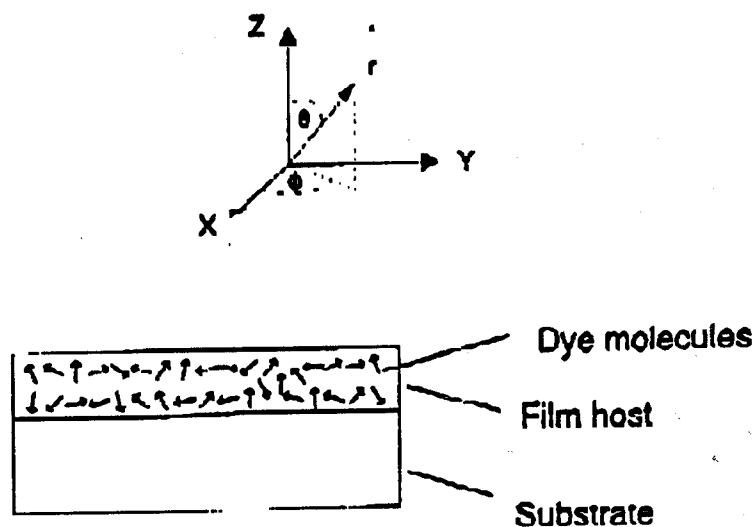


Fig. CA-1: Schematic of random distribution of Dye molecules in host.

Upon application of an electric field ( $E_z$ ) parallel to the z-direction, the energy that forces a particular dipoles to orientate parallel to the field is described as:

$$\mu_z \cdot E_z = |\mu_z| |E_z| \cos \theta$$

where  $d\Omega$  is the solid angle which is defined as:

$$d\Omega = \sin\theta \, d\theta \, d\phi$$

The distribution function can be thought of as the probability of finding a molecule in a small solid angle. When cylindrical symmetry of the system is assumed, the distribution function becomes independent of  $\phi$ . The distribution function simplifies to the following:

$$f(\theta) \sin\theta \, d\theta$$

For a random distribution of dye molecules the distribution function is described as follows:

$$f(\theta) \sin\theta \, d\theta = \frac{1}{2} \sin\theta \, d\theta$$

Plotting  $f(\theta)$  vs  $\theta$  for the random case, results in a straight line, indicating that there is equal probability of finding the dye molecules in all directions.



#### **D. GRADIENT REFRACTIVE INDEX LENSES FROM POLYCERAMS**

Gradient refractive index (GRIN) optical devices - especially lenses - are important in many present and emerging optical applications. GRIN devices contain a refractive index variation in one or more dimensions of a material, thereby enhancing the imaging and processing abilities of optical materials while simultaneously reducing the aberrations formed in traditional (single-index) optical materials. Notable examples of optical GRIN devices include multi-mode optical fiber waveguides and couplers, integrated optic waveguides, microlens singlets and arrays, and macro-scale lenses. Of particular note, large diameter (5-75 mm) GRIN lenses have been highly desired for numerous applications including photocopiers, film and video cameras, laser printers, scanners, and night-vision goggles.

GRIN materials utilize the direct relation between refractive index and the velocity of light propagating through a material, ie:

$$v = c / n$$

where  $v$  is the velocity of light in a medium with index of refraction  $n$  and  $c$  is the speed of light in a vacuum. Further, as the refractive index of a material varies, the direction of light propagation changes according to Snell's law:

$$\frac{\sin\theta_t}{\sin\theta_i} = \frac{n_1}{n_2}$$

where  $\theta_t$  is the angle of transmission,  $\theta_i$  is the angle of incidence, and  $n_1$  and  $n_2$  are the refractive indices of the incident and transmission regions, respectively. As light passes through a GRIN material, the change in refractive index ( $\Delta n$ ) effectively curves the light path while simultaneously retarding or accelerating the light velocity.

The most common optical GRIN device is the radial (r-GRIN) lens, schematically shown in Fig. D-1. The r-GRIN lens contains a symmetrical 2-D refractive index gradient about the cylinder axis. By using a suitable parabolic refractive index profile, all light rays incident on the end face of the lens propagate through the lens with a constant period due to the slower velocity of light near the center and faster velocity (lower index) near the lens edge. The constant period of the light allows a range of processing, including collimation into a parallel rays, focusing (down to a point), or magnification, as indicated in Figs. D-2 and D-3.

Conventionally, GRIN lens structures are formed by the surface modification of glasses, porous sol-gels, or polymers. However, such techniques and materials are very limited in the depth, profile, and magnitude ( $\Delta n$ ) of the

refractive index gradient that may be introduced into a material. The surface modification processes used in the commercial production of r-GRIN glass rods--from which r-GRIN lenses are cut--can be both time-consuming and expensive because of the ion exchange process employed to develop the index profile. The K-for-Tl exchange is carried out in a fused salt bath at temperatures exceeding 450 C; and the requirement for reasonable times of such exchange (1~30 days) has limited the available size of r-GRIN lenses to approximately 1 cm in diameter. Further, the magnitude of the available  $\Delta n$  from conventional processing is restricted to about 0.01.

The application of new POLYCERAM materials in the formation of GRIN structures appears to offer an outstanding opportunity for creating large diameter lenses with exceptional control over the depth, shape, and magnitude of the refractive index profile. The optical properties of POLYCERAM materials are comparable to those of optical glasses; and the ease of formation and thermal stability of POLYCERAMS make them highly attractive for forming GRIN lenses.

The processing of POLYCERAM materials provide a highly attractive method of incorporating refractive index-modifying oxides or polymers into the structure. As indicated in Section B above, for example, refractive index

changes as large as 0.23 may easily be produced by varying the chemistry and volume fraction of the inorganic components in MPEOU-SiO<sub>2</sub>-TiO<sub>2</sub> POLYCERAMS. This  $\Delta n$  is much larger than that achieved by any other GRIN processing technique. Further, the ability to form POLYCERAM materials without the deleterious cracking associated with the drying of sol-gel-derived oxides, makes it particularly attractive to explore POLYCERAMS for a range of GRIN devices.

Over the past year, the PI team has developed the ability to form large diameter r-GRIN lenses having a large  $\Delta n$  from POLYCERAMS. The results obtained to date have been highly encouraging; and a number of patent disclosures will shortly be prepared on the concept and preferred embodiments.

#### POLYCERAM r-GRIN Material Synthesis

POLYCERAMS offer the potential for large variations in refractive index, depending primarily upon the oxide constituents and to a lesser extent on the organic-modifying component. An initial survey was therefore carried out of several polymers combined with SiO<sub>2</sub>- and SiO<sub>2</sub>/TiO<sub>2</sub>- oxides. Resulting from this work, MPEOU was selected as the initial polymer of choice

because of the low levels of small angle x-ray scattering exhibited by POLYCERAMS containing this polymer.

Based upon previous results on POLYCERAM optical waveguides (see Section B above), a standard synthesis route was utilized, as indicated in Fig D-2. Particular to the formation of precursor solutions for forming GRIN rods was the use of a stirring step for 24 hours to obtain coating solutions with stable viscosities. The solutions were stored in tightly capped bottles at 0°C prior to use.

#### Formation of GRIN Lenses

##### Coating Concept and Procedure

The dip-coating technique was selected for the formation of POLYCERAM r-GRIN lenses because of its relative simplicity and ability to alter uniformly the  $\Delta n$  of the GRIN lens as a function of increasing radius. To achieve the desired variation in refractive index, two POLYCERAM solutions were used, typically with the addition of a low- $n$   $\text{SiO}_2$ -based solution to a high- $n$   $\text{SiO}_2/\text{TiO}_2$  solution. A computer-controlled peristaltic pump was used to uniformly add the secondary solution to the primary bath in a manner such that a desired refractive index profile was created. By the serial dipping of a

thin POLYCERAM bait-rod into the solution bath, a bulk POLYCERAM rod was formed.

A machine was constructed to form r-GRIN rods by serial dip coating. As indicated in Fig. D-5, the relevant features of the apparatus constructed include a computer-controlled vertical stepper motor and peristaltic pump, rotator motor, oven, protective quartz tube, solution bath, stirrer, and air-tight enclosing superstructure.

The use of a computer-interfaced stepper motor allows accurate positioning (better than  $1\text{ }\mu\text{m}$ ) and a vertical travel of 36 cm; similarly, the computer-interfaced peristaltic pump has a resolution of  $1.5\text{ }\mu\text{l}$ . A small motor was used to rotate the sample during drying in a 20 cm high, 10 cm diameter oven maintained typically at  $120^{\circ}\text{C}$ . Located approximately 25 cm below the oven was a water cooled base, magnetic stirrer, and POLYCERAM solution bath. The water cooled bath was maintained at a constant  $18^{\circ}\text{C}$  to minimize solvent evaporation during the coating process; a magnetic stirrer allowed the solution to be agitated and homogenized continuously. Adjacent to the bath was the peristaltic pump and secondary solution container.

As indicated in Fig. D-6, the coating process consists of repeating only 7 steps. The sample is initially lowered toward the solution bath at high speed

while the solution is stirred. Prior to immersion in the solution, the stirring and sample rotation cease. Immersion and withdrawal occur at a slow speed ( $< 1$  mm/sec). Withdrawal is followed by dispensing controlled additions of the secondary solution and resuming sample rotation and solution stirring. The sample is rapidly raised into the oven to dry the added coating layer; and the process is repeated to complete the desired number of coatings.

The computer control provides consistent immersion of the GRIN rod, so as to form a uniform cylindrical rod. This is achieved by considering the volume depletion of the solution bath (in forming the coating) and addition of secondary solution to the bath. Further, the computer allows precise control and variation of the time and rate of the heating, drying, cooling, immersion, and withdrawal parameters. A list of coating machine parameters is given in Table D-1.

GRIN rods were typically formed using tailored and varying amounts of  $\text{SiO}_2/\text{TiO}_2$ -MPEOU ( $\text{Si/Ti} = 2$ ,  $n = 1.634$ ) and  $\text{SiO}_2$ -MPEOU ( $n = 1.495$ ), both containing 60% MPEOU by wt. A 250 coat ( $\sim 1$  cm diameter) lens was typically formed in about 12 hours, the fabrication time depending primarily upon the drying time between each layer.

For the formation of self-focusing lenses, the refractive index must be high at the center of the lens and decrease parabolically. Initially, the lens coatings are formed from the high index  $\text{SiO}_2/\text{TiO}_2$ -MPEOU POLYCERAM solution, which dries within about 30 seconds. During this drying time, the POLYCERAM solution bath is diluted with the computer-controlled addition of the  $\text{SiO}_2$ -MPEOU solution. The drying of layers containing higher percentages of  $\text{SiO}_2$  requires longer times. Hence, the drying time is increased from 30 to 120-240 seconds as the composition is varied.

The temperature of drying has been found to have a significant impact on the optical and mechanical properties of the final GRIN rod. Temperatures in the range of 80-175°C have yielded suitable lenses when the material is dried for a long enough time to remove the solvent phase and densify the material, and not so long as to degrade or decompose the polymer when higher temperatures are used. In current practice, temperatures of 100-120°C are being utilized to remove the solvent relatively slowly and densify the material without cracking.

After fabrication and final drying of the overall body, the rod is sectioned to form lenses. The lenses are polished with diamond and alumina water-based slurries to a 0.06  $\mu\text{m}$  finish. Under polarized light, the small changes in



refractive index of the individual coating layers can be revealed (when they are present) and a change of color (due to the polarization) is observed as the refractive index varies with the coating radius. Examination of the surfaces of POLYCERAM lenses in the scanning electron microscope indicates (as expected) that the successive deposition process does not form observable physical interfaces between layers.

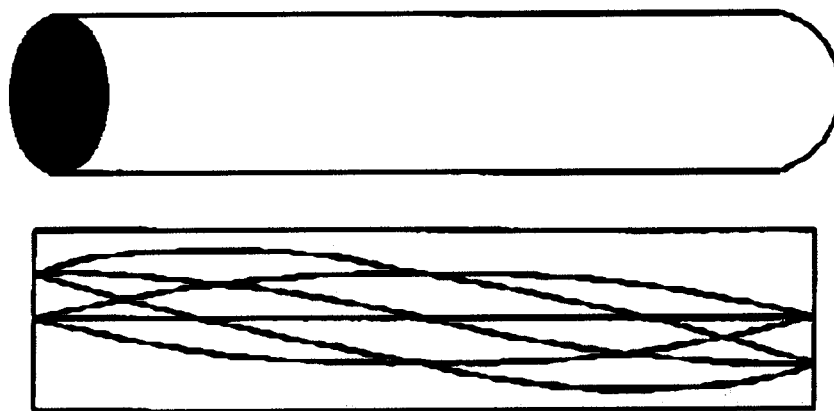
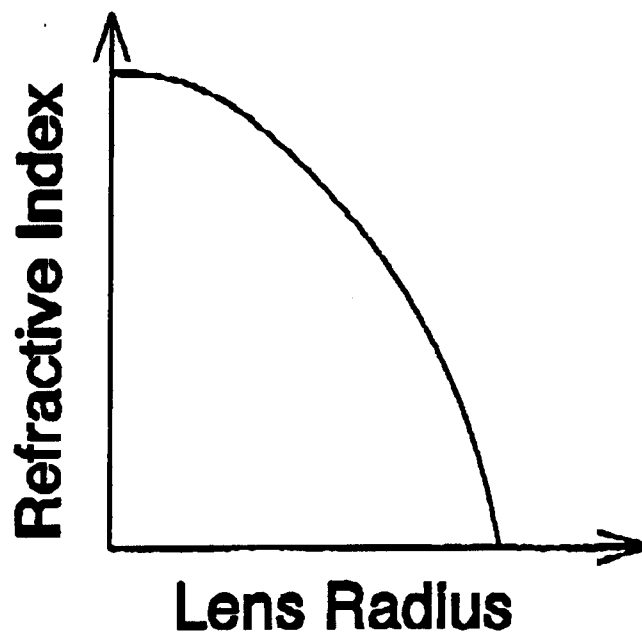
Research in this program area was initiated only in the past 10 months. Work during this period, besides demonstrating the feasibility of the concept, has indicated the importance of various processing parameters in obtaining high quality GRIN rods. For example, if the material is not thoroughly dried during the deposition process, then catastrophic cracking will occur within several days due to shrinkage stresses. Similarly, heating the lens to a very high temperature or for too long a time results in a highly brittle material, which typically cracks during sectioning or polishing. With appropriate choice of processing parameters, however, dense POLYCERAM rods have been formed which are not subject to cracking or attack by water.

In exploring details of the coating process, it was found that individual layers as thick as several  $\mu\text{m}$  or as small as 10's of nm can be deposited by varying parameters such as the solution concentration and withdrawal speed.

In the case of solutions containing high concentrations of Ti alkoxides, an unexpected relation between withdrawal speed and coating thickness had been observed. Since the solutions are typically rather dilute and exhibit Newtonian rheological behavior, a linear decrease in thickness with increasing withdrawal speed was anticipated. It was found, however, that at a limiting speed near 1 mm/sec, the thickness increases rapidly, apparently without bound, as indicated in Figure D-4. Research is currently underway to elucidate this phenomenon.

Finally, during the process of developing a computer-controlled deposition system, a model was developed to describe and predict the formation of POLYCERAM GRIN lenses by varying the concentrations of two or more separate solutions. The model has been incorporated into the software driving the computer-controlled deposition system (see above). Of present note, the model--and results of runs carried out to validate the model--indicate that an arbitrary index profile can be formed in POLYCERAM bodies using the present process, subject only to the available range of  $\Delta n$  between different end members. This flexibility will provide heretofore-unbelievable flexibility to the optical designer.

## Self-Focusing r-GRIN lens



**Cross Section - Side View**

**Figure D-1** Diagram of Self-focusing r-GRIN lens formed using a parabolic refractive index function over the lens radius.

## Convex Cylindrical GRIN Lens

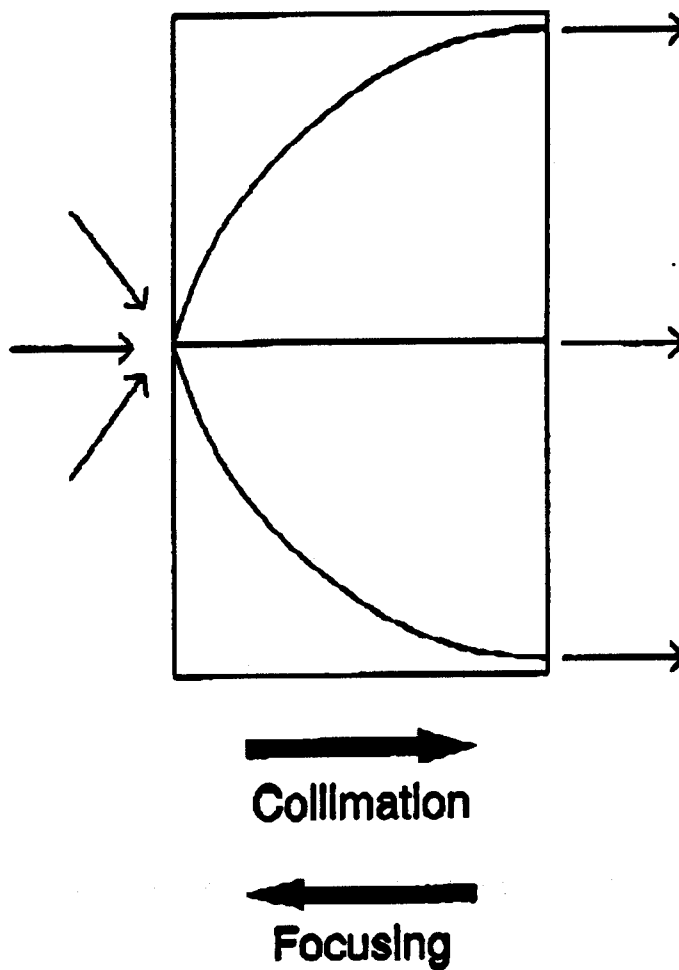


**Figure D-2**

**Schematic side-view of focusing/collimating r-GRIN lens.**

## Convex Cylindrical GRIN Lens

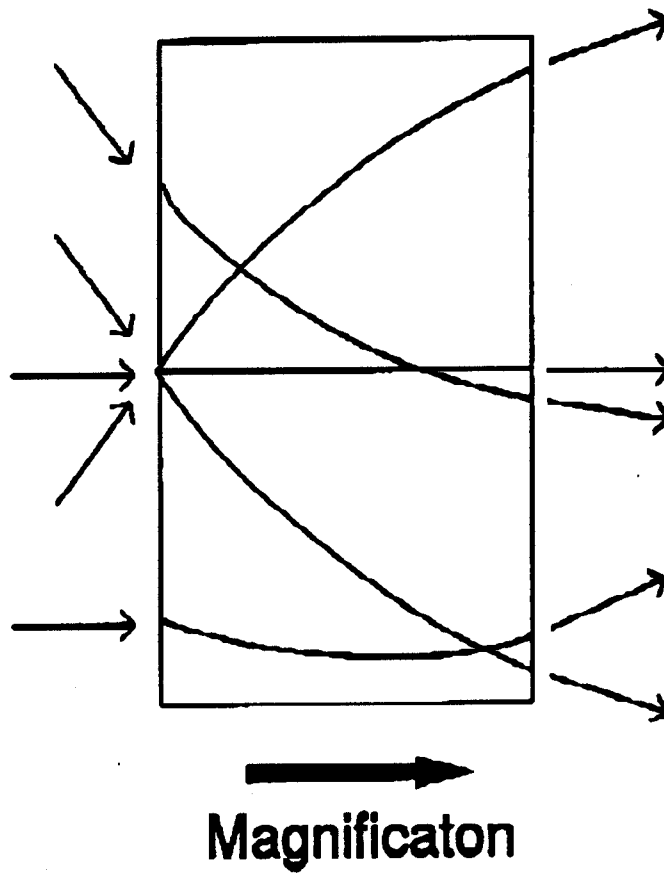


**Figure D-3**

**Schematic side view of magnifying r-GRIN lens.**

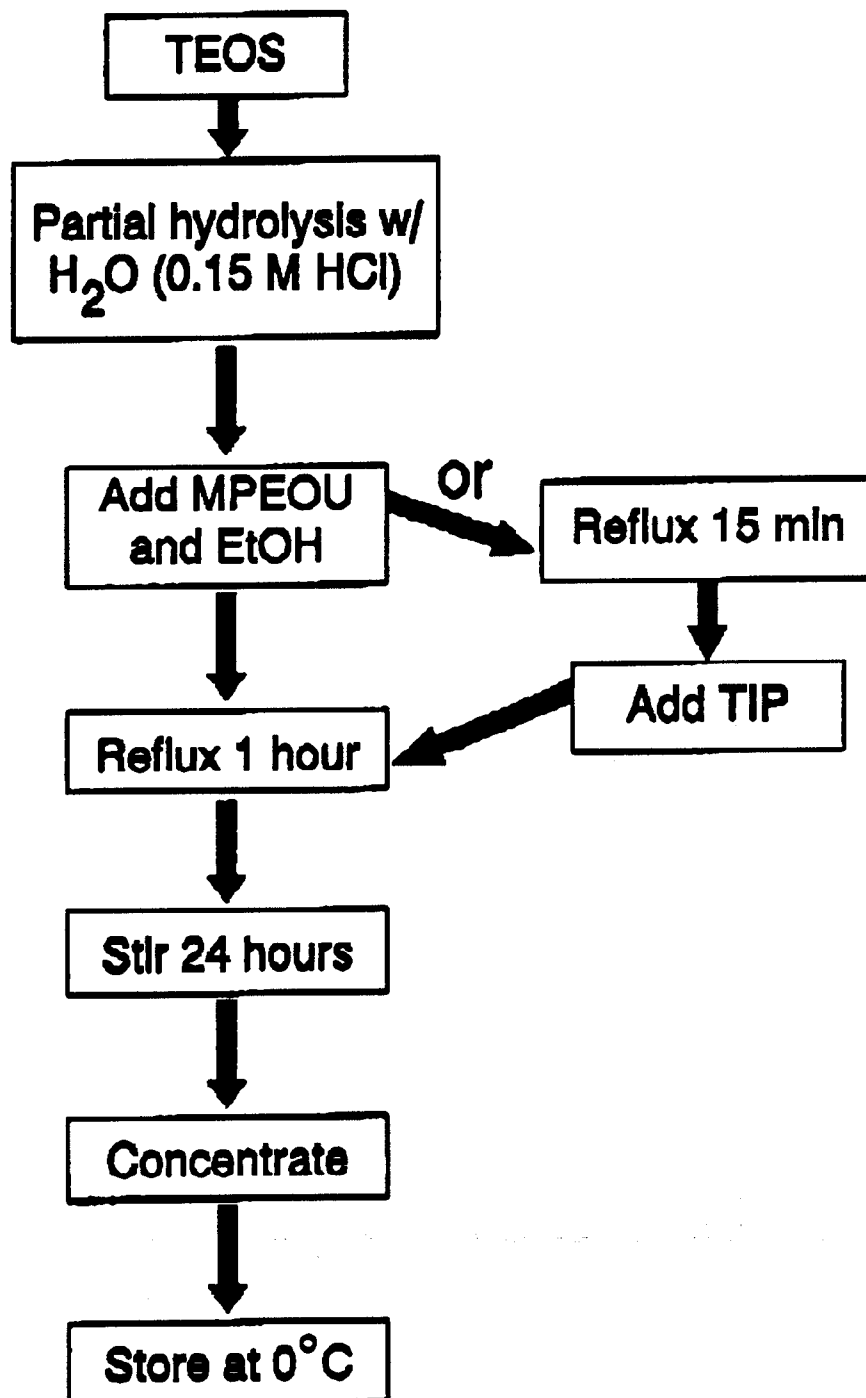


**Figure D-4** Synthesis Procedure for GRIN POLYCERAM Precursor Solutions.

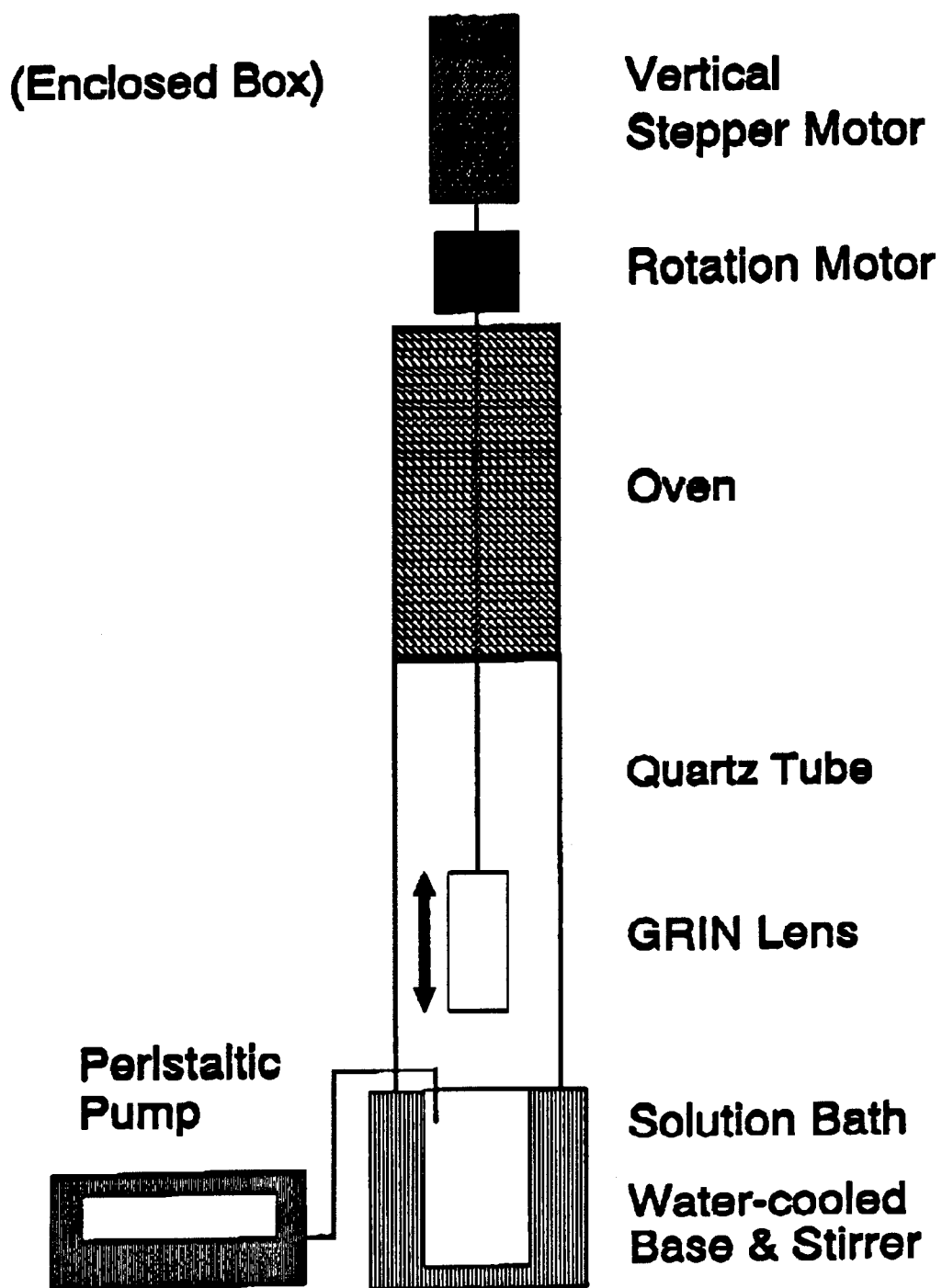


**Figure D-5 Schematic of GRIN dip coater machine.**

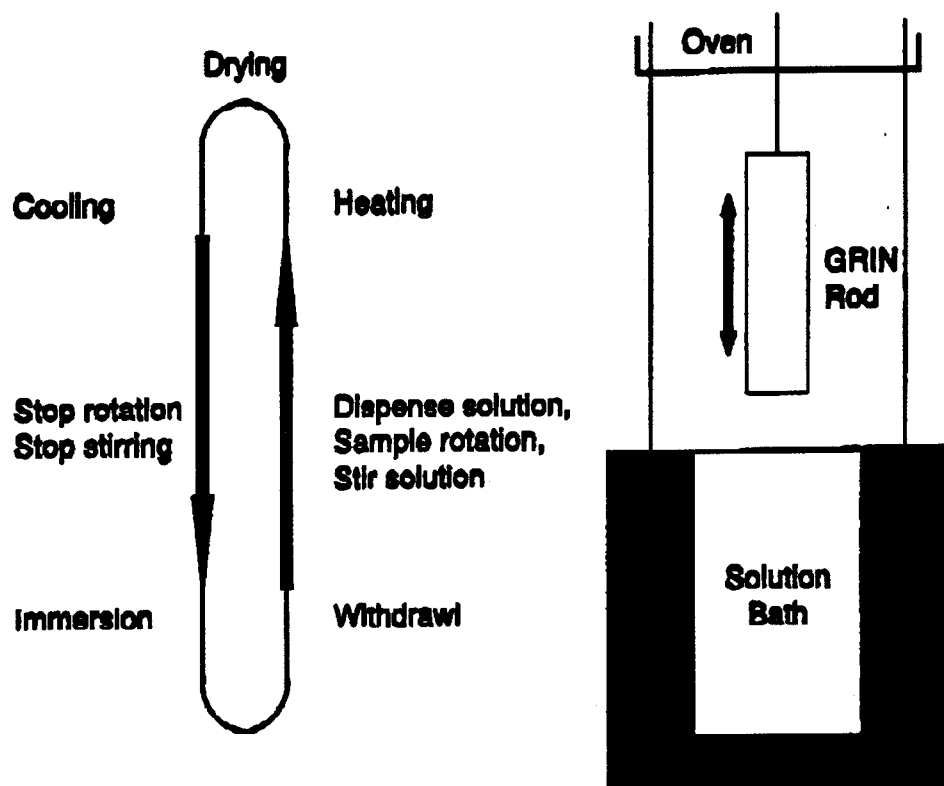


**Figure D-6** Diagram of dip coat cycle.



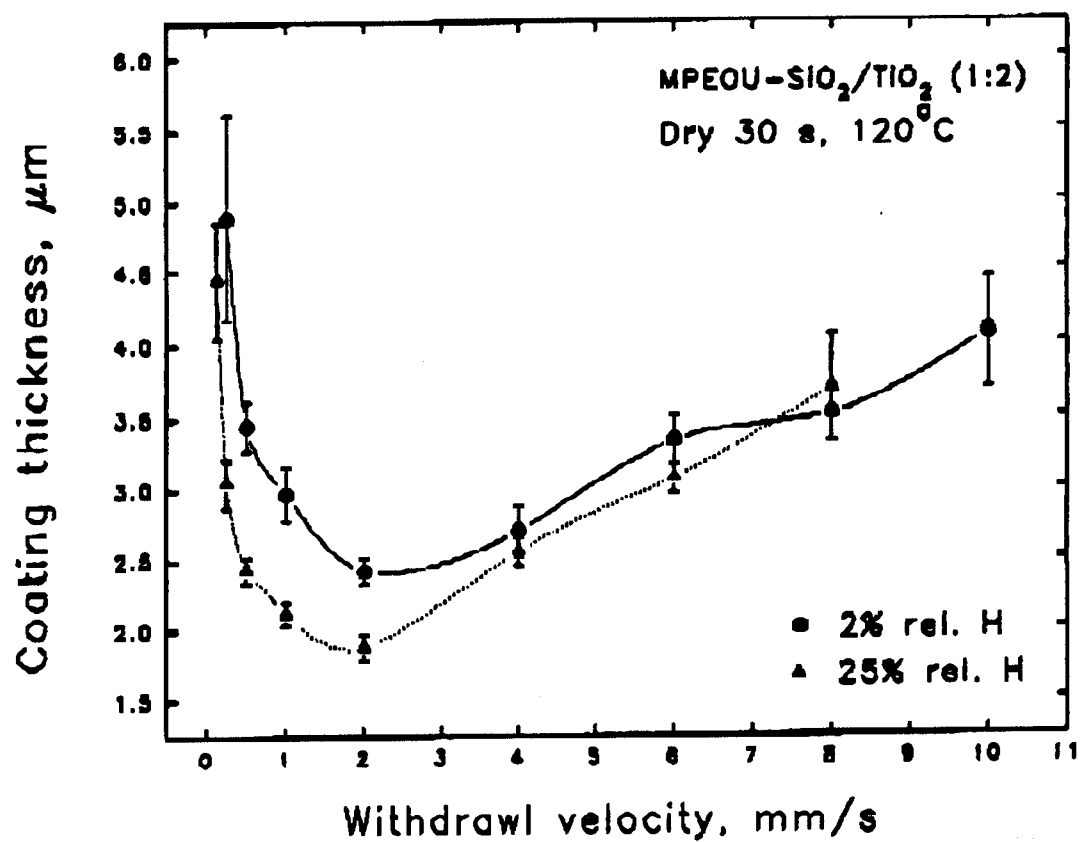


Figure D-7 Coating thickness versus withdrawal speed for a high index MPEOU- SiO<sub>2</sub>/TiO<sub>2</sub> POLYCERAM solution.

**Table D-1. Dip Coat Machine Parameters.**

<b>Vertical velocity</b>	<b>~0 to 10 mm/sec</b>
<b>Rotational velocity</b>	<b>3 rpm</b>
<b>Maximum GRIN rod size</b>	<b>up to 60 mm diameter, 6 cm height</b>
<b>Drying oven</b>	<b>RT to &gt;150°; cylinder, 20 cm height, 10 cm diameter, ~ 5 cm linear portion</b>
<b>Humidity</b>	<b>Typically <math>\leq 2\%</math></b>